



**COLLISIONAL DYNAMICS, LASING AND STIMULATED RAMAN
SCATTERING IN OPTICALLY PUMPED CESIUM AND
POTASSIUM VAPORS**

DISSERTATION

Kirk C. Brown, Major, USAF
AFIT/DS/ENP/12-M01

**DEPARTMENT OF THE AIR FORCE
AIR UNIVERSITY**

AIR FORCE INSTITUTE OF TECHNOLOGY

Wright-Patterson Air Force Base, Ohio

DISTRIBUTION STATEMENT A
APPROVED FOR PUBLIC RELEASE; DISTRIBUTION UNLIMITED

The views expressed in this dissertation are those of the author and do not reflect the official policy or position of the United States Air Force, the Department of Defense or the United States Government. This material is declared work of the U.S. Government and is not subject to copyright protection in the United States.

AFIT/DS/ENP/12-M01

COLLISIONAL DYNAMICS, LASING AND STIMULATED RAMAN
SCATTERING IN OPTICALLY PUMPED CESIUM AND POTASSIUM VAPORS

DISSERTATION

Presented to the Faculty
Department of Engineering Physics
Graduate School of Engineering and Management
Air Force Institute of Technology
Air University
Air Education and Training Command
in Partial Fulfillment of the Requirements for the
Degree of Doctor of Philosophy

Kirk C. Brown, BS, MS

Major, USAF

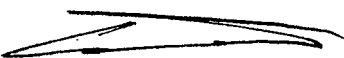
March 2012

DISTRIBUTION STATEMENT A
APPROVED FOR PUBLIC RELEASE; DISTRIBUTION UNLIMITED

COLLISIONAL DYNAMICS, LASING AND STIMULATED RAMAN
SCATTERING IN OPTICALLY PUMPED CESIUM AND POTASSIUM VAPORS

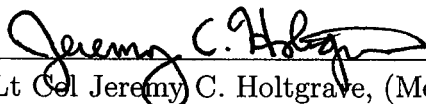
Kirk C. Brown, BS, MS
Major, USAF

Approved:




Glen P. Perram, PhD (Chairman)

5 MARCH 2012
Date



Lt Col Jeremy C. Holtgrave, (Member)


2 March 2012
Date



David A. Dolson, PhD (Member)

2-March-2012
Date

Accepted:



M. U. Thomas
Dean, Graduate School of Engineering
and Management

16 Mar 2012
Date

Abstract

This dissertation explores quantum effects and collisional dynamics in optically pumped alkali vapors. In cesium, we study the 7^2P state and remeasure the spin orbit mixing and quenching cross sections in mixtures with helium and methane using time-resolved fluorescence techniques. The cross section of an important laser species, ethane, is measured for the first time. The analysis includes the effects of radiation trapping using the Holstein model in the Doppler and pressure-broadened limit. To aid in the interpretation of data, we employ a rate equation model and compare simulations to experimental data. The fine-structure mixing cross sections for He, CH₄ and C₂H₆ are 14 ± 3 , 35 ± 6 and $73\pm10 \text{ \AA}^2$, respectively. The $^2P_{3/2}$ state is quenched more rapidly than the $^2P_{1/2}$ state.

Information about the spin orbit relaxation rates and quenching cross sections was used to assist in the demonstration and characterization of a three-level, optically pumped gas laser based on the spin orbit relaxation $7^2P_{3/2}$ – $7^2P_{1/2}$ transition using a mixture of 550 torr of helium and 100 torr of ethane. This laser is a conventionally pumped three-level system similar to the first infrared DPAL lasers. This method of optical pumping demonstrated that in addition to two-photon pumping schemes, a single photon method provided similar performance. The maximum output energy was $3.3 \mu\text{J}$ with a threshold of $10 \mu\text{J/pulse}$ and a slope efficiency of 0.45%.

Finally, we demonstrated tunable Raman and hyper-Raman lasing in potassium vapor. The hyper-Raman laser utilized a stable cavity without a buffer gas. The output was tunable from 766–770 nm. The threshold for the hyper-Raman process was 60 mW. The maximum slope efficiency (10.4%) and output power (12 mW) are comparable to previously demonstrated potassium DPAL systems that used several

atmospheres of buffer gas. Two separate Raman processes were identified, Stimulated Electronic Raman Scattered (SERS) and Three Photon Stimulated Raman Scattering (TPSRS) during the laser demonstration. The Raman processes were observed to compete with each other over the the full tuning range of the pump laser. We also demonstrated rapid switching between the two processes over a small pump wavelength range, with a corresponding and much larger hop in the output wavelength.

AFIT/DS/ENP/12-M01

To my children

Acknowledgements

I would like to thank my committee: Profs. Glen Perram, Lt. Col. Jeremy Holtgrave and David Dolson for their guidance, review and patience during the course of my AFIT studies. I would also like to thank Col. (ret.) John Franco for his outstanding mentorship, support and advice. Open source software packages were used exclusively in writing this document. Please support the developers of MiKTeX, TeXShop, JabRef, BibTeX and TeXMaker. I cannot thank my wife, children and extended family enough for their continuous support during this long and sometimes stressful process. Maraming salamat sa inyo! Were it not for my wife's encouragement and confidence during my undergraduate years, I would not be where I am today. To her constant enthusiasm, optimism and cheerfulness I owe a great deal.

Kirk C. Brown

Table of Contents

	Page
Abstract	iv
Acknowledgements	vii
List of Figures	x
List of Tables	xvi
I. Introduction	1
Optically Pumped Alkali Lasers	1
Spin Orbit Mixing and Quenching of the Cesium 7^2P state	5
Pulsed Cesium Laser Operating in the Blue	6
Potassium Hyper Raman Laser	6
II. Background	7
Alkali Atom Collisions With Foreign Gases	7
Spin Orbit Mixing and Collision Adiabaticity	12
Radiation Trapping	15
Optically Pumped Alkali Vapor Lasers	17
Raman and Hyper Raman Scattering	19
III. Spin Orbit Mixing and Quenching Rates of Cesium 7^2P in Mixtures of Helium, Methane and Ethane	23
Abstract	23
Introduction	23
Derivation of Eigenvalues	26
Radiation Trapping	29
Experiment	30
Results	32
Discussion	35
Conclusion	39
IV. Demonstration of a 459 nm, Pulsed, Optically Pumped Cesium Vapor Laser	43
Abstract	43
Introduction	43
Experiment	45
Results	47
Discussion	53

	Page
Rate Equations	53
Impact of Quenching on Laser Performance	56
Conclusion	60
V. Tuneable Hyper-Raman Laser in Potassium Vapor	62
Abstract	62
Introduction	62
Experiment	63
Results	66
Theory	70
Conclusion	75
VI. Conclusion and Recommendations	78
Cesium 7^2P Kinetics	79
Pulsed Blue Cesium Laser	80
Potassium Hyper Raman Laser	81
Blue Cesium Laser Recommendations	81
Potassium Hyper-Raman Laser Recommendations	83
Appendix A. Cesium Data	85
Appendix B. Potassium Data	91
Bibliography	93

List of Figures

Figure		Page
1.	Energy levels for some lower states of potassium. The wavelengths and transition rates may be found in Table 2	8
2.	Energy level diagram of cesium with wavelength and branching ratios from Heavens [37]. The wavelengths and transition rates may be found in Table 3.	9
3.	Value of the electronic potential as a function of internuclear distance for ^4He , methane and ethane. The C_6 values in parentheses were taken from Reference [12] and are in a.u. where 1 a.u. is equal to $e^2 r_0^5$	10
4.	Three level energy diagram of an OPAL. N_0 is a ground $S_{1/2}$ state, and N_1 and N_2 are the $^2P_{1/2}$ and $^2P_{3/2}$ states, respectively.	18
5.	Some lower energy levels of cesium. The wavelengths and transition probabilities are listed in Table 7	24
6.	Experiment layout. A heated glass cell contains about 1 gram of pure cesium. A 10 ns pulsed dye laser at 455.5 nm pumps the Cs $7^2P_{3/2} - 6S_{1/2}$ transition and side fluorescence is monitored via a RCA 31034 PMT attached to a 0.3 meter f/5 monochromator and recorded using a 1 GHz oscilloscope.	31
7.	Helium fluorescence decay curves of the cesium $7P_{1/2}-6S_{1/2}$ transition (459.3 nm) at 50°C using a 10 ns pulsed dye laser at 455.5 nm. The solid curves are the least squares fit of Eq. 19. The buffer gas pressures in torr are (a) 2.0 ± 0.02 , (b) 1.2 ± 0.012 , (c) 0.6 ± 0.006 , (d), 0.4 ± 0.004 and (e) 0.2 ± 0.002	33
8.	Stern-Volmer plot of experimentally derived rates (\square) and calculated rates based on Eq. 22(\blacklozenge) for Helium at 50°C . The solid line is a least squares linear fit to the experimentally derived rates.	34
9.	Stern-Volmer plot of experimentally derived rates (\square) and calculated rates based on Eq. 22(\blacklozenge) for methane at 110°C . The solid line is a least squares linear fit to the experimentally derived rates.	35

Figure	Page
10.	Stern-Volmer plot of experimentally derived rates (\square) and calculated rates based on Eq. 22(\blacklozenge) for ethane at 120°C. The solid line is a least squares linear fit to the experimentally derived rates. 36
11.	Plot of the amplitude, C , from fit of Eq. 19 (\square) and predicted by Eq. 23 (\blacklozenge) for helium. 37
12.	Plot of the amplitude, C , from fit of Eq. 19 (\square) and predicted by Eq. 23 (\blacklozenge) for methane. 38
13.	Plot of the amplitude, C from fit of Eq. 19 (\square) and predicted by Eq. 23 (\blacklozenge) for ethane. 39
14.	Simulated side fluorescence plots (solid) with data for ethane at T=120°C. The buffer gas pressures in torr are: (a) 0.10 ± 0.001 , (b) 0.150 ± 0.001 , (c) 0.20 ± 0.002 , (d) 0.30 ± 0.003 , (e) 0.40 ± 0.004 , (f) 0.50 ± 0.005 , (g) 0.60 ± 0.006 , (h) 0.80 ± 0.008 , (i) 1.00 ± 0.01 , (j) 1.10 ± 0.01 41
15.	Scaling of the fine structure mixing cross-sections, σ_{21} , with adiabaticity for He collisions with the lowest 2P states of Cs, Rb, K and Na, and the higher excited $n=7,8$ 2P and $n=5$ 2D states of Cs, (o) prior data [68, 48, 77] and (\bullet) present result for Cs 7^2P 42
16.	Scaling of fine structure mixing cross-sections with vibrational energy defect for (\bullet) Cs $6^2P_{3/2,1/2}$ [68] and (o) Cs 7^2P (present results). Buffer gases include CH_4 , C_2H_6 and C_2F_6 42
17.	Energy levels and wavelengths relevant to the Cs DPAL. Virtual states for two-photon transitions are denoted as dashed lines. Solid lines are pump transitions and dashed are radiative transitions. Fine-structure spacing is not to scale. 46
18.	Experiment Layout. A pyrex cell with Quartz windows filled with cesium vapor was enclosed in an aluminum heater block. The pump beam was focused into the cell using a 100 mm lens and the polarizations were separated using a polarizing beam splitting cube (PBSC). The output coupler (OC) was a 25 cm ROC with varying reflectivity. All optics were coated for 455 nm. 48

Figure	Page
19.	Instantaneous laser output power for four Cs concentrations. $T = 85^{\circ}\text{C}$ (+), 90°C (\circ), 100°C (\triangle), 110°C (\bullet) and pump laser (inset) 49
20.	Intensity profile of blue laser beam. The solid line is a least squares fit to a Gaussian. The divergence angle, θ is roughly 4 mrad, resulting in an M^2 value of 13.5. 50
21.	Measured pump intensity, I_p plotted against laser output intensity, I_l for four temperatures (A) 85°C , (B) 90° , (C) 100° , (D) 110° . The arrows indicates the direction of buildup for all cases. The photon buildup time was subtracted out for all cases, resulting in slopes that approximate the slope efficiency. 51
22.	Photon build-up time as a function of cesium concentration. 52
23.	Laser threshold (\circ) and slope efficiency (\blacktriangle) as a function of Cs density 53
24.	Fourier spectrogram of the output pulse. The oscillations in the tail of the pulse are centered around frequency of about 260 MHz for ($- - -$) 85°C , (\cdots) 90°C , ($\cdot - \cdot$) 100°C and ($—$) 110°C . The longitudinal mode spacing of the cavity, $\nu = c/2L$ is 321 MHz. 54
25.	Simulated longitudinally-averaged intracavity laser intensity and experimental laser output pulses for four cell temperatures: (a) 85°C , (b) 90°C , (c) 100°C , (d) 110°C 58
26.	Predicted population inversion, Δ_{10} , as a fraction of the initial ground state concentration for a blue DPAL assuming no stimulated emission. The values of the quenching cross section, σ , represents the range of typical values found in the literature. The fraction quenched to the ground, ξ is assumed to be unity. 59
27.	Predicted population inversion for several values of ξ , as a fraction of the initial ground state concentration for an infrared DPAL ($- - -$) and blue DPAL ($—$) assuming no stimulated emission. The quenching cross section for the infrared case is 1 \AA^2 and 10 \AA^2 for the blue case 60

28.	Simulated longitudinally-averaged intracavity laser intensity (solid lines) at $T = 120^\circ\text{C}$ for four values of ξ : 0.75, 0.50, 0.25, 0.10 from top to bottom, respectively. The experimental data is also shown (empty squares). A decrease in amplitude and increase in pulsewidth is seen with an decrease in ξ	61
29.	Schematic of experiment layout. (OC) Output coupler and (HR) high-reflector.	65
30.	Photograph of potassium hyper Raman laser experiment	66
31.	Semilog plot of output intensities for a specific pump wavelength showing the nonlinear features at 325°C . For all plots: (A) 2^{nd} anti-Stokes, (B) 1^{st} anti-Stokes, (C) residual pump, (D) 1^{st} Stokes, (E) 2^{nd} Stokes. Clockwise from top left: D_2 pump with multiple order anti-Stokes scattering, anti-Stokes scattering, Rayleigh scattering, D_1 pump with multiple order Stokes scattering.	67
32.	Average output intensity as a function of potassium density for a pump power of 232 mW. Pump (\blacklozenge), 1^{st} anti-Stokes (\triangle), 1^{st} Stokes (\square), 2^{nd} anti-Stokes (\circ), 2^{nd} Stokes (\diamond)	68
33.	Output wavelength and average power in mW (given by the graylevel) for a specific input wavelength at an input power of 232 mW and temperature of 325°C . Vertical bars indicate position of D_1 and D_2 lines. (A) 2^{nd} Stokes, (B) 1^{st} Stokes, (C) Pump, (D) hyper Raman process, (E) 1^{st} anti-Stokes (F) 2^{nd} anti-Stokes.	69
34.	Onset of hyper Raman lasing. Pump wavelength: 767.6 nm (solid), 767.8 nm (dashed), 768.1 nm (dot-dash). The point (A) is the 1^{st} anti-Stokes, (B) is the pump and (C) is the hyper Raman process. The point (O) is the initial point where the process can be seen separated from the pump beam in this spectrometer. The tuning from the pump beam is linear with a slope of 2.01 nm/nm.	70

Figure	Page
35.	Evidence of process switching. Pump (A) tuning from 769.2 nm (dot-dash) to 769.3 nm (solid), results in selection of either hyper Raman (B) or SERS Stokes scattering (C). The temperature was 325 °C and the input power was 232 mW.71
36.	Input vs Output power for hyper Raman laser. Pump tuned to 768.2 nm at 325° C. The dashed line is a least-squares fit to the data. The slope efficiency was 10.4% and the extrapolated threshold is 60 mW. The maximum optical-to-optical conversion is about 7%72
37.	Temporal pulse shapes for: (○) potassium DPAL laser (770.3 nm) using 1400 Torr of He, (□) the anti-Stokes laser (763.5 nm) with no buffer gas. The FWHM of the DPAL is about 9 ns; for the Raman it is about 3 ns. The DPAL is pumped on the D ₂ line and lases on the D ₁ line. To achieve only anti-Stokes output, the Raman laser was tuned from 767.2 to 767.6 nm with anti-Stokes output blue-shifted by a constant 3.4 nm. The asymmetry and narrowing of the pulse is due to the copropagation with the pump pulse.....73
38.	Energy levels involved in a λ -type Raman process. In SERS, the ground state $ 1\rangle$ is first populated by a pump photon, ω_p . A second pump photon scatters off a virtual state below $ 4\rangle$ generating an antiStokes photon (or Stokes if $E_2 > E_3$) and increasing the population of the final state, $ 2\rangle$. The separation between $ 4\rangle$ and the virtual level is given by Δ_{42} and the detuning between the pump and $ 3\rangle$ and $ 2\rangle$ is given by Δ_{31} and Δ_{21} , respectively.....74
39.	Simulated fractional population densities of the ρ_{11} (---) and ρ_{33} (—) states for a pump detuning of -20 cm^{-1} from the D ₂ line (ρ_{33}).....76
40.	Simulated fractional population densities of the the $4^2P_{1/2}$ state (ρ_{22}), showing population transfer via a Raman process from $4^2P_{3/2}$77
41.	Vapor Pressure of Cesium according to Eqns. 49 and 5186

Figure	Page
44.	Simulated side fluorescence plots (solid) with experimental data for helium at $T=85^{\circ}\text{C}$. The buffer gas pressure in torr from top to bottom: 2.0, 1.2, 0.6, 0.4, and 0.2 87
42.	Time dependent fluorescence decay with double-exponential fits (—) for methane. Methane pressures in torr, from top to bottom: 1.0, 0.7, 0.5, 0.4, 0.3, 0.2, 0.1 88
43.	Time dependent fluorescence decay with double-exponential fits (—) for ethane. Ethane pressures in torr, from top to bottom: 1.3, 1.1, 1.0, 0.8, 0.6, 0.5, 0.4, 0.3, 0.2, 0.1 89
45.	Simulated side fluorescence plots (solid) with experimental data for methane at $T=110^{\circ}\text{C}$. Methane gas pressure in torr: (a) 0.2, (b) 0.4, (c) 0.6, (d) 1.2, (e) 2.0 90
46.	Vapor Pressure of potassium according to Eqn. 52 92

List of Tables

Table	Page
1. Alkali transition wavelengths, energies and quantum efficiencies between the ground state and the first two 2P states. Unbolded data from [11]. Bolded data from [1].	4
2. Transition wavelengths and probabilities for several dipole allowed transitions of potassium in Fig. 1.	11
3. Transition wavelengths and probabilities for several dipole allowed transitions of cesium in Fig. 2.	12
4. Cesium 7^2P spin-orbit and quenching cross sections from previous works. Cell temperatures given in the parentheses.	13
5. Fine structure mixing cross-sections and adiabaticity for He collisions with the lowest 2P States of Cs, Rb, K and Na and the higher excited $n=7,8$ 2P and $n=5^2D$ states of Cs.	14
6. Scaling of fine structure mixing cross-sections with vibrational energy defect for Cs $6^2P_{3/2,1/2}$ and Cs 7^2P . Buffer gases include CH_4 , C_2H_6 and C_2F_6	14
7. Transition wavelengths and probabilities for several dipole allowed transitions of cesium in Fig. 17.	25
8. Cesium 7^2P spin-orbit and quenching cross sections assuming unequal quenching cross sections of the fine-structure states, calculated from Eqs. 22 and 23 (top) and values used in the simulations of Fig. 14 (bottom). Cell temperatures given in parentheses.	40
9. Cesium 7^2P spin-orbit and quenching cross sections from previous works. Cell temperatures given in the parentheses.	40
10. Parameters and values used to model laser performance	57
11. Cesium physical properties	87
12. Cesium $7^2P_{3/2}$: optical properties of allowed dipole transitions	87

Table		Page
13.	Potassium physical properties	91

COLLISIONAL DYNAMICS, LASING AND STIMULATED RAMAN SCATTERING IN OPTICALLY PUMPED CESIUM AND POTASSIUM VAPORS

I. Introduction

Optically Pumped Alkali Lasers

Over the last several decades, the Department of Defense (DoD), in a joint effort with universities and the defense industry, developed laser technology for a variety of military applications. Laser technology provided the United States and our allies with a significant and persistent technical advantage over our adversaries in conflicts from the Vietnam War to the Global War on Terrorism. Lasers and other directed-energy weapons have long been viewed as a force multiplier, augmenting traditional kinetic kill mechanisms such as bullets, missiles and bombs. Acquisition budgets have waxed and waned, but few have given up hope that one day, lasers may reach their full potential as military weapons. Indeed, the ability to strike instantaneously at very long ranges is an attractive capability.

During the last thirty years, large, high power chemical and solid state laser systems have been developed and tested with the intent of installing them on airborne platforms. These laser systems were designed to identify, track, target and destroy enemy aircraft, missiles and ground targets at stand-off ranges. During the last decade, two chemical laser systems achieved significant program milestones including the destruction of moving targets: The YAL-1A Airborne Laser, a Megawatt-class Chemical Oxygen Iodine Laser (COIL) system and the Advanced Tactical Laser (ATL), a 100 kW class COIL laser mounted on-board a C-130. Both COIL systems use infrared

laser radiation at $1.315\text{ }\mu\text{m}$ to rapidly induce structural failure leading to target destruction. Lasers have also proven their effectiveness in maritime environments. In 2011, the Office of Naval Research demonstrated a 15 kW solid state laser system that successfully ignited the fuel tank of a small outboard motor in rain, fog and eight-foot seas. [2, 3]

Despite their initial success at downing targets, general public interest and positive support by military leadership, many programs have seen cost overruns and ultimately fell victim to budget cuts. These financial problems, as well as questions about the safety and reliability of large chemical laser systems have cast doubt on the future employment of these technologies. In fact, the Airborne Laser program was cut completely in December 2011. [20] However, the DoD has not given up on its high-power laser efforts. Instead it has invested in alternate laser technologies such as solid state, fiber and hybrid diode-pumped/gas laser systems. These laser systems have the potential to offer military leaders and warfighters a ruggedized and reliable laser system with few of the hazards found in chemical lasers. System cost, a major factor in determining the viability of new military acquisitions, scales directly in proportion to weight. The lack of chemical storage tanks, high-speed pumps and piping in solid state systems, serves to reduce weight thus driving down the cost of the system, especially for daily operations and routine maintenance. However, current solid-state systems have not emphasized weight savings over performance and the advantages they promise have yet to be realized. Solid state systems are powered exclusively on electricity, a battlefield asset that is mature, widely available and most importantly, familiar to commanders. Several solid state laser programs have recently demonstrated target destruction using lasers mounted on ground mobile systems: Boeing's Laser Avenger [4] was designed as a counter IED system and MATRIX was designed to attack UAVs. [94]

However, as with all engineering efforts, tradeoffs exist when adapting technology to military applications. Solid-state lasers are no exception. Two serious issues continue to plague many of these systems: (1) heat dissipation and (2) power scaling. Due to the higher density of the gain medium, heat dissipation remains a difficult challenge. With uneven heating, index of refraction gradients in the crystalline gain material can reduce the beam quality to a point where complicated and inefficient beam cleanup methods are required in applications where a diffraction-limited beam is desired. Additionally, the low gain of solid state systems further complicates efforts to scale output power, requiring multiple amplification stages with large areas.

In 2003, Krupke’s group at Lawrence Livermore National Laboratory, published two papers on a new hybrid laser design that promised high efficiency, scalability and near diffraction-limited beam quality ideal for power beaming to photovoltaic cells based on the lunar surface. [50, 51] This new category of lasers, dubbed “DPAL”s for diode-pumped alkali lasers, has become an area of fruitful research for several research groups in academia and the defense industry, including our own group at the Air Force Institute of Technology. DPALs are a marriage of a gas gain medium and a diode laser array pump. They operate as a three level system, requiring high pump intensities for maximum performance. They offer the efficiency, convenience and ruggedness of a solid state system with the simplicity, heat dissipation and excellent beam quality of gas lasers. At the heart of the DPAL design is an alkali vapor at low densities contained in a compact glass cell or stainless steel heat pipe oven. The alkali vapor is mixed with various noble gases or small molecules that serve two purposes: (1) pressure broaden the absorption and emission spectrum of the alkali transition lines and (2) rapidly transfer population from the pumped level to the upper laser level. The table below provides basic spectroscopic data about the alkalis used in DPALs. The table was reproduced from Reference [11] with extensions into

the visible wavelengths by the author. In the last decade, many successful systems have been demonstrated with output powers up to 145 W cw using Rb [104] and slope efficiencies as high as 81% in Cs [99]. A thorough summary of previous DPAL research will be presented in Chapters III and IV. A comprehensive listing can also be found in Sulham. [88]

Table 1. Alkali transition wavelengths, energies and quantum efficiencies between the ground state and the first two 2P states. Unbolded data from [11]. Bolded data from [1].

Alkali Metal	Laser (nm)	Pump (nm)	ΔE (cm) $^{-1}$	Quantum Efficiency (%)	States
Li	670.98	670.96	0.34	99.9	2P–2S
Li	323.52	323.52	0.096	99.9	3P–2S
Na	589.76	589.16	17.2	99.9	3P–3S
Na	330.99	330.33	5.6	99.8	4P–3S
K	770.11	766.70	57.7	99.1	4P–4S
K	404.84	404.52	18.8	99.9	5P–4S
Rb	794.98	780.25	237	98.1	5P–5S
Rb	421.67	420.30	77.5	99.6	6P–5S
Cs	894.59	852.35	554	95.2	6P–6S
Cs	455.65	459.36	181.0	99.1	7P–6S

If the concept of the DPAL is to be extended into the visible and UV, several areas will need to be addressed. The success of the near infrared versions of the DPAL is largely due to three factors: (1) High gain, easily broadened atomic transitions, (2) Rapid spin orbit mixing rates and (3) Low self and buffer gas quenching. Gain on atomic absorption and emission lines is largely based on the cross section, the peak value of the line shape function and is inversely proportional to the square of the wavelength. Further, quenching cross sections generally increase with increasing values of an electron’s quantum number, n . Lasers operating at wavelengths shorter than the near infrared may operate at much less efficiency and output power. Therefore they are probably limited to several low power yet useful applications: Underwater or space point-to-point communications, laboratory spectroscopy, and pollution monitoring.

In stark contrast to the three level laser action in DPAL is the concept of a Raman or Hyper Raman laser. In these lasers, strong pump radiation is scattered from alkali atoms and the resulting output is shifted by an amount defined by the nonlinear process(es) active. Alkali atoms have properties that allow for highly efficient production of nonlinear output, and there is a long and diverse history of research in this field. Since strong pump intensity is a requirement for these lasers, they are not necessarily candidates for high-power weapons. In fact, nonlinear processes have long been suspected of being a limiting factor for intensity scaling in gas lasers. However, there are several facts that may make the tunable Raman output from alkali vapors useful for laser communications, beam diagnostics, remote sensing or laboratory applications. The first is that the Raman output is shifted from the pump source by multiples of the spin orbit splitting for Stimulated Electronic Raman Scattering (SERS). The second is that spin-orbit or buffer gases are not required. Finally, Raman processes in alkalis can exhibit high gain, resulting in efficient optical conversion of pump radiation.

Spin Orbit Mixing and Quenching of the Cesium 7^2P state

Understanding the chemical kinetics of the the Cesium $7^2P_{3/2}-7^2P_{1/2}$ transition is critical to the performance of the blue cesium laser or variations thereof. Chapter III of the dissertation explores the measurement of the spin orbit mixing and quenching cross sections for several buffer gases commonly used in DPAL lasers: Helium, Methane and Ethane. The measurement of the spin-orbit and quenching cross sections for ethane in a mixture with cesium 7^2P was performed for the first time. The preliminary results were published in the *Proceeding of the SPIE: High Energy/Average Power Lasers and Intense Beam Applications V* during the 2011 Photonics West conference. [16] A more comprehensive account has been accepted for publication in *Physical Review A*. [18] This work can be found in Chapter III and additional plots

and results in Appendix A

Pulsed Cesium Laser Operating in the Blue

Chapter IV explores an extension of the DPAL laser concept discussed in the Introduction into the visible using direct optical pumping of the $7^2P_{3/2}$ state of cesium. The preliminary results were published in the *Proceedings of the SPIE: High Energy/Average Power Lasers and Intense Beam Applications V* during the 2011 Photonics West conference. [16]

Potassium Hyper Raman Laser

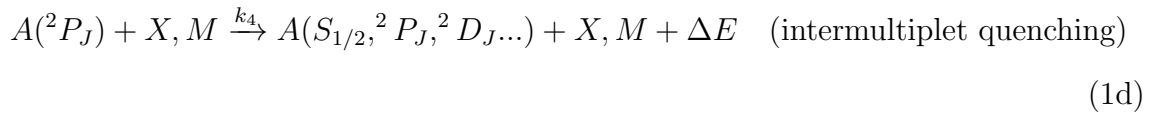
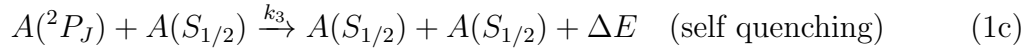
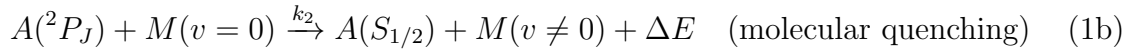
Chapter V discusses a laser concept that frequently occurs in alkali-metal vapor that are pumped with high-intensity sources: nonlinear Raman processes. The demonstration of a tuneable hyper-Raman laser is discussed. In traditional DPAL lasers, nonlinear effects are greatly reduced due to the presence of the buffer gas(es). However, if the buffer gas is reduced to low densities or removed completely, nonlinear effects like Stimulated Raman Scattering compete favorably with three level laser action. In fact, we demonstrate that in the absence buffer gases, strong two and three photon nonlinear effects are highly efficient and can match DPAL performance. This work was published in the *Proceedings of the 42nd AIAA Plasmadynamics and Lasers Conference* in June 2011 [19].

II. Background

This chapter discusses the fundamentals of collisions of excited alkali atoms, alkali vapor laser operation and nonlinear processes in atomic vapors.

Alkali Atom Collisions With Foreign Gases

The subject of excited alkali atoms in collisions with other atoms and molecules is an old one going back to the very beginnings of spectroscopic experimentation. All alkali metals have a single valence electron and are thus chemically reactive. Due to the simplicity of their atomic structure and ease of theoretical modeling, alkali metals are the most studied species with the longest history. The energy levels of the two alkali-metal species studied in this dissertation, Cs and K, are found in Figs. 1 and 2. The diminution of fluorescence intensity (*i.e.*, quenching) by foreign gases was reported in many flame-type experiments. In these experiments, the electronic energy of the excited alkali atom can be distributed to the collision partner in several ways according to the equations below:



The fraction of excited alkali states that participate in the processes listed in Equations 1a–1e depends greatly on the particular excited alkali species, electronic state and collision partner. For example, in collisions involving the first excited P state of an alkali atom, the primary processes are 1a,1b and 1e. This is mainly due to the fact that the first excited states are energetically distant to the other S, P and D states and quenching is direct to the ground state requiring a minimum (for Cs) of over $11,000 \text{ cm}^{-1}$ to be transferred to the collision partner and converted into kinetic energy or internal rovibrational energy. Thus, for the first excited states of the alkalis, many collision partners have large spin orbit mixing cross sections and low quenching cross sections, creating an ideal situation for the development of a DPAL laser.

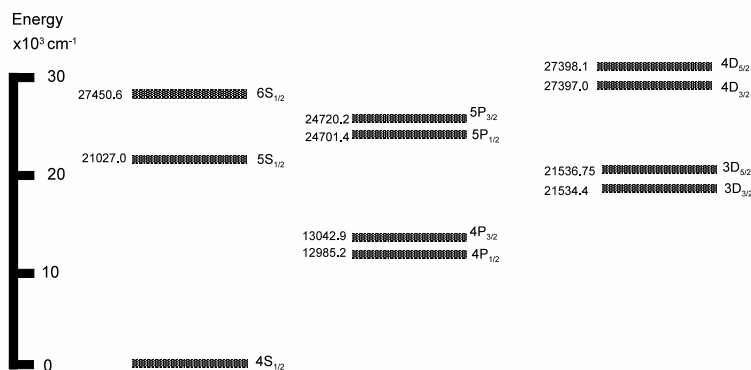


Figure 1. Energy levels for some lower states of potassium. The wavelengths and transition rates may be found in Table 2

This is not necessarily true if we now consider the second excited P state. In general, all the processes listed in Equations 1a–1e must now be considered, since the electronic potentials of the surrounding levels have a much larger influence on collisions. Additionally, as the atom radius increases with increasing quantum number, n , the cross sections for these reactions have been shown to increase in a monotonic fashion.

Collisions between an excited electronic state and another neutral atom or molecule

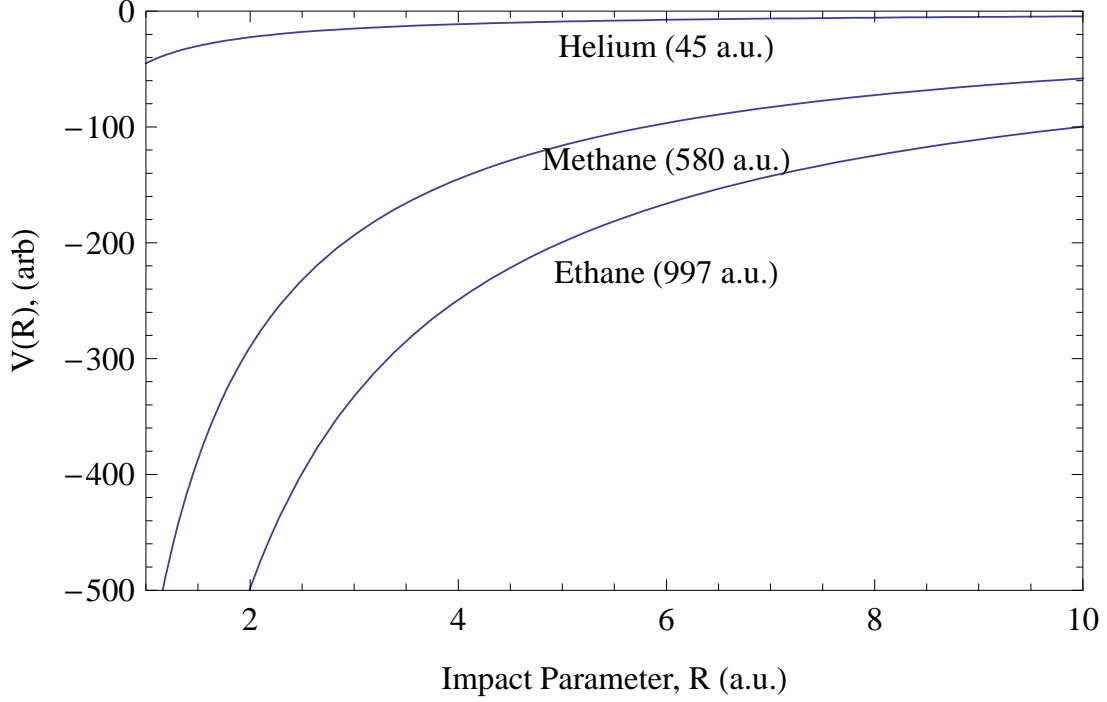


Figure 3. Value of the electronic potential as a function of internuclear distance for ^4He , methane and ethane. The C_6 values in parentheses were taken from Reference [12] and are in a.u. where 1 a.u. is equal to $e^2 r_0^5$

where $\alpha(i\omega)$ is the “dynamic polarizability”

$$\alpha(i\omega) = \frac{2}{3} \sum_{|i\rangle} \frac{\Delta E_i}{\Delta E_i^2 + \omega^2} \left| \langle g | \vec{\mathbf{D}} | i \rangle \right|^2 \quad (3b)$$

$|g\rangle$ is the atomic ground state, $|i\rangle$ is the i^{th} state, ΔE_i is the energy difference between the ground and i^{th} state, and $\vec{\mathbf{D}}$ is the electric-dipole operator. The contribution towards C_6 is not uniform among all states. For example, the value of C_6 for Cs is primarily from the 6P state with only 1% from other states. [26]

The upper bound to the quenching cross section may then be calculated by [29]

$$\sigma(\langle g \rangle) = \frac{3\pi}{2} \left(\frac{4 C_6}{\mu \langle g \rangle^2} \right)^{1/3} \quad (4)$$

where $\langle g \rangle$ is the average thermal relative collision speed given by the $\sqrt{8kT/\pi\mu}$.

Table 2. Transition wavelengths and probabilities for several dipole allowed transitions of potassium in Fig. 1.

Transition	Energy E, (cm ⁻¹)	Wavelength λ ,(nm)(Air)	Trans. Prob. A, (10 ⁶ s ⁻¹)	Line Reference	Trans. Prob. Reference
5S _{1/2} -4P _{3/2}	7983.65	1252.21	15.6	[6]	[76]
5S _{1/2} -4P _{1/2}	8041.37	1252.23	7.9	[6]	[76]
3D _{5/2} -4P _{3/2}	8491.78	1177.28	25.9	[6]	[76]
3D _{3/2} -4P _{3/2}	8494.10	1176.96	4.34	[6]	[76]
3D _{3/2} -4P _{1/2}	8551.81	1169.02	22.0	[6]	[76]
4P _{3/2} -4S _{1/2}	13042.896	766.48	38.0	[6]	[76]
4P _{1/2} -4S _{1/2}	12985.185	769.89	37.5	[6]	[76]
5P _{3/2} -4S _{1/2}	24720.139	404.41	1.16	[6]	[76]
5P _{1/2} -4S _{1/2}	24701.382	404.72	1.07	[6]	[76]

More recent work in this area [42, 21, 57, 65] has confirmed the trend of increasing cross section with a decrease in collision velocity in a variety of alkalis and noble gases, and also investigated cross sections between alkalis and small diatomic and polyatomic molecules.

The case of a collision between an atom and a molecule was treated by Fisher [32] who described the quenching collision between electronically excited alkalis and molecules in terms of a curve crossing model. In this model the excited alkali and molecule form an ionic intermediate complex ($A^+ - M^-(v)$) whose potential surfaces intersect with the potential surfaces of the final product. The intersection of the sets of potentials can be thought of as nodes with a defined probability for curve crossing. A particle entering on an initial potential surface proceeds to cross nodes and deposit a portion of the energy into product surfaces (*i.e.*, vibrational states), resulting in an electronic-to-vibrational transfer of energy that is roughly Gaussian in shape. Perhaps the most interesting result of Fisher’s paper was that the peak E-V transfer probability was not aligned with the vibrational state that corresponded to an energy equal to the electronic energy, but rather peaked at a vibrational level about one-half of the resonant state.

Table 3. Transition wavelengths and probabilities for several dipole allowed transitions of cesium in Fig. 2.

Transition	Energy E, (cm ⁻¹)	Wavelength λ ,(nm)(Air)	Trans. Prob. A, (10 ⁶ s ⁻¹)	Line Reference	Trans. Prob. Reference
5D _{3/2} -6P _{3/2}	2766.95	3614.088	0.107	[6]	[74]
5D _{5/2} -6P _{3/2}	2864.53	3490.967	0.781	[6]	[28]
7P _{1/2} -7S _{1/2}	3229.81	3096.148	3.52	[6]	[37]
5D _{3/2} -6P _{1/2}	3320.98	3011.151	0.913	[6]	[74]
7P _{3/2} -7S _{1/2}	3410.86	2931.805	4.05	[6]	[37]
7S _{1/2} -6P _{3/2}	6803.22	1469.490	11.4	[6]	[37]
7P _{1/2} -5D _{3/2}	7266.09	1375.88	1.59	[6]	[37]
7P _{3/2} -5D _{5/2}	7349.55	1360.55	1.10	[6]	[37]
7S _{1/2} -6P _{1/2}	7357.26	1358.83	6.23	[6]	[37]
7P _{3/2} -5D _{3/2}	7447.14	1342.43	0.13	[6]	[37]
6P _{1/2} -6S _{1/2}	11178.268	894.347	28.63	[6]	[69]
6P _{3/2} -6S _{1/2}	11732.307	852.113	32.79	[6]	[69]
7P _{1/2} -6S _{1/2}	21765.348	459.317	0.793	[6]	[91]
7P _{3/2} -6S _{1/2}	21946.397	455.528	1.84	[6]	[91]

Spin Orbit Mixing and Collision Adiabaticity

Consider the collision of two bodies, the first consisting of two equal masses, m_1 connected by a “spring” with a fundamental frequency of oscillation, ω_0 and the second a body with a different mass, m_2 . Let the difference between vibrational modes be quantized such that there are two states, $|i\rangle$ and $|j\rangle$, separated by an energy difference of ΔE , which may range from 1 to 10^3 wavenumbers (cm⁻¹). The two bodies approach each other with a collision velocity based on the reduced mass, μ , and the temperature T . At temperatures less than 2-3 times room temperature, they are considered “thermal” speeds that range from 10^2 to 10^3 m/s. The three bodies interact through long-range forces defined by the dispersion constant, C_6 and at a distance defined by the impact parameter, b . The interaction of the collision is said to be *adiabatic* if the collision time, τ is much greater than $\hbar/\Delta E$, where collision time may be described as $b/\langle g \rangle$ [33]. Therefore, if we consider the two states $|i\rangle$ and $|j\rangle$ as analogs to the fine-structure states of alkalis, we can expect the spin orbit mixing

Table 4. Cesium 7^2P spin-orbit and quenching cross sections from previous works. Cell temperatures given in the parentheses.

Collision Partner	Spin-Orbit, σ_{21} Cross Section (\AA^2)	Quenching, $\sigma_{10} = \sigma_{20}$ Cross Section (\AA^2)	Reference
Helium	12.8 ± 2.6 (320 K)	Not reported	[60]
Helium	11 ± 2 (448 K)	Not reported	[23]
Helium	14.9 ± 4.5 (320 K)	Not reported	[84]
Helium	15.2 ± 4.6 (320 K)	Not reported	[84]
Methane	40	60	[82]

cross section to be a monotonic function proportional to $g/\Delta E$, since g depends on the mass of the collision partner. Several experiments with the alkalis performed by Siara and Krause in the 1970s [83, 84] as well as the initial Gallagher study [33] confirmed this trend.

In Table 5 we show the mixing probability for collisions between several alkali-metals and helium. It can be seen that in general, the mixing probability, defined as (σ_{He}/σ_g) where σ_{He} is the cross section for collisions with helium and σ_g is the gas-kinetic cross section, approaches unity as the inverse adiabaticity (τ_{col}/τ_{osc}) increases, where τ_{col} is the duration of the collision and τ_{osc} is the period of oscillation corresponding to the ΔE of the fine-structure levels. The mixing cross-sections for alkali-metals and molecules may also be compared. In an inelastic collision, the rate of energy transfer from the electronic state to a set of ro-vibrational states is often distributed in a statistical manner. This comparison may be found in Table 6 where the difference between the vibrational energy of the fundamental mode and the “vibrational” energy of the fine-structure states are compared with the resulting cross section. In general, it can be seen that the cross section increases monotonically with a decrease in the difference of the two energies.

Table 5. Fine structure mixing cross-sections and adiabaticity for He collisions with the lowest ^2P States of Cs, Rb, K and Na and the higher excited $n=7,8$ ^2P and $n=5^2\text{D}$ states of Cs.

Alkali Metal	Fine Structure Pair	ΔE (cm^{-1})	Inverse Adiabaticity ($1/\xi$)	Mixing Probability (σ_{He}/σ_g)
^{133}Cs	$6^2\text{P}_{3/2,1/2}$	554	0.471	1.51×10^{-6}
^{85}Rb	$5^2\text{P}_{3/2,1/2}$	273.6	1.11	0.001
^{133}Cs	$7^2\text{P}_{3/2,1/2}$	181	1.44	0.141
^{133}Cs	$8^2\text{P}_{3/2,1/2}$	82.7	3.04	0.343
^{133}Cs	$5^2\text{D}_{5/2,3/2}$	97.6	3.09	0.363
^{39}K	$4^2\text{P}_{3/2,1/2}$	57.7	4.21	0.600
^{23}Na	$3^2\text{P}_{3/2,1/2}$	17.2	15.4	0.867

Table 6. Scaling of fine structure mixing cross-sections with vibrational energy defect for Cs $6^2\text{P}_{3/2,1/2}$ and Cs 7^2P . Buffer gases include CH_4 , C_2H_6 and C_2F_6 .

Collision Partners	$e^{-(\Delta E_{21}-\Delta E_{vib})/kT}$ (dim.)	Mixing Cross Section (\AA^2)
Cs $6\text{P}-\text{CH}_4$	0.012	21.36
Cs $7\text{P}-\text{CH}_4$	0.020	35
Cs $6\text{P}-\text{C}_2\text{H}_6$	0.28	64.83
Cs $7\text{P}-\text{C}_2\text{H}_6$	0.466	73
Cs $6\text{P}-\text{C}_2\text{H}_6$	0.68	65.6
Cs $6\text{P}-\text{C}_2\text{F}_6$	0.85	137.5

Radiation Trapping

Consider an atomic gas vapor where one atom is surrounded by a cloud of similar atoms at some density. If that atom emits a quanta of radiation at $h\nu$ that corresponds to one of the resonance lines of the atom, then there is some probability the quanta will be absorbed, reradiated and reabsorbed many times before leaving the cloud of atoms. This process is known as radiation trapping. The first theoretical study of radiation trapping of photons in an atomic vapor was performed by Holstein. Based on an early work by Compton, he assigned a probability, $T(\rho)$ that an emitted photon with an absorption coefficient, $k(\nu)$ would traverse a distance ρ before being absorbed.[38]

$$T(\rho) = \int P(\nu) e^{-k(\nu)\rho} d\nu \quad (5)$$

where $P(\nu)$ is the frequency spectrum of the radiation in an infinitesimal volume of gas, $d\nu$.

Several versions of $k(\nu)$ were discussed in his paper. For this dissertation we are only considering atoms with a Maxwellian velocity distribution that are pressure-broadened by the presence of gases in the cell. Since the alkali vapor was contained in a cylindrical glass cell, we only consider trapping results for infinite cylinders. In this limit the two transition probabilities are

$$T(\rho) \approx \frac{1}{k_0 \rho \sqrt{\pi \ln(k_0 \rho)}} \quad \text{Doppler broadening} \quad (6a)$$

$$T(\rho) \approx \frac{1}{\sqrt{\pi k_p \rho}} \quad \text{Pressure broadening} \quad (6b)$$

where k_0 is defined as the line-center absorption coefficient,

$$k_0 = \frac{\lambda_0^3 N}{8 \pi} \frac{g_2}{g_1} \frac{1}{\sqrt{\pi} v_0 \tau} \quad (7)$$

and in Equation 7, N is the density of the gas, g_2 and g_1 are the degeneracy of upper and lower state, respectively and v_0 is the average collision speed and τ is the spontaneous lifetime of the 2–1 transition.

Since Holstein's results are only valid in specific trapping regimes it become important to isolate which mechanism is dominant in a particular experiment. For a particular frequency, ν the dominant process is the one in the portion of the absorption line where $k_\nu \rho$ is approximately unity[39].

The radiation trapping has an effect on the observed radiative decay such that it become a product of the natural decay rate, Γ_{nat} and the escape factor, g . The escape factor for a cylindrical geometry may be calculated by [39]

$$g = \frac{1.60}{k_0 \rho \sqrt{\pi \ln(k_0 \rho)}} \quad \text{Dopper regime} \quad (8a)$$

$$g = \frac{1.115}{\sqrt{\pi k_p \rho}} \quad \text{Pressure broadened regime} \quad (8b)$$

In a later paper, Huennekens applied the Holstein theory to radiation trapping in sodium-noble gas mixtures, and experimentally demonstrated the Na density-dependent transition from Doppler to pressure trapped regimes.[40] The Doppler regime is characterized by a constant fluorescence decay rate independent of buffer gas pressure. The pressure-dependent regime is characterized by a positive linear slope.

A key point to note for the sake of later analysis is that the fluorescence decay rate of a single level, when collisionally populated by a buffer gas from a related fine-structure level (i.e. spin orbit mixing) is that the measure decay rate, ω_- , will be a

weighted sum of the form[39, 40]

$$\omega_- = \rho g_1 \Gamma_{1eff} + (1 - \rho) g_2 \Gamma_{2eff} \quad (9)$$

Optically Pumped Akali Vapor Lasers

The research in this dissertation is based on a visible analog to the DPAL. Therefore a short introduction to the processes involved in establishing inversion and lasing in an akali-buffer gas gain medium is necessary. Since most proof-of-concept research is based on using a surrogate pump laser we will refer to these lasers by the more general term, OPAL for Optically-Pumped Alkali Laser.

An OPAL is a three level laser where the ground state, N_0 , is optically excited by a pump laser tuned to a specifically electronic state (See Figure 4). In a three level laser the ground state is also the lower laser level. A fraction of the N_0 population is transferred into this state, labeled N_2 , and referred to as the pumped level. For most alkalis the spontaneous lifetime of this state ranges from about $10^1 - 10^2$ ns. The effect of the spin-orbit mixing gas is to promote rapid transfer between the pumped level and the upper laser level, N_1 . The population density of the upper laser level must be greater than twice the lower laser level for the three level laser to achieve threshold. Thus, pumping intensity must be high and spin orbit mixing rates greater than both radiative and quenching losses to other electronic levels.

The density of the ground state is controlled by the temperature of a cold finger attached to the glass cell that contains the buffer gas and alkali metal vapor. The temperature of OPAL lasers is typically in the range of 90 to 130 °C which amounts to a density of about 10^{13} cm^{-3} . In this work we use the vapor-pressure curves of Taylor and Langmuir which are reproduced in Appendix A

Besides the spin-orbit mixing and quenching rates, several other mechanisms are

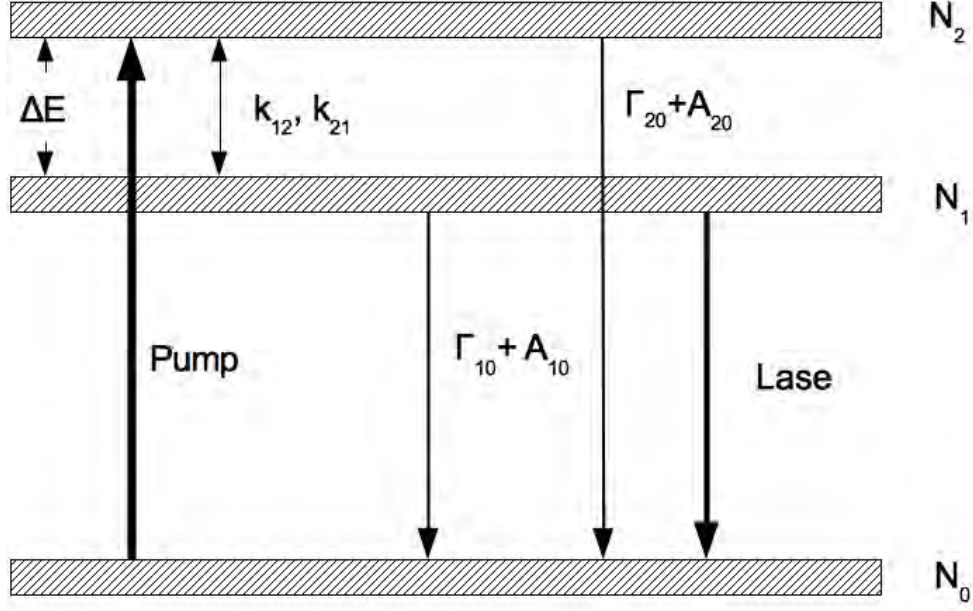


Figure 4. Three level energy diagram of an OPAL. N_0 is a ground $S_{1/2}$ state, and N_1 and N_2 are the $^2P_{1/2}$ and $^2P_{3/2}$ states, respectively.

important to the operation of any alkali laser. The first is optical cross sections of the pump and laser transition and the second are the losses due to the cavity. In this dissertation, we demonstrate a pulsed alkali vapor laser and apply the rate equation models developed for DPALs by Hager. [105, 36] The details of the model will be presented in Chapter IV.

The optical cross section of an atomic transition is mainly affected by the line shape, $g(\nu)$. The line shape of an atomic gas is the intensity of an emission line as a function of frequency for a small range above and below the peak which exists at some value, ν_0 . The line shape will be broadened in frequency by several different mechanisms, two of which are important to OPALs: Doppler and pressure broadening. Doppler broadening is a consequence that atoms in a gas with a Maxwellian speed distribution have their ν_0 shifted by some amount. The aggregate of many individual shifted absorption lines has the effect of creating a new line shape that has a functional form of [92]

$$I(\nu) = \left(\frac{4 \ln 2}{\pi}\right)^{1/2} \frac{1}{\Delta\nu_D} \exp \left[-4 \ln 2 \left(\frac{\nu - \nu_0}{\Delta\nu_D} \right)^2 \right] \quad (10)$$

where $\Delta\nu_D$ is the full width of the transition at the line center frequency given by [92]

$$\Delta\nu_D = \sqrt{\frac{8 k T \ln 2}{M c^2}} \quad (11)$$

In addition to Doppler broadening, the presence of a foreign gas specifically added to broaden the absorption lines due to pressure broadening. This line shape has a Lorentzian form (instead of the Gaussian form of the Doppler line shape) and consists of two parts: a broadening and a shift [25]

$$I(\nu) = \frac{C}{(\nu - \nu_0 - \Delta\omega)^2 + (\gamma/2)^2} \quad (12)$$

where the line shift is $\Delta\nu = N \bar{v} \sigma$ and the line broadening is $\gamma = \gamma_n + N \bar{v} \sigma$

For the the second resonance transition of cesium, the broadening due to helium was reported as 4.4 and $3.5 \times 10^{-20} \text{ cm}^{-1}/\text{cm}^{-3}$ [72] and for H_2 , $33 \times 10^{-20} \text{ cm}^{-1}/\text{cm}^{-3}$. [31]. Regarding self-broadening there are no published values available for the second resonance doublet and therefore we will use the value of the first, $5.7 \times 10^{-7} \text{ cm}^{-3} \text{ s}^{-1}$ and $6.7 \times 10^{-7} \text{ cm}^{-3} \text{ s}^{-1}$ for the D_1 and D_2 lines, respectively. Because the cesium pressures used in this dissertation were less than a mTorr, the use of these rates in the absence of actual data is justified.

Raman and Hyper Raman Scattering

The use of pulsed dye lasers in this work resulted in large optical intensities that can cause nonlinear responses in the gas vapor. In this situation, the polarization of the medium changes in such as way that the pump energy may be radiated from

virtual states, or deposited in a state that would be the result of a dipole-forbidden transition. These Raman transitions can have much larger transition probabilities than those of molecules mainly due to the fact that the probability increases as $(\nu_p - \nu_e)^{-1}$, where ν_p is the frequency of the pump and ν_e is the frequency of the electronic transition. Because the linewidths in atomic vapors are narrow compared to molecular mediums, the denominator of the transition probability can become very large. [97]

Sorokin first observed stimulated electronic Raman scattering (SERS) in potassium vapor when irradiating a gas cell with the output of a 750 MW pulsed ruby laser. [86] He noticed that the spectrally shifted output of the Raman line corresponded to the energy separation of the fine-structure states of the first 2P levels, similar to Raman scattering resulting from the ro-vibrational levels of molecules. The Raman output was strong enough to create 2^{nd} order lines shifted by $\nu_p + 2\Delta$ where Δ is the separation of the fine-structure states, 58 cm^{-1} , in potassium. In a similar potassium vapor experiment, Bradley observed up to four simultaneously generated SERS lines. [15]. Anikin was the first to observe an additional three-photon Raman process in potassium vapor which competes with the two photon SERS process. [10]. This newly identified Raman effect was found to have a frequency of $2\nu_p - \Delta$. The three photon process was also observed in sodium by Shevy who was the first to adequately explain why the three-photon effect was so efficient. [79, 80] He later demonstrated that the input polarization controls the intensity of the three-photon process. [78]. Indeed, in our potassium system, the polarization of the pump was orthogonal to the laser output, ideal for the production of three-photon stimulated Raman scattering.

When a photon interacts with an atom in the ground state, one of three things can happen. The photon, can be absorbed by the atom, promoting it to an excited

state. The photon can interact with the atom in such a way that it scatters with no loss of energy—an elastic collision—which is called Rayleigh scattering. A photon can also interact with an atom in an inelastic collision, and the photon will gain or lose a small amount of energy. This is known as Raman scattering and the difference in the energy of the photon after the collision is known as the Raman shift. If the frequency of the photon is downshifted, this is called a Stokes scattering; if the reverse is true, it is called anti-Stokes scattering. The observed shift in frequency is mainly due to the rovibrational or electronic levels of the atom or molecule the photon scatters from. The process of Raman scattering is nonlinear, and is a function of the polarizability of the medium the photon travels through. Unlike real electronic or rovibrational states that are eigenfunctions of the Schrodinger equation, Raman processes occur through virtual transitions. These virtual transitions correspond to the polarization state of the medium. If a Raman process occurs by absorbing two photon through another virtual transition, the process is called hyper-Raman scattering. The process transitions from spontaneous to stimulated when the amount of photons traveling in the +z or -z direction increase the amplitude of the Stokes wave in proportion to the Raman gain. The polarization of a medium can be written as a sum of the electric field \vec{E} and the susceptibility tensor $\chi^{(n)}$ of order n :

$$\vec{P} = P_0 + \chi^{(1)}E + \chi^{(2)}E^2 + \chi^{(3)}E^2 + \dots \quad (13)$$

The Raman process is governed by the third-order susceptibility, $\chi^{(3)}$. Since the virtual state can be considered a linear combination of the ground and excited states, the semiclassical framework is better suited for use when rate equations will be used to describe the time-evolution of the states. The semiclassical method begins with the Hamiltonian described in two pieces $H = H_0 + \mu_{ij}E_j$ where H_0 is the time-independent piece and $\mu_{ij}E_j$ represents the perturbation of the applied electric fields.

The states evolve according to the Bloch equations (also found in the literature as the Liouville equation) according to

$$\frac{d\dot{\rho}}{dt} = -i\hbar [H(t), \rho(t)] + \Gamma \quad (14)$$

where ρ indicates the density of particular state and Γ is the sum of the population relaxation and phase changing mechanisms.[35] An expansion of the above equation results in a system of rate equations with terms describing radiative rates, driving rates (form $i\Omega_j\rho_{ij}$) and transition rates (form $i\omega_{ij}\rho_{ij}$) where the Ω are the Rabi frequencies defined by $\mu E/\hbar$. The system can then be solved using standard numerical methods to predict the population levels.[75, 96, 95]

III. Spin Orbit Mixing and Quenching Rates of Cesium 7^2P in Mixtures of Helium, Methane and Ethane

Abstract

The fine-structure mixing and quenching cross sections of the cesium 7^2P state in mixtures of helium, methane and ethane were measured using laser-induced fluorescence techniques. This research was performed to study the kinetics associated with an optically-pumped blue cesium laser operating on the $7^2P_{1/2}$ – $6S_{1/2}$ transition. Fluorescence decay curves from pulsed-laser experiments were analyzed as a function of buffer gas density at cell temperatures near 393 K. The fine-structure mixing cross sections for He, CH₄ and C₂H₆ are 14 ± 3 , 35 ± 6 and 73 ± 10 Å², respectively. The $^2P_{3/2}$ state is quenched more rapidly than the $^2P_{1/2}$ state. A model that includes the effects of radiation trapping and independent quenching cross sections for each fine structure sublevel is compared to the experimental data. The rapid quenching negatively impacts the performance of a recent demonstrated optically pumped blue laser. We compare the cross sections for alkali-noble gases and extend the adiabaticity analysis to the higher lying excited states.

Introduction

Optically pumped alkali lasers have been intensely studied during the past decade. [50, 99, 66, 104, 89, 58] When pumped with a diode array, slope efficiency can exceed 80%. [99] These systems appear promising for scaling to high average power. For example, a rubidium laser pumped by a 1.28 kW diode stack with a 0.35 nm bandwidth has recently achieved 145 W average power. [104] The energy level diagram of some lower energy levels of the cesium system is illustrated in Fig. 17. The near infrared laser is diode pumped from the ground $6^2S_{1/2}$ state to the first excited, $6^2P_{3/2}$ state

at 852 nm, and lases after spin-orbit relaxation from $6^2P_{1/2}$ at 894 nm. The fine structure splitting of the 6^2P term is 554 cm^{-1} and relaxation by molecular collision partners such as ethane or methane at several hundred torr is required.

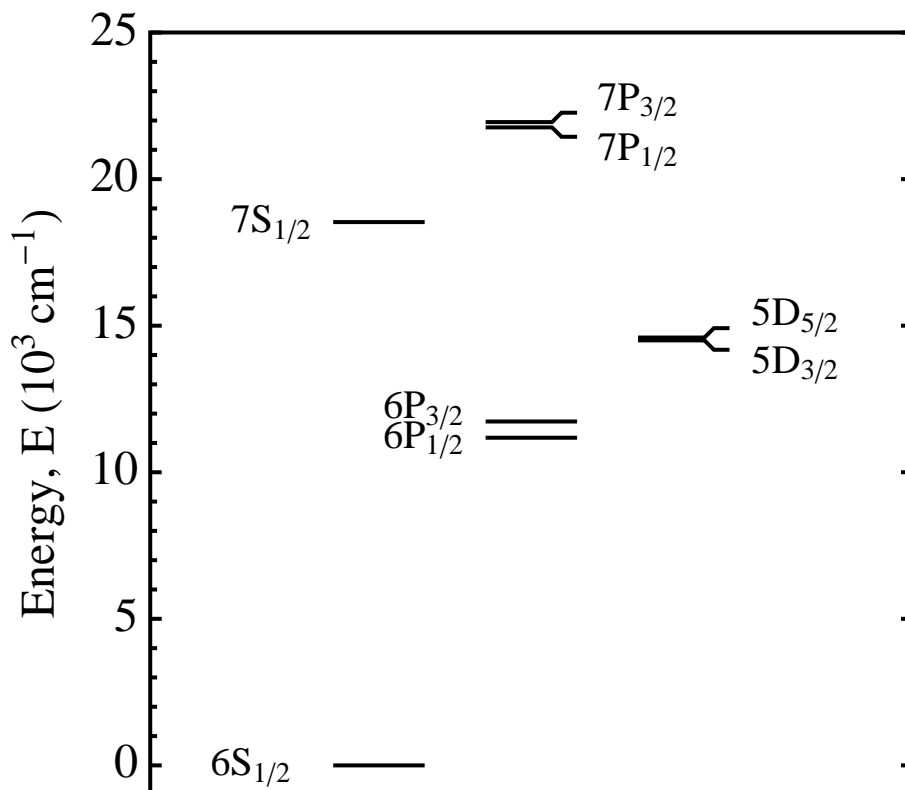


Figure 5. Some lower energy levels of cesium. The wavelengths and transition probabilities are listed in Table 7

Several optically pumped alkali lasers operating in the blue from the second excited, $7^2P_{3/2,1/2}$ states have also been demonstrated. Two color, sequential excitation [62], and two-photon direct excitation of the $6^2D_{3/2,1/2}$ states [89] followed by optical cascade to the 7^2P states, or direct one photon excitation of the 7^2P states [17] have been investigated. However, the fine structure relaxation and collisional quenching of these states are relatively unstudied. For Cs $7^2P_{3/2,1/2}$, there are several older reports of rapid fine structure mixing by rare gases [60, 23, 84] and molecular colli-

Table 7. Transition wavelengths and probabilities for several dipole allowed transitions of cesium in Fig. 17.

Transition	Energy E, (cm ⁻¹)	Wavelength λ ,(nm)(Air)	Trans. Prob. A, (10 ⁶ s ⁻¹)	Line Reference	Trans. Prob. Reference
5D _{3/2} -6P _{3/2}	2766.95	3614.088	0.107	[6]	[74]
5D _{5/2} -6P _{3/2}	2864.53	3490.967	0.781	[6]	[28]
7P _{1/2} -7S _{1/2}	3229.81	3096.148	3.52	[6]	[37]
5D _{3/2} -6P _{1/2}	3320.98	3011.151	0.913	[6]	[74]
7P _{3/2} -7S _{1/2}	3410.86	2931.805	4.05	[6]	[37]
7S _{1/2} -6P _{3/2}	6803.22	1469.490	11.4	[6]	[37]
7P _{1/2} -5D _{3/2}	7266.09	1375.88	1.59	[6]	[37]
7P _{3/2} -5D _{5/2}	7349.55	1360.55	1.10	[6]	[37]
7S _{1/2} -6P _{1/2}	7357.26	1358.83	6.23	[6]	[37]
7P _{3/2} -5D _{3/2}	7447.14	1342.43	0.13	[6]	[37]
6P _{1/2} -6S _{1/2}	11178.268	894.347	28.63	[6]	[69]
6P _{3/2} -6S _{1/2}	11732.307	852.113	32.79	[6]	[69]
7P _{1/2} -6S _{1/2}	21765.348	459.317	0.793	[6]	[91]
7P _{3/2} -6S _{1/2}	21946.397	455.528	1.84	[6]	[91]

sion partners [82], but not for the important laser specie, ethane. The corresponding quenching rates, their dependence on spin-orbit split state, and the product states are largely unavailable. Inter-multiplet energy transfer between 7²P_{3/2,1/2} and 6²D_{3/2} state with heavy rare gas partners are relatively fast, with the exception being He. [23] For the heavier rare gases, the presence of additional electronic levels, which are not a factor for the first ²P state, induces a barrier structure in the potential that reduces the cross section. For the case of He, that barrier structure is absent allowing the collision to proceed via long-range forces, increasing the cross section.

The rates for fine structure mixing of the lowest ²P states in the alkali metals for collisions with rare gases increase with decreased splitting, as predicted by adiabaticity arguments. [33, 68]. When the splitting is large and the collision energy is low, the duration of the collision is long relative to the oscillation period and the rates are slow. The more impulsive collision for the helium-potassium system leads to faster rates. Similar effects have been observed for the higher lying excited alkali states

where the fine structure splitting is less. For example, collision cross sections with noble gases and the 7^2P states are larger by a factor of 10^2 - 10^3 than those of the 6^2P state. [48, 60]. For the 8^2P state the values are larger by another factor of 10, corresponding to a reduction in the fine structure splitting. [23]

In the present work, pulsed laser induced fluorescence techniques are employed to measure the fine structure mixing and J-dependent quenching rates for the Cs $7^2P_{3/2,1/2}$ states.

Derivation of Eigenvalues

In this section we derive the key relationships for determining the spin orbit mixing and quenching cross sections. The populations in the ground $6^2S_{1/2}$ state, N_0 and the second excited $7^2P_{3/2}$, N_2 and the $7^2P_{1/2}$, N_1 , states are controlled by the following mechanism

$$[Cs(6S_{1/2})] + h\nu_{20} \xrightarrow{R} [Cs(7P_{3/2})] \quad \text{optical pumping} \quad (15a)$$

$$[Cs(7P_{3/2})] \xrightarrow{\xi_2 A_{20}} [Cs(6S_{1/2})] + h\nu_{20} \quad \text{spontaneous emission} \quad (15b)$$

$$[Cs(7P_{1/2})] \xrightarrow{\xi_1 A_{10}} [Cs(6S_{1/2})] + h\nu_{10} \quad \text{spontaneous emission} \quad (15c)$$

$$[Cs(7P_{3/2})] + M \xrightarrow{k_{20}} [Cs(S, P, D)] + M \quad \text{quenching} \quad (15d)$$

$$[Cs(7P_{1/2})] + M \xrightarrow{k_{10}} [Cs(S, P, D)] + M \quad \text{quenching} \quad (15e)$$

$$[Cs(7P_{3/2})] + M \xrightleftharpoons[k_{12}]{k_{21}} [Cs(7P_{1/2})] + M \quad \text{spin orbit mixing} \quad (15f)$$

where R is the optical pumping rate at $\lambda_{20}=455.5$ nm, A_{10} and A_{20} are the spontaneous emission rates and ξ_2 and ξ_1 are the radiation trapping factors discussed below. k_{20} and k_{10} are the quenching rates of the J=3/2 and J=1/2 levels, respectively, and k_{21} ,

k_{12} are the spin orbit mixing rates in the forward and backward direction. The spin orbit relaxation rates are related by detailed balance,

$$k_{12} = \frac{g_2}{g_1} e^{-\frac{\Delta E_{21}}{kT}} k_{21} = \rho k_{21} \quad (16)$$

where the degeneracies are $g_2=4$ and $g_1=g_0=2$ for N_2 , N_1 and N_0 , respectively. k is Boltzman's constant, $\Delta E_{21}=181 \text{ cm}^{-1}$ and at $T = 373 \text{ K}$, $\rho=0.9948$. The pump rate, R , is specified by pump laser intensity, $I_p(t)$:

$$R(t) = \frac{\sigma_{stim}}{h\nu_{20}} I_p(t) \left(\frac{g_2}{g_0} N_0 - N_2 \right) \quad (17)$$

where h is Planck's constant, ν_{20} is the frequency of the 2-0 pump transition and σ_{stim} is the stimulated emission cross section of the 2-0 transition. The arbitrary collision partner, M , is either helium, methane or ethane in the present work. First order decay rates are defined as $\gamma_{20} = k_{20} [M]$, $\gamma_{10} = k_{10} [M]$ and $\gamma_{21} = k_{21} [M]$, where $[M]$ is the number density of the collision partner.

The coupled rate equations can be cast in matrix form[77]:

$$\begin{pmatrix} \dot{N}_2 \\ \dot{N}_1 \end{pmatrix} = \begin{pmatrix} -(\xi_2 A_{20} + \gamma_{20} + \gamma_{21}) & R + \rho\gamma_{21} \\ \gamma_{21} & -(\xi_1 A_{10} + \gamma_{10} + \rho\gamma_{21}) \end{pmatrix} \begin{pmatrix} N_2 \\ N_1 \end{pmatrix} \quad (18)$$

When the duration of the pump pulse is short relative to the radiative and collisional time scales, the pump rate, R can be converted to an initial condition for the number pumped to the $7^2P_{3/2}$ state: $N_2^0 = N_2(t=0)$.

For instantaneous pumping, the rate equations in Eq. 18 have the time dependent solution for the fluorescence intensity, $I(t)$:

$$I(t) = C \left(e^{(-\lambda_- t)} - e^{(-\lambda_+ t)} \right) \quad (19)$$

with eigenvalues

$$\lambda_{\pm} = -\frac{1}{2}(\xi_1 A_{10} + \xi_2 A_{20} + \gamma_{10} + \gamma_{20} + (1 + \rho)\gamma_{21}) \pm \frac{1}{2} \sqrt{((\xi_1 A_{10} + \gamma_{10}) - (\xi_2 A_{20} + \gamma_{20}))^2 + 2\gamma_{21}((\xi_1 A_{10} + \gamma_{10})(\rho - 1) + (\xi_2 A_{20} + \gamma_{20})(1 - \rho)) + (1 + \rho)^2 \gamma_{21}^2} \quad (20)$$

The coefficient describing the initial conditions, C , is pressure dependent and may be written as:

$$C = \frac{\gamma_{21}}{\sqrt{((\xi_1 A_{10} + \gamma_{10}) - (\xi_2 A_{20} + \gamma_{20}))^2 + 2\gamma_{21}((\xi_1 A_{10} + \gamma_{10})(\rho - 1) + (\xi_2 A_{20} + \gamma_{20})(1 - \rho)) + (1 + \rho)^2 \gamma_{21}^2}} \quad (21)$$

For the present conditions, $\rho \approx 1$ and Eq. 20 can be reduced to:

$$\lambda_{\pm} = -\frac{1}{2}(\xi_1 A_{10} + \xi_2 A_{20} + \gamma_{10} + \gamma_{20} + 2\gamma_{21}) \pm \frac{1}{2} \sqrt{((\xi_1 A_{10} - \xi_2 A_{20}) + (\gamma_{10} - \gamma_{20}))^2 + 4\gamma_{21}^2} \quad (22)$$

Using the same argument, we can now simplify Eq. 21 to $C = \gamma_{21} / (\lambda_+ - \lambda_-)$ or

$$C = \frac{\gamma_{21}}{\sqrt{((\xi_1 A_{10} - \xi_2 A_{20}) + (\gamma_{10} - \gamma_{20}))^2 + 4\gamma_{21}^2}} \quad (23)$$

The values of k_{21} , k_{10} and k_{20} were calculated from Eq. 22 and Eq. 23 using the eigenvalues of the fluorescence curves fit to Eq. 19. Using a *Mathematica* nonlinear least-squares fit, the difference of the eigenvalues in Eq. 22 provides k_{21} and also

$k_{10} - k_{20}$. The sum of the eigenvalues in Eq. 22 returns $k_{10} + k_{20}$. These two equations were solved simultaneously to extract k_{10} and k_{20} . Equation 23 can be used as an independent check of the fit parameters in Eq. 22. The values of $\xi_1 A_{10}$ and $\xi_2 A_{20}$ were calculated in a similar way. The values for σ_{10} , σ_{20} and σ_{21} were calculated assuming $k = \bar{v}\sigma$, with $\bar{v} = (8kT/\pi\mu)^{1/2}$ where \bar{v} is the average speed of the collision pair, k is Boltzmann's constant, T is the cell temperature and μ is the reduced mass.

Finally, the effects of the finite duration pump pulse can be considered by direct numerical simulation of the rate equations in Eqs. 18. $I_p(t)$ is approximately a time-dependent Gaussian pulse with a FWHM of $\tau_p=10$ ns, a peak intensity, $I_{peak} \approx 10^8$ W/cm² and a phase delay of t_0 :

$$I_p(t) = I_{peak} e^{-4 \ln 2 \left(\frac{t-t_0}{\tau_p} \right)^2} \quad (24)$$

Radiation Trapping

For a given volume of atomic vapor, radiation emitted near a resonance line can be absorbed and emitted many times before escaping. The effects of radiation trapping at modest cell temperatures must be considered, especially at higher Cs densities where laser action may be expected. Detailed discussion of trapping in alkali vapor/buffer gas mixtures may be found in References [22, 59, 40, 71, 98]. The trapping coefficient, ξ , is defined as the number of times a photon is absorbed after traveling a distance r before being emitted [38]. For a cylindrical geometry ξ can be approximated for Doppler broadened transitions

$$\xi = \frac{1.60}{k_0 r \sqrt{\pi \ln(k_0 r)}} \quad (25a)$$

with k_0 defined as

$$k_0 = \frac{\lambda^3}{8\pi} N_0 \frac{g_2}{g_0} \frac{A}{\sqrt{\pi} v_{Cs}} \quad (25b)$$

and for pressure broadening

$$\xi = \frac{1.115}{\sqrt{\pi k_p r}} \quad (26a)$$

with k_p defined as

$$k_p = \frac{\lambda^2}{2\pi} N_0 \frac{g_2}{g_0} \frac{A}{\gamma_p} \quad (26b)$$

where A is the Einstein A coefficient of the transition, r is the radial path length through the Cs vapor, γ_p is the collisional broadening rate (s^{-1}), to include the effects of self and collision partner broadening [39], v_{Cs} is the average velocity of Cs, N_0 is the number density of Cs. For the Cs $7^2P_{3/2,1/2}$ states the collision rates are high and the present study is limited to low pressures of less than 2 torr. Thus Doppler broadening dominates the trapping factors: ξ_1 and ξ_2 are independent of pressure. Only when pressure broadening is significantly larger can a pressure dependent trapping factor complicate determination of the fine structure and quenching rates.

Experiment

The pulsed, laser induced fluorescence apparatus is shown schematically in Fig. 6. A pulsed dye laser (Continuum ND6000), with up to 25 mJ in a 10 ns pulse at 10 Hz was tuned to the cesium $7^2P_{3/2} - 6S_{1/2}$ (λ_{20} , 455 nm) transition. The pump bandwidth is about 2.1 GHz, large compared to the Doppler broadened absorption profile. The fluorescence of the cesium $7^2P_{1/2} - 6S_{1/2}$ transition (λ_{10} , 459 nm) was collected with a pair of lenses ($f_1=90$ mm, $f_2=250$ mm) and the image was focused on the entrance slit of a McPherson 218 (0.3 m) monochromator with a resolution of 0.5 nm. The fluorescence was detected with an uncooled RCA 31034 PMT and analyzed on a 1

GHz oscilloscope.

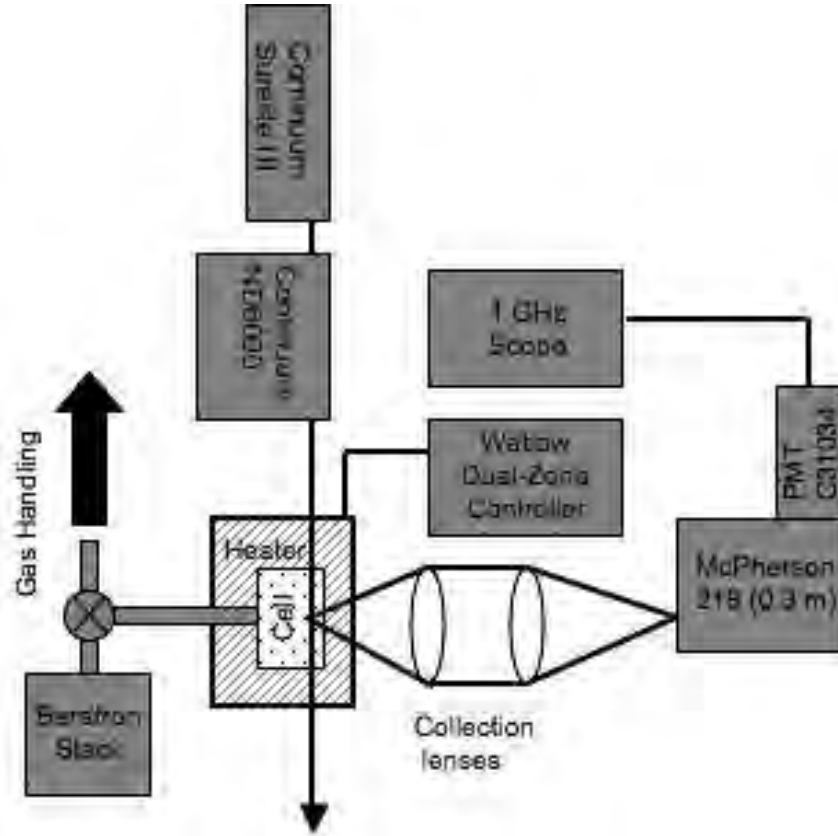


Figure 6. Experiment layout. A heated glass cell contains about 1 gram of pure cesium. A 10 ns pulsed dye laser at 455.5 nm pumps the Cs $7^2P_{3/2} - 6S_{1/2}$ transition and side fluorescence is monitored via a RCA 31034 PMT attached to a 0.3 meter f/5 monochromator and recorded using a 1 GHz oscilloscope.

The cesium was contained in a Pyrex cylinder (25.4 mm radius) enclosed in an aluminum heater block with an observation port perpendicular to the pump beam. The cell temperature was controlled ($\pm 1^\circ\text{C}$) using a dual-zone heater system (Watlow) with independent control of both the cell and cold finger. For these experiments the cell temperature was maintained about 5 degrees above the cold finger to prevent condensation on the cell windows. At 110°C the concentration of Cs is about 3.4×10^{16} atoms/cm³. For C₂H₆ we found that a temperature of 120°C was required to create an acceptable signal-to-noise ratio. At this temperature the concentration of Cs is about double that of 110°C . The cells were baked for several hours at 250°C under vacuum

(10^{-6} torr) before breaking the ampoule containing cesium metal. Research grade He, CH₄ and C₂H₆ gas pressure was measured with Baratron capacitance manometers (Model #690A) with 0.001-1000 torr ranges. For each pressure the scattered pump laser intensity was subtracted from the observed decay profiles by tuning off the resonance and recording the part of the signal not attributed to fluorescence.

Results

The fluorescence decay curves for emission from $7^2P_{1/2}$ for various He buffer gas pressures are provided in Fig. 7. As buffer gas increases, the rate for spin-orbit relaxation increases, the peak fluorescence intensity increases and decay rates increase. Significant population is transferred even at low pressure, indicating near gas kinetic rates. Scattered laser light obscures the decay curves for $t < 20$ ns. For each pressure, the decay curves were fit to the double exponential function of Eq. 19 generating the two eigenvalues, λ_+ and λ_- and the amplitude coefficient, C . The fits are compared with the data in Fig. 7. Fits for methane and ethane can be found in Appendix A

The pressure dependence of the fit eigenvalues are displayed as Stern-Volmer plots for He, CH₄ and C₂H₆ collision partners in Figs. 8–10. The intercepts on the Stern-Volmer plot for helium (Fig. 8) are nearly equal for the two eigenvalues, agree to within 2-5% of the known radiative rates of $A_{20}=7.5 \times 10^6 \text{ s}^{-1}$ and $A_{10}=6.3 \times 10^6 \text{ s}^{-1}$. [60] At the $T=50^\circ\text{C}$ cell conditions for the helium data, radiation trapping is minimal. However, the higher temperatures (and thus Cs concentrations) required of methane and ethane, the intercepts diverge and the corresponding effective rates suggest trapping factors of $\xi=0.81-0.92 \pm 0.16$ for $T=110^\circ\text{C}$ (CH₄) and $\xi=0.20-0.31 \pm 0.4$ for $T=120^\circ\text{C}$ (C₂H₆). The error bounds in the Stern-Volmer plots represent a confidence interval of 99%. The uncertainty in the pressure is small, $\approx 1\%$. The drift in absolute pressures is less than 15 mTorr.

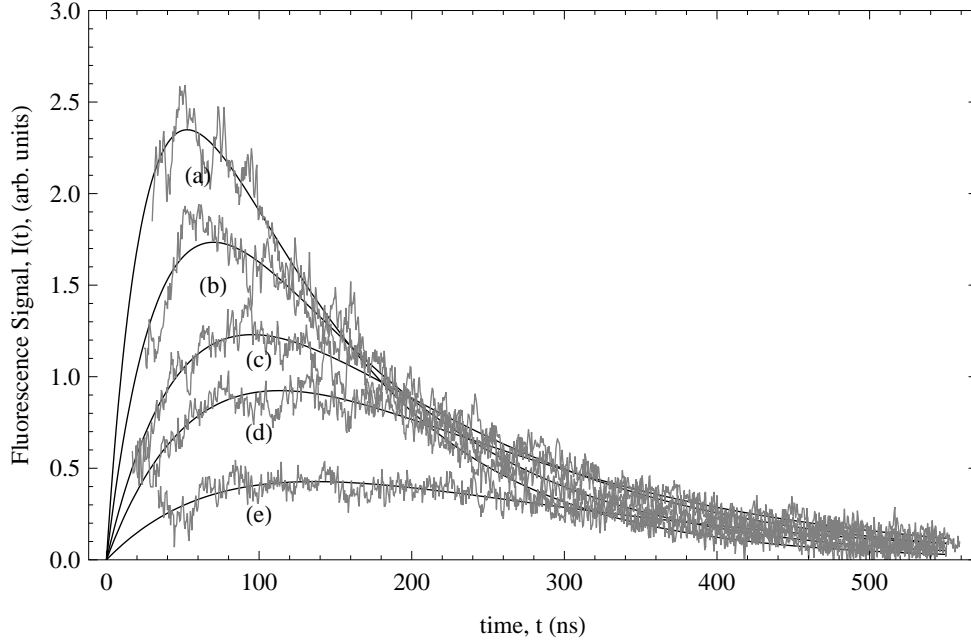


Figure 7. Helium fluorescence decay curves of the cesium $7P_{1/2}$ – $6S_{1/2}$ transition (459.3 nm) at 50°C using a 10 ns pulsed dye laser at 455.5 nm. The solid curves are the least squares fit of Eq. 19. The buffer gas pressures in torr are (a) 2.0 ± 0.02 , (b) 1.2 ± 0.012 , (c) 0.6 ± 0.006 , (d), 0.4 ± 0.004 and (e) 0.2 ± 0.002 .

The trapping factors, ξ are independent of He and CH_4 pressure, suggesting that Doppler broadening dominates the transition at the low buffer gas pressures. This seems probable since the Doppler broadening of Cs at those temperatures is about 800 MHz whereas the Cs-He broadening is only about 10 MHz at the highest pressure. The value of ξ for ethane is larger and weakly dependent on ethane pressure. This suggests that at the Lorentzian wing of the ethane broadened transition contributes to the radiation trapping. This “persistence” of the Lorentzian wing in radiation trapping was mentioned before by Huennekens in mixtures of sodium and noble gases. [40].

The amplitudes for the decay curves, C , obtained from the fit to Eq. 23 as a function of buffer gas concentration are shown in Figs. 11-13. The error bounds for these plots represent a confidence interval of 90%. The amplitude would be independent of pressure if the radiative and quenching rates were equal for the two spin-orbit split states. However, the significant curvature in Figs. 11-13 is consistent with the pre-

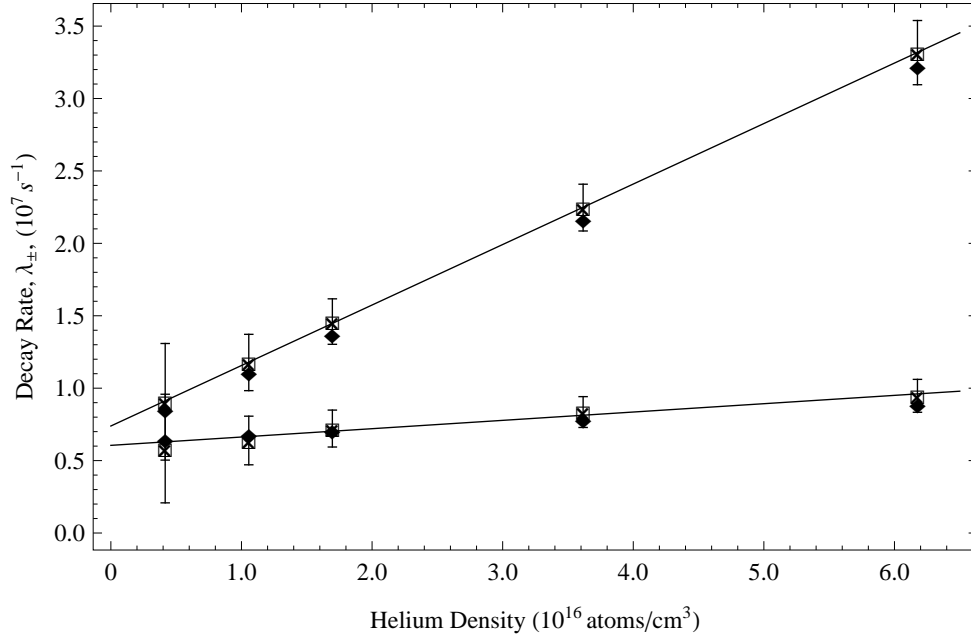


Figure 8. Stern-Volmer plot of experimentally derived rates (\square) and calculated rates based on Eq. 22 (\blacklozenge) for Helium at 50°C. The solid line is a least squares linear fit to the experimentally derived rates.

diction of Eq. 23, establishing the variance in quenching rates reported in Table 8. The eigenvalues predicted from Eq. 20 are wholly consistent with the observations, as illustrated in Figs. 8 and 10. Indeed, the three pressure dependent quantities, λ_{\pm} and C , uniquely define the three cross sections, σ_{20} , σ_{10} and σ_{21} .

Finally, the full numerical integration of the rate equations (Eqs. 18) with the time dependent pumping of Eq. 24 are compared to the observed decay profiles for the ethane case in Fig. 14. A single set of cross-sections, as summarized by Table 8 is sufficient to represent the full set of observed decay profiles. These results represent the best estimate for the spin-orbit relaxation and quenching cross-sections reported in this work. The simultaneous representation of all the decay profiles by a single set of rate coefficients illustrates the self consistency of the observations and analysis. The uncertainties in the spin-orbit relaxation rates are somewhat larger when all the data is simultaneously analyzed with the numerical simulations. The spin-orbit rates agree

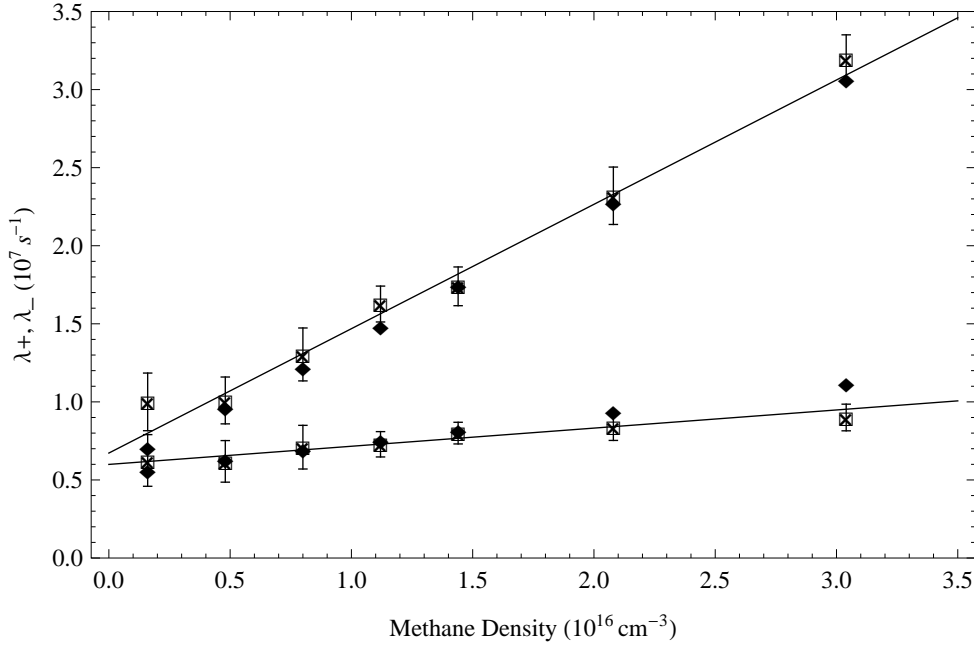


Figure 9. Stern-Volmer plot of experimentally derived rates (\square) and calculated rates based on Eq. 22 (\blacklozenge) for methane at 110°C. The solid line is a least squares linear fit to the experimentally derived rates.

within the error bounds. The consistency of the quenching rates is poorer, suggesting systematic error bounds for the quenching rates of 35%.

Discussion

While the fine structure mixing and quenching of the first excited $^2\text{P}_{3/2,1/2}$ states in the alkali metal atoms is well studied [60, 23, 84, 82, 33, 68, 48, 73], the kinetic database for the higher lying states is rather limited. [60, 23, 48] The rates for Cs $7^2\text{P}_{3/2,1/2}$ with helium and methane collision partners have previously been determined, and are summarized in Table 9. The current measurements of the spin-orbit relaxation rates for He and CH_4 agree favorably with the prior results. Indeed, there is no discrepancy considering the 20% error bands. The rate for ethane is newly reported in the present work.

The fine structure mixing rates for the first excited Cs $6^2\text{P}_{3/2,1/2}$ states with rare

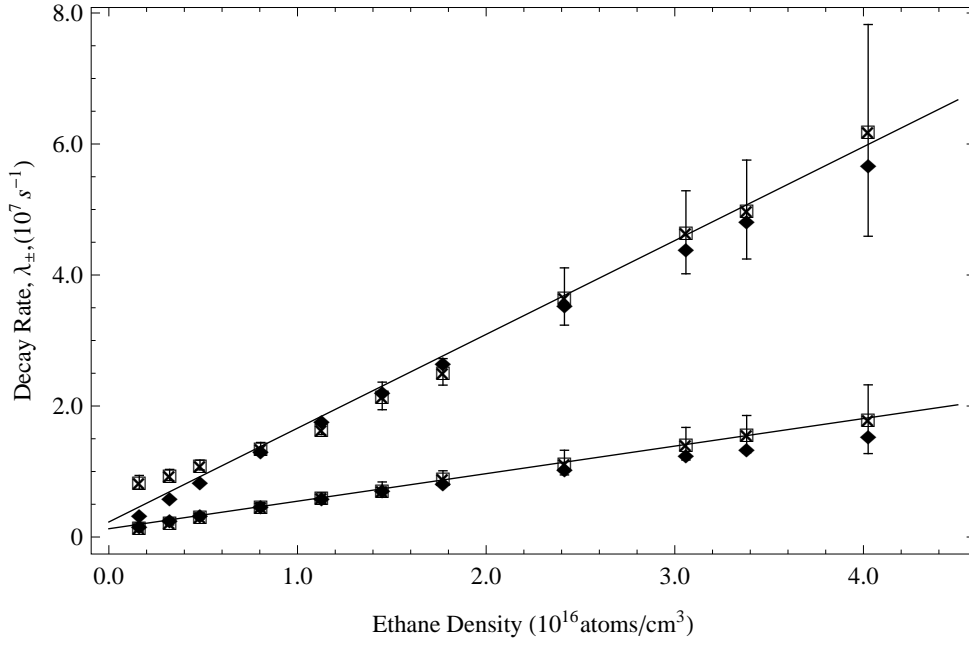


Figure 10. Stern-Volmer plot of experimentally derived rates (\square) and calculated rates based on Eq. 22(\blacklozenge) for ethane at 120°C. The solid line is a least squares linear fit to the experimentally derived rates.

gas partners are sufficiently rapid to sustain near infrared lasing only for the K and Rb diode pumped alkali laser systems. [105, 50] For the heavier alkali atoms the fine structure splitting increases and the mixing rates decrease. This trend has been qualitatively explained in terms of collision adiabaticity. [33] When the duration of the collision, τ_c , is long relative to the period of oscillation, $\tau_\nu = 1/\nu_{21} = h/\Delta E_{21}$, the interaction is adiabatic and the mixing probability is low. For light collision partners where the relative speed is high, the collision time decreases, the interaction is more impulsive, or sudden, and the mixing rate increases. We define adiabaticity, α , as the ratio of the oscillator period and collision duration:

$$\alpha = \frac{\tau_\nu}{\tau_c} = \frac{\bar{v}}{\nu_{21}L} \quad (27)$$

where the collision time is determined from a characteristic interaction length, L , and the relative speed, \bar{v} . The current results for helium are compared with prior

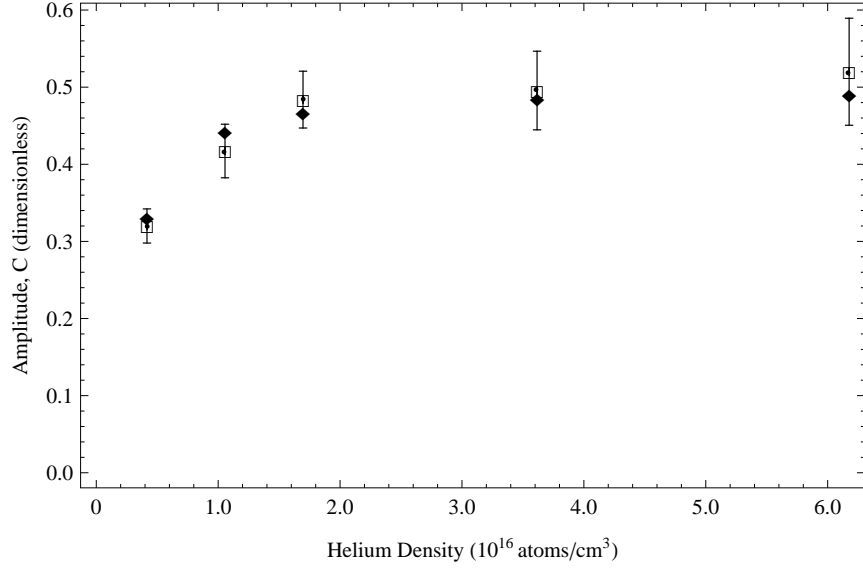


Figure 11. Plot of the amplitude, C , from fit of Eq. 19 (\square) and predicted by Eq. 23 (\blacklozenge) for helium.

studies of the Cs $n=6,7$, and $8\ ^2P_{3/2,1/2}$ and $5^2D_{5/2,3/2}$ levels in Fig. 15. Cross sections are reported as a probability per collision by normalizing relative to the gas kinetic value, $\sigma_g = \pi (r_{Cs} + r_{He})^2 = 9.9 \times 10^{-15} \text{ cm}^2$. For a fixed interaction length, $L = 0.2 \text{ nm}$, and given collision pair, $\bar{v} = 1.5\text{-}1.8 \times 10^5 \text{ cm/s}$ at $T=420\text{-}601\text{K}$, the adiabaticity depends primarily on the fine structure splitting. The results are nicely summarized by this single parameter. The cross-sections increase linearly with the inverse of the adiabaticity, until a near unit probability per collision is reached. The 8^2P term has the smallest splitting, $\Delta E_{21}/kT = 0.29$, yielding a near gas-kinetic rate.

Mixing induced by the molecular collision partners is generally faster than the rare gases. Recent studies of mixing in the Rb $5^2P_{3/2,1/2}$ and Cs $6^2P_{3/2,1/2}$ by molecular collision partners attribute the efficient collisional mixing to ro-vibrational excitation. [48, 68] The splitting in Cs $7^2P_{3/2,1/2}$ of 181 cm^{-1} is more nearly resonant with the 289 cm^{-1} vibrational mode of ethane than the lowest, 1367 cm^{-1} , mode of methane, leading to an enhancement in the mixing rate. The scaling with energy defect for the present study of Cs 7^2P is consistent with the recent results for Cs 6^2P , as shown in

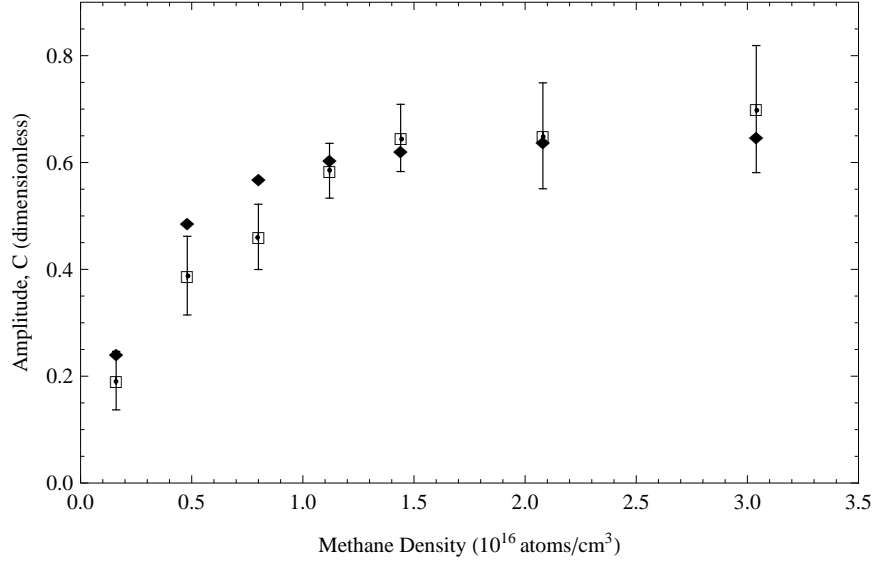


Figure 12. Plot of the amplitude, C , from fit of Eq. 19 (□) and predicted by Eq. 23 (◆) for methane.

Fig. 16.

Several prior studies of inelastic collisions between alkali metals and rare gases or small molecules report quenching rates that depend on fine structure splitting. Generally, the $J=3/2$ level exhibits a rate that is faster than the $J=1/2$ component by a factor of up to 4.5. [55] However, the $J=1/2$ state is more rapidly quenched in mixtures of $\text{Cs}(6^2\text{P}_{1/2})+(\text{H}_2, \text{HD} \text{ or } \text{CH}_4)$ [83], and equally quenched in mixtures of $\text{K}(4^2\text{P}_{1/2})+\text{C}_2\text{H}_4$. [29] The current results of Table 8 indicate ratios of σ_{20}/σ_{10} of 4.1, 1.8 and 1.9 for helium, methane and ethane, respectively. For molecular collision partners, spin-orbit mixing rates in Rb and Cs have been attributed to electronic to ro-vibrational energy transfer.[68] Resonances in the molecular energy transfer might explain the strong dependence on spin-orbit splitting.

The efficiency of the diode pumped alkali laser depends in part on rapid fine structure mixing without significant quenching. Quenching may compete with the pump rate and effectively increase the pump intensity required to reach threshold. Helium, methane and ethane collision partners meet these criteria for the first $^2\text{P}_{3/2,1/2}$ states

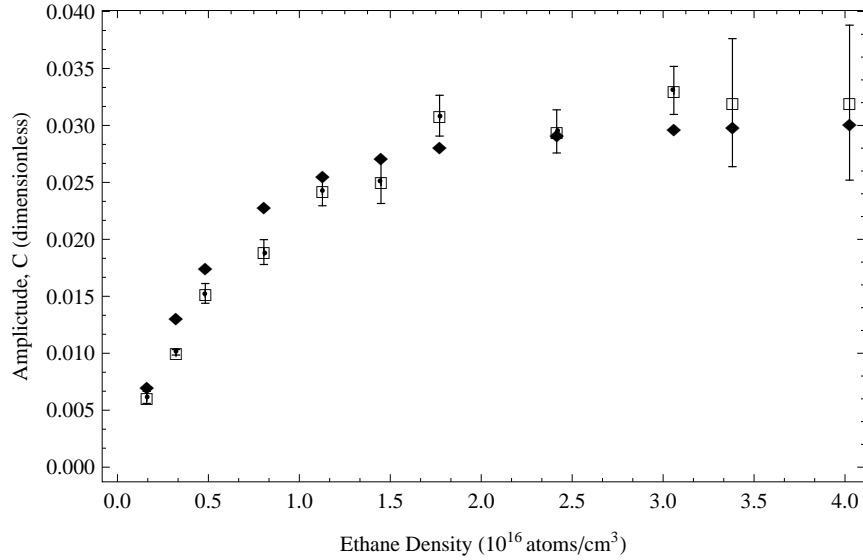


Figure 13. Plot of the amplitude, C from fit of Eq. 19 (\square) and predicted by Eq. 23 (\blacklozenge) for ethane.

associated with the near infrared lasers. For the blue analog laser, intermultiplet energy transfer is possible and quenching rates may be enhanced.

The present results indicate quenching for Cs $7^2P_{3/2,1/2}$ by helium is about 35% of the fine structure mixing. Our full numerical analysis agrees that the quenching of Cs $7^2P_{3/2}$ by methane is about 28% greater than the fine structure mixing. The ethane collision partner is somewhat more favorable for lasing, with a mixing rate more than twice for methane. The ethane quenching rate remains large, and significantly impacts laser performance. Indeed, our recent demonstration of a blue laser directly pumped on the Cs $6^2S_{1/2} \rightarrow 7^2P_{3/2}$ transition requires ethane as the collision partner. [17] Clearly, the performance of the blue analog laser is degraded by the rapid quenching rates and the search for alternative buffer gas partners is warranted.

Conclusion

Collision induced mixing in Cs $7^2P_{3/2,1/2}$ is rapid, due to the small energy splitting. The scaling of helium induced mixing rates among the various excited Cs states is

Table 8. Cesium 7^2P spin-orbit and quenching cross sections assuming unequal quenching cross sections of the fine-structure states, calculated from Eqs. 22 and 23 (top) and values used in the simulations of Fig. 14 (bottom). Cell temperatures given in parentheses.

Collision Partner	Spin-Orbit Cross Section (\AA^2)	Quenching Cross Section (J=3/2)	Quenching Cross Section (J=1/2)
Helium	14 ± 2 (323 K)	5 ± 1	≈ 1
Methane	42 ± 3 (383 K)	30 ± 2	20 ± 2
Ethane	80 ± 5 (393 K)	80 ± 6	10 ± 3
Helium	14 ± 3 (323 K)	4 ± 3	≈ 1
Methane	35 ± 6 (383 K)	45 ± 8	25 ± 2
Ethane	73 ± 10 (393 K)	59 ± 6	31 ± 3

Table 9. Cesium 7^2P spin-orbit and quenching cross sections from previous works. Cell temperatures given in the parentheses.

Collision Partner	Spin-Orbit, σ_{21} Cross Section (\AA^2)	Quenching, $\sigma_{10} = \sigma_{20}$ Cross Section (\AA^2)	Reference
Helium	12.8 ± 2.6 (320 K)	Not reported	[60]
Helium	11 ± 2 (448 K)	Not reported	[23]
Helium	14.9 ± 4.5 (320 K)	Not reported	[84]
Helium	15.2 ± 4.6 (320 K)	Not reported	[84]
Methane	40	60	[82]

well described by a single parameter, the adiabaticity. The mixing rates by molecular collision partners are somewhat larger and appear to be enhanced by vibrational energy transfer. In contrast to the lowest, Cs $6^2\text{P}_{3/2,1/2}$ levels, the higher excited states are rapidly quenched. Intermultiplet energy transfer likely enhances the quenching rates. Quenching of the blue laser upper level, $7^2\text{P}_{1/2}$, by ethane is about 42% of the fine structure mixing rate. While a blue laser with direct optical pumping of $7^2\text{P}_{3/2}$ has been demonstrated, the rapid quenching imposes an increased pump rate to reach threshold and a higher heat load.

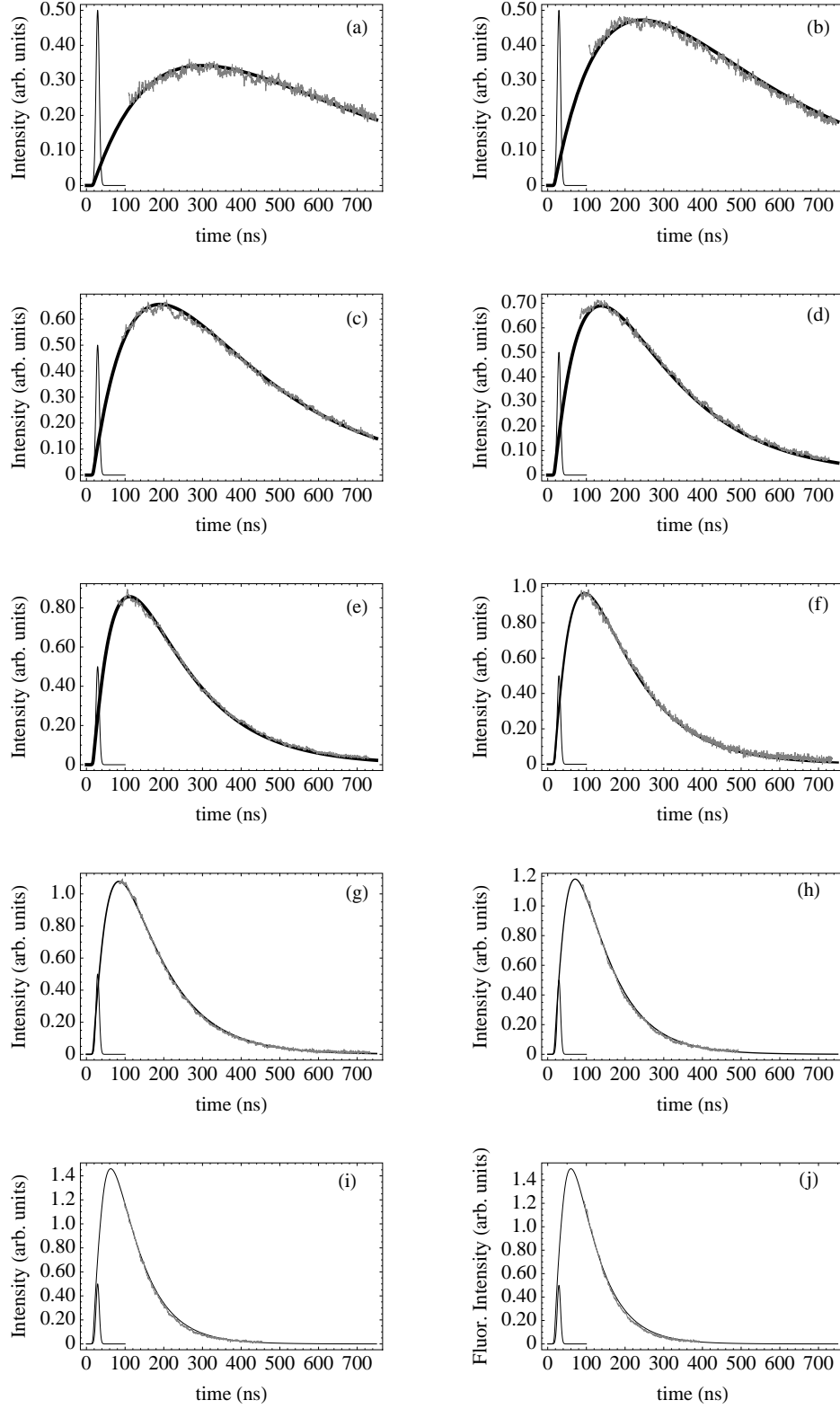


Figure 14. Simulated side fluorescence plots (solid) with data for ethane at $T=120^{\circ}\text{C}$. The buffer gas pressures in torr are: (a) 0.10 ± 0.001 , (b) 0.150 ± 0.001 , (c) 0.20 ± 0.002 , (d) 0.30 ± 0.003 , (e) 0.40 ± 0.004 , (f) 0.50 ± 0.005 , (g) 0.60 ± 0.006 , (h) 0.80 ± 0.008 , (i) 1.00 ± 0.01 , (j) 1.10 ± 0.01

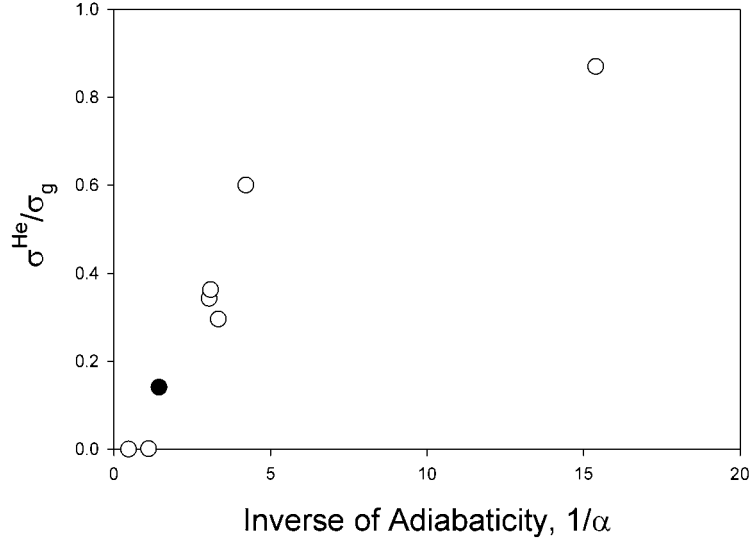


Figure 15. Scaling of the fine structure mixing cross-sections, σ_{21} , with adiabaticity for He collisions with the lowest ^2P states of Cs, Rb, K and Na, and the higher excited $n=7,8$ ^2P and $n=5^2\text{D}$ states of Cs, (\circ) prior data [68, 48, 77] and (\bullet) present result for Cs 7^2P .

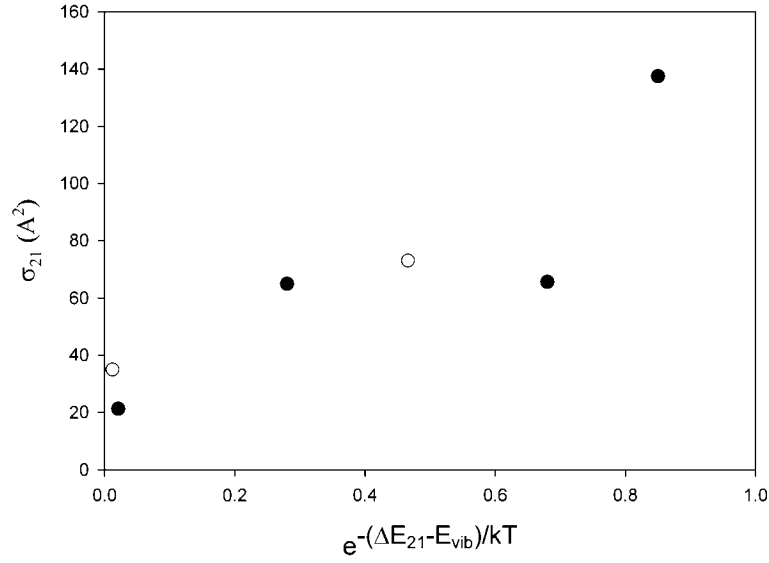


Figure 16. Scaling of fine structure mixing cross-sections with vibrational energy defect for (\bullet) Cs $6^2\text{P}_{3/2,1/2}$ [68] and (\circ) Cs 7^2P (present results). Buffer gases include CH_4 , C_2H_6 and C_2F_6 .

IV. Demonstration of a 459 nm, Pulsed, Optically Pumped Cesium Vapor Laser

Abstract

We report on the demonstration of a pulsed cesium vapor laser operating in the blue via direct optical excitation of the $7^2P_{3/2}$ state. The cesium laser may be considered a three-level visible analog to the near infrared diode pumped alkali laser (DPAL). The $6^2S_{1/2}$ – $7^2P_{3/2}$ pump transition is collisionally broadened by helium. Population is rapidly transferred to the $7^2P_{1/2}$ state using ethane and lasing was observed on the 459.3 nm $7^2P_{1/2}$ – $6^2S_{1/2}$ transition. The best results were found with 550 Torr of helium and 100 Torr of ethane at cell temperatures from 90–110°C. Using this setup, the maximum slope efficiency (0.45%) and lowest threshold pump energy (10 μ J/pulse) were obtained. The maximum output energy was 3.3 μ J/pulse, comparable to previous two-photon pumped blue laser demonstrations. A red-shifted stimulated Raman scattering (SRS) beam was present in some conditions. Weak blue emission at 459 nm was also observed using 200–500 Torr of helium alone. A time-dependent rate equation model was developed to aid in the discussion of the intermultiplet mixing and strong infrared radiative transitions inherent in this system. A scalable alkali laser system operating in the blue near the Jerlov minimum has several possible communications, optical storage, color display and remote sensing applications.

Introduction

The diode pumped alkali laser (DPAL) has been the subject of intense study during the past ten years. [50, 99, 66, 104, 89, 58, 49] DPAL systems retain many of the benefits of a gas laser, such as convective cooling and excellent beam quality, while enjoying the efficiency and convenience of electrically driven systems. These lasers

appear promising for scaling to high average power. For example, a rubidium laser pumped by a 1.28 kW diode stack with a 0.35 nm bandwidth has recently achieved 145 W average power. [104] Output powers in a cw cesium DPAL have reached 48 W [100] with slope efficiencies as high as 81%. [99] Scaling to pump intensities of greater than 40 kW/cm² while retaining performance near the quasi-two level ideal limit have also been demonstrated. [89] Indeed, scaling to greater than 1 MW/cm² has been achieved in potassium with greater than 10% slope efficiency. [41] The alkali metals offer several advantages when used as a gain medium for an optically pumped laser. The low vapor pressure of both cesium and rubidium results in sufficient ground state concentrations ($>10^{13}$ atoms/cm³) at temperatures of 100-120°C. The optical cross sections are large and support lasing in short cavities (≈ 1 –10 cm). The rapid spin orbit mixing rates allow for efficient optical recycling of alkali atoms with as many as 10^{10} laser photons generated per atom per second. [58] Finally, the fine-structure splitting of the alkali 2P states for K, Rb and Cs are 57, 238 and 584 cm⁻¹, respectively, resulting in quantum efficiencies of 95-99%.

Optically pumped alkali metal vapors can also produce coherent radiation in the blue. Fig. 17 shows the relevant energy levels for Cs lasers. Three general approaches have been pursued: (1) intracavity frequency doubling, (2) two pump laser schemes, and (3) coherent up conversion or lasing without inversion methods. Intracavity doubling of the Cs DPAL using a PPKTP crystal achieved 0.6 W and 4% efficiency in a cw experiment. [101] A similar approach achieved 40 mW at 397.4 nm in a Rb system. [67] Beach, et.al. proposed a two-photon pumped blue cesium laser using the $6^2S_{1/2}$ – $6^2P_{3/2}$ and $6^2P_{1/2}$ – 6^2D_J transitions and lasing on the 455/459 nm $6^2S_{1/2}$ – 7^2P_J transition. [64]. They found that the decreased optical cross section of the second step pump transition due to pressure broadening was the likely cause of the device’s failure to lase. Shultz, et.al. demonstrated cw lasing in Cs using two continuous-wave diodes

at 852 and 917 nm, resulting in 4 μ W of 455 nm output. [81] Frequency upconversion in Rb vapor by two color pumping at 780 nm and 776 nm produced 5.2 μ m emission, followed by a coherent blue beam at 470 nm. [93] Powers of up to 1.1 mW in the blue with pump powers of 15 mW have improved the efficiency from earlier lasing without inversion (LWI) demonstrations. [103, 102, 7, 56] The upconversion was attributed to four wave mixing. [7] Finally, a pulsed laser operating at either 455 or 459 nm with 0.4% conversion efficiency was demonstrated by our group using a single pump laser tuned to the two-photon $5^2S_{1/2}$ – 5^2D_J transition in both Rb and $6^2S_{1/2}$ – 6^2D_J in Cs. [90] In that experiment, the upper laser level was populated by radiative transfer from the S or D state. These single pump wavelength systems have an advantage in that no buffer gas is required and thus quenching rates and chemical reactivity are not an issue. In this paper we demonstrate coherent 459 nm emission is also possible via direct optical excitation of the $7^2P_{3/2}$ state using buffer gases to create a three-level analog of the infrared DPAL, in contrast with nonlinear pumping schemes. A surrogate dye laser was used to pump the gain medium since blue diode lasers with sufficient intensity to produce an inversion are not currently available.

A blue laser operating at 459 nm is near the Jerlov optical window [85] in seawater. Underwater sensors for oceanographic data, offshore exploration, and pollution monitoring would be greatly aided by a laser communication network. [54] A compact, low diffraction blue laser may find additional applications for optical data storage, color displays, and submarine communication. [70]

Experiment

The experimental setup used in this demonstration was similar to other DPAL lasers and is shown in Fig. 18. A pulsed dye laser (Continuum ND6000), with up to 8 mJ in a 10 ns pulse at 10 Hz was tuned to the cesium $7^2P_{3/2}$ – $6^2S_{1/2}$ (455 nm)

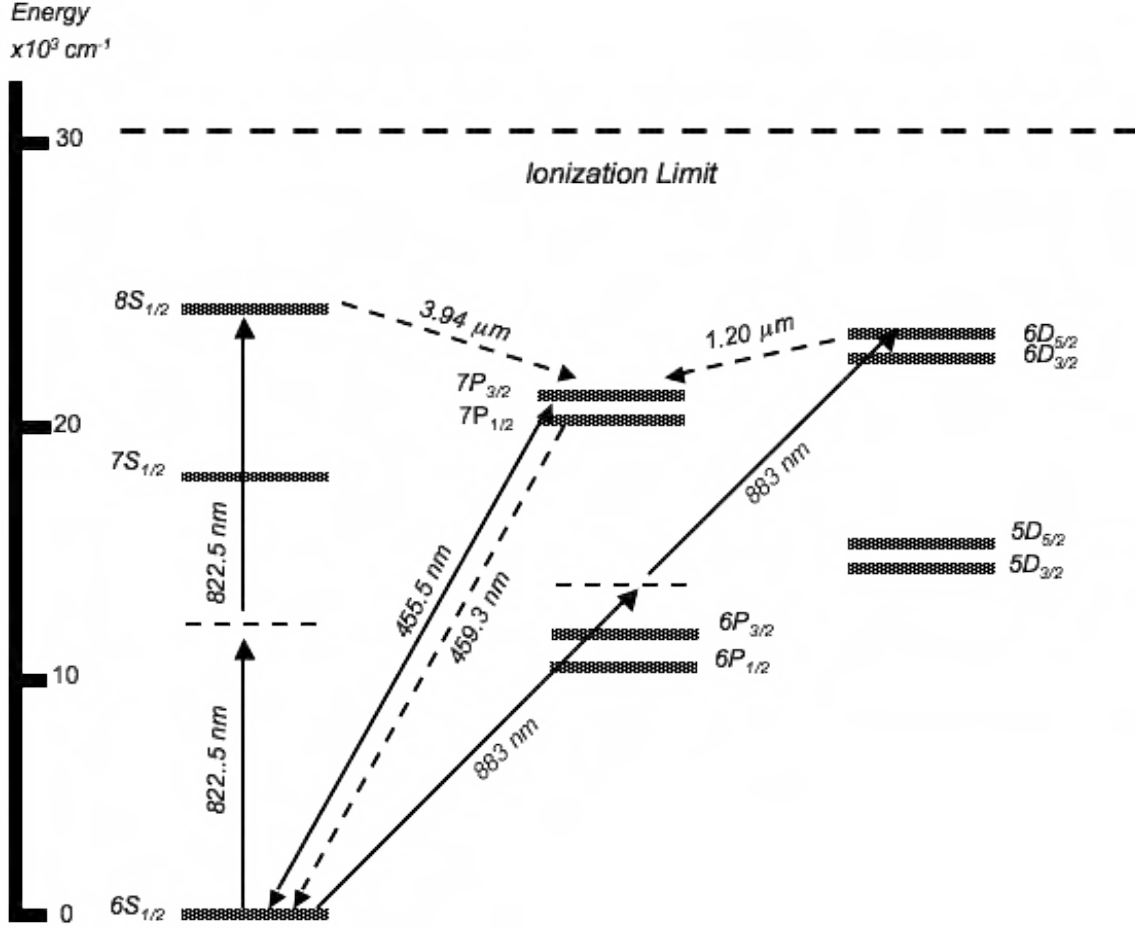


Figure 17. Energy levels and wavelengths relevant to the Cs DPAL. Virtual states for two-photon transitions are denoted as dashed lines. Solid lines are pump transitions and dashed are radiative transitions. Fine-structure spacing is not to scale.

transition. The pump bandwidth was 2.1 GHz. The pump laser is tunable over the blue spectrum using Coumarin-460 dye (Exciton, Inc. C-460). The cesium vapor was contained inside a 2.5 cm long Pyrex cell with a diameter of 2.5 cm. Quartz windows were mounted at normal incidence. Attached to the bottom of the cell was a temperature controlled cold finger filled with liquid cesium. The unfocused pump beam shape was ovoid with a major axis of about 4 mm and a minor axis of 2 mm. The pump beam was focused into the cell by a 100 mm focal length lens after being passed through a pinhole. The maximum output energy, measured just before the pump beam entered the cell was 0.72 mJ/pulse. Within the alkali cell the pump

beam is well collimated with an area of about 0.032 cm^2 . Research grade (99.999%) helium, methane and ethane were filled at room temperature through a teflon-coated valve attached to the top of the cell. Buffer gas pressure was measured with Baratron capacitance manometers (Model #690A) with 1000 Torr range. This setup permitted independent cell and cold finger temperatures as well as the buffer gas admission over a wide range of pressures. To reduce the possibility of cesium condensation on the windows, the aluminum heater block was extended to a point several centimeters longer than the cell. The flat high reflector and output coupler (Lattice Electro Optics, Inc. ROC = 25 cm) form a stable 48 cm cavity. We tested several output couplers with reflectivities varying from 50-99%. The most consistent and repeatable performance was with the 90% output coupler. The laser output and pump beams were separated using a polarizing beam splitting cube. The output beam was directed into a 0.3 m monochromator (McPherson 218) coupled to an uncooled RCA C31034 PMT and 1 GHz oscilloscope for time-resolved spectral analysis of the pump and laser beams. The monochromator was set to a resolution of 0.5 nm. Pump power output was measured on a Coherent PM-10 power meter and laser power output was measured on a Thorlabs S120 photodiode power meter.

Results

A laser beam associated with stimulated emission on the $7^2\text{P}_{1/2}$ - $6\text{S}_{1/2}$ blue transition at 459.3 nm was observed after optical excitation to the $7^2\text{P}_{3/2}$ level at 455.5 nm. Using helium only at pressures of 200-400 Torr, a weak blue beam was observed. However, using a mixture of helium and ethane at pressures of 550 Torr and 100 Torr, respectively, the 459 nm emission was much stronger and repeatable over several experiments. Fig. 19 illustrates the pump pulse and resulting blue laser output pulses for four cesium vapor densities (cell temperatures). For a pump pulse energy

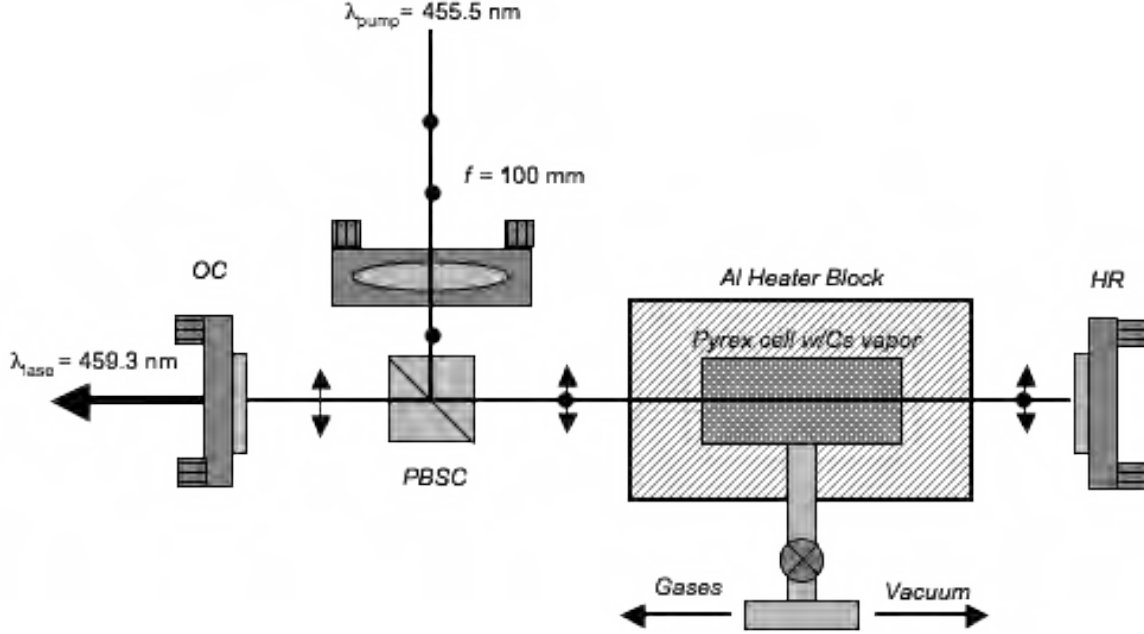


Figure 18. Experiment Layout. A pyrex cell with Quartz windows filled with cesium vapor was enclosed in an aluminum heater block. The pump beam was focused into the cell using a 100 mm lens and the polarizations were separated using a polarizing beam splitting cube (PBSC). The output coupler (OC) was a 25 cm ROC with varying reflectivity. All optics were coated for 455 nm.

of 0.72 mJ in a 0.032 cm^2 spot, the peak pump intensity was 2.12 MW/cm^2 . The maximum output laser energy per pulse was $3.3 \mu\text{J}$ and was observed to increase with an increase in Cs concentration. The output pulses are delayed from the pump pulse by 4 -8 ns.

In Fig. 20 we show the radial extent of the output beam. We calculated the divergence assuming that $\theta = 2 \arctan(d_{far} - d_{close}/2l)$, where d_{far} and d_{close} are the spot diameters at the exit of the cavity and at about $l=2$ meters. The divergence angle was $\approx 4 \text{ mrad}$. If the beam was purely Gaussian, the divergence angle could be calculated by $\lambda/\pi w$, where w is the beam waist. For this calculation we assume the beam waist is at the output coupler, d_{close} . M^2 may be calculated from $M^2 = \pi w \theta / 2\lambda$, and this gives an M^2 value of 13.5, indicating several lower-order modes achieved threshold.

From the pulse shapes in Fig. 19, we can determine the slope efficiency, pump

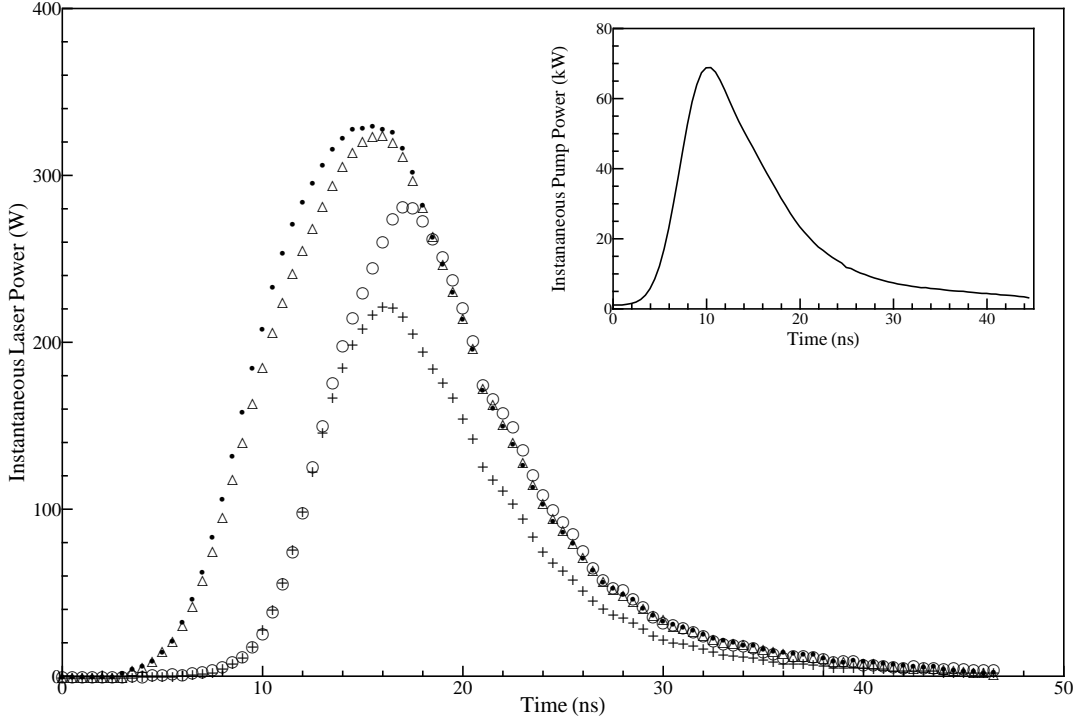


Figure 19. Instantaneous laser output power for four Cs concentrations. $T = 85^{\circ}\text{C}$ (+), 90°C (o), 100°C (Δ), 110°C (\bullet) and pump laser (inset)

threshold and photon buildup time for each temperature. Figure 21 converts the observed pulse shapes to output intensity as a function of input intensity for several pairs of pump and output laser pulse shapes. If we assume that the output intensity is simply delayed from the pump intensity by a fixed photon buildup time, the hysteresis can be largely removed. This delay can be thought of as the photon buildup time which is inversely proportional to the gain, γ . At higher alkali concentrations the hysteresis is larger and a single time delay between the output and input pulses is inadequate to capture the full dynamics. In particular, the early rise of the output intensity exceeds the long-time linear response. Even so, the plots of Fig. 21 do provide an estimate of threshold, slope efficiency and photon build-up time.

The buildup time, τ_{ϕ} , decreases with an increase in γ , τ_{ϕ} is proportional to $(c\gamma)^{-1}$. τ_{ϕ} decreases with Cs density corresponding to an increase in gain as shown in Fig. 22

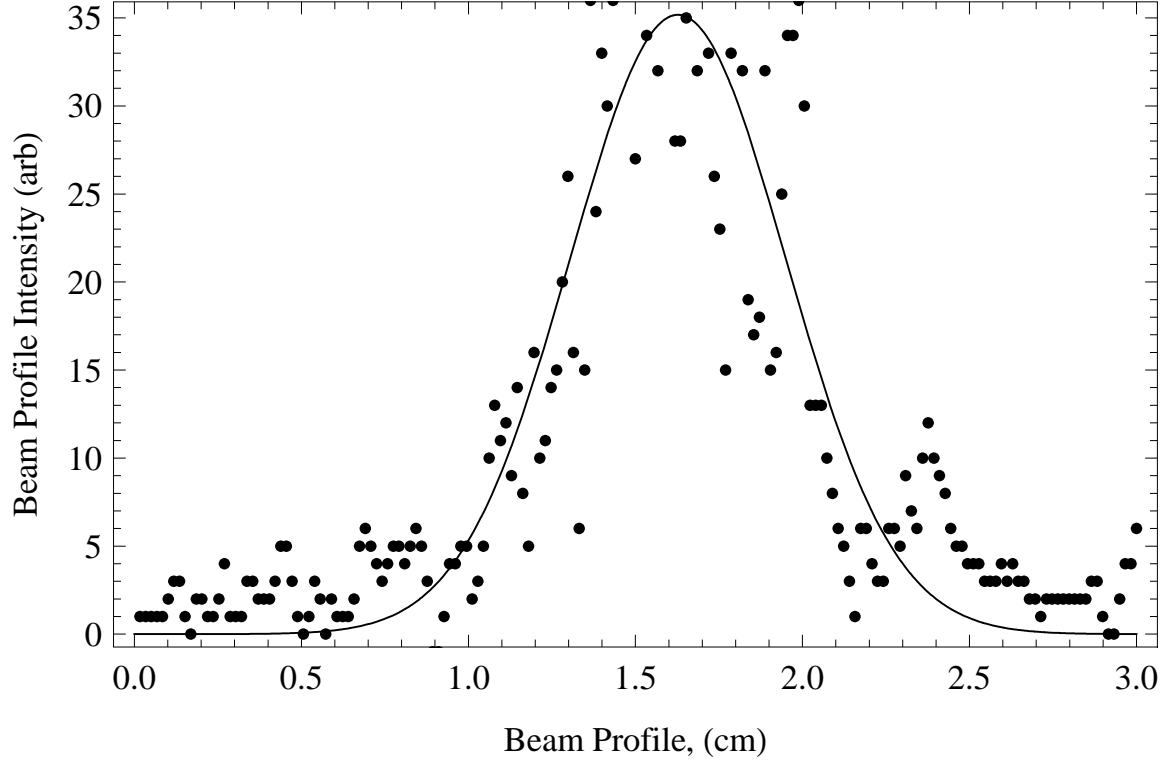


Figure 20. Intensity profile of blue laser beam. The solid line is a least squares fit to a Gaussian. The divergence angle, θ is roughly 4 mrad, resulting in an M^2 value of 13.5.

The delays are short, consistent with the high gain in alkali metal vapor lasers. The threshold pump intensity is low. At the peak pump intensity, the system is pumped to many multiples of the threshold value. An estimate of threshold intensity from the intercepts in Fig. 21 yield values of 20 - 270 kW/cm², or 6 - 85 μ J per pulse as shown in 23. At 0.72 mJ per pulse, the system is pumped to more than 10 times threshold. Threshold appears to decline with cesium concentration. These results are consistent with Page, et. al who reported this effect in the near infrared Rb DPAL.[63] Further increases in temperature are likely to increase threshold as the pump must deplete the ground state in this three-level system. Slope efficiencies increase to almost 0.45% at higher cesium concentration, as show in Fig. 23.

The ability of a DPAL system to scale is proportional to the number of cesium atoms that can be recycled for the duration of the pump pulse. Recycling is defined

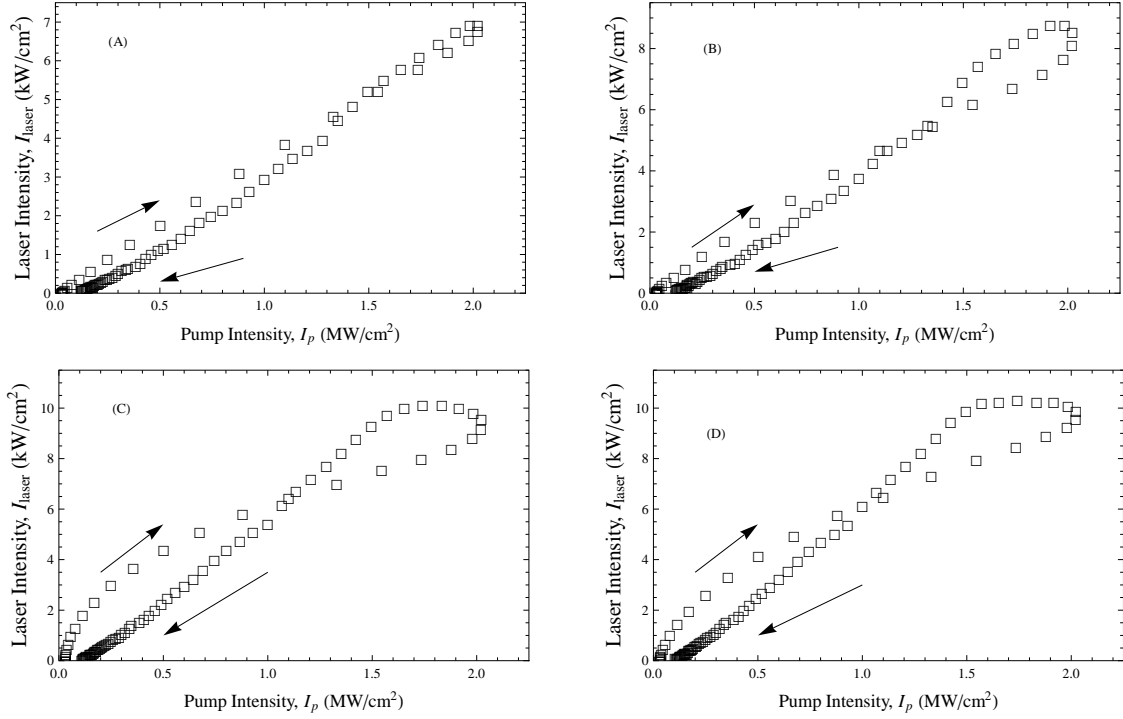


Figure 21. Measured pump intensity, I_p plotted against laser output intensity, I_l for four temperatures (A) 85°C, (B) 90°, (C) 100°, (D) 110°. The arrows indicates the direction of buildup for all cases. The photon buildup time was subtracted out for all cases, resulting in slopes that approximate the slope efficiency.

as the process where an excited cesium atom returns to the ground state after spin orbit relaxation and stimulated emission. The blue laser output pulses in Fig. 19 have a FWHM of 10-12 ns. The spin orbit mixing rate for Cs $7P_J$ and ethane at 100 Torr is on the order of 0.75 ns. Thus, for each pulse, the excited atoms can be recycled about 13 times during the pump pulse. The pumped volume of this cell is 0.08 cm^3 and the number of excited Cs atoms at 120°C is about 4.88×10^{12} atoms. For a pump energy of 0.72 mJ, the number of pump photons is $\approx 1.65 \times 10^{15}$. The number of pump photons is more than 300 times greater than the number of cesium atoms and thus, these photons are not able to contribute to the inversion. Therefore, the number of cycles available is too small and in these conditions, the lasing mechanism is bottlenecked. The wasted pump photons are a significant contributor to the poor

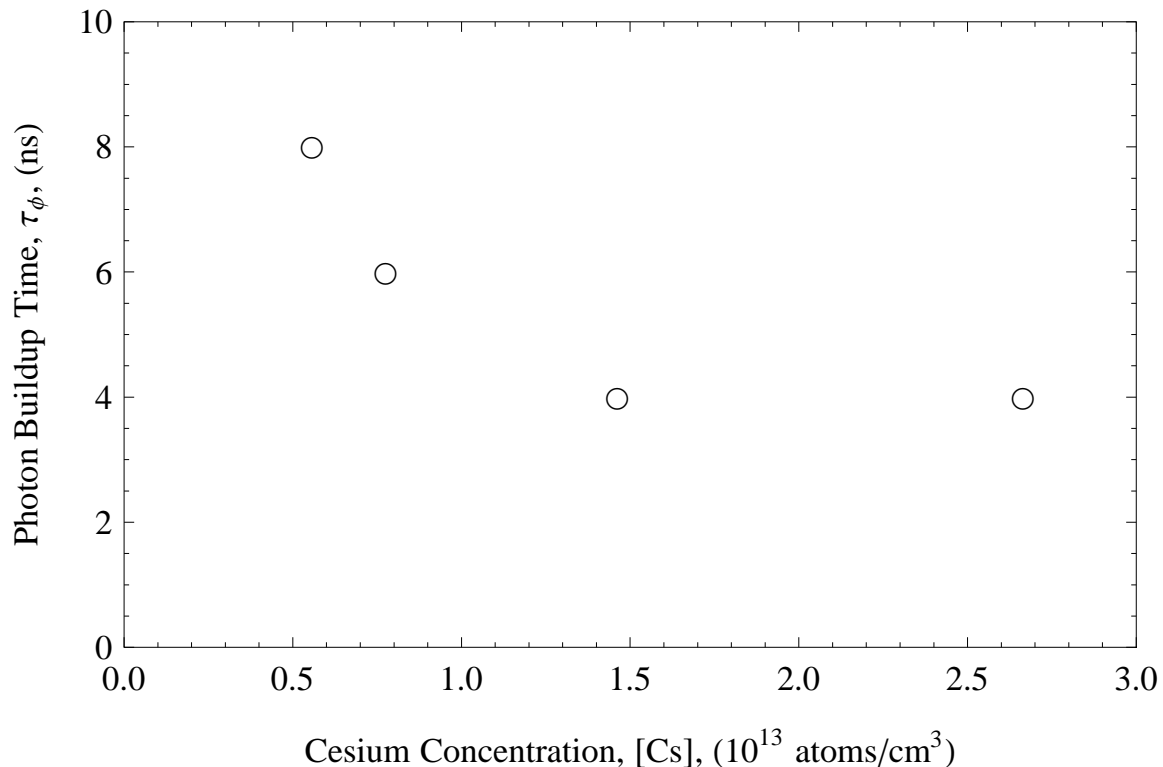


Figure 22. Photon build-up time as a function of cesium concentration.

slope efficiency observed in this system.

A periodic modulation is observed in the tail of the pulse of Fig. 19 and the Fourier spectrum is presented in Fig. 24. The oscillations exhibit features at 240 and 320 Mhz. The $7^2P_{1/2}$ state has two hyperfine levels ($F = 3, F=4$) separated by about 400 Mhz. While Doppler shifted hyperfine beating of the lower level has been observed [34], the current pump linewidth is large (2.1 GHz) relative to the Doppler width (800 MHz). The longitudinal mode spacing of the current stable resonator is 312 MHz and the higher frequency component (320 MHz) appear to be associated with longitudinal mode beating. The large observed beam divergence and corresponding value of $M^2 = 13.5$, suggests lasing on multiple transverse modes. Transverse mode beating may explain the lower frequency component (260 MHz).

We also observed a red-shifted blue emission around 460 nm, which we attributed

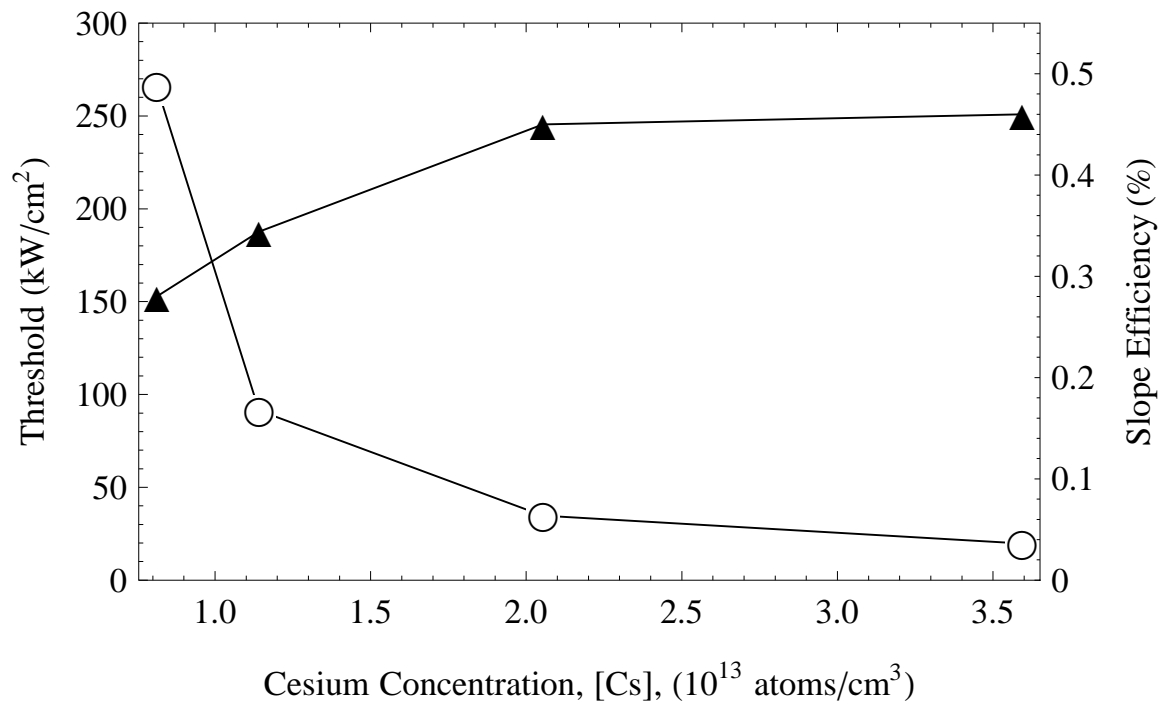


Figure 23. Laser threshold (○) and slope efficiency (▲) as a function of Cs density

to Stimulated Raman Scattering (SRS). SRS has been observed in several experiments where optically pumped alkali vapor was mixed with a buffer gas.[45, 46, 47, 44] These nonlinear processes have been described as competitors to lasing in alkali-vapor lasers. Indeed, our group observed SRS and other nonlinear processes competing with the three-level lasing mechanism in a potassium/helium laser.[41] We found that at low buffer gas pressures (< 100 Torr), SRS processes dominated the DPAL lasing mechanism in these Potassium systems.

Discussion

Rate Equations.

Interpretation of the present results is aided by a set of rate equations, first developed for use with infrared DPALs. [105, 36] We extended these equations, adding terms

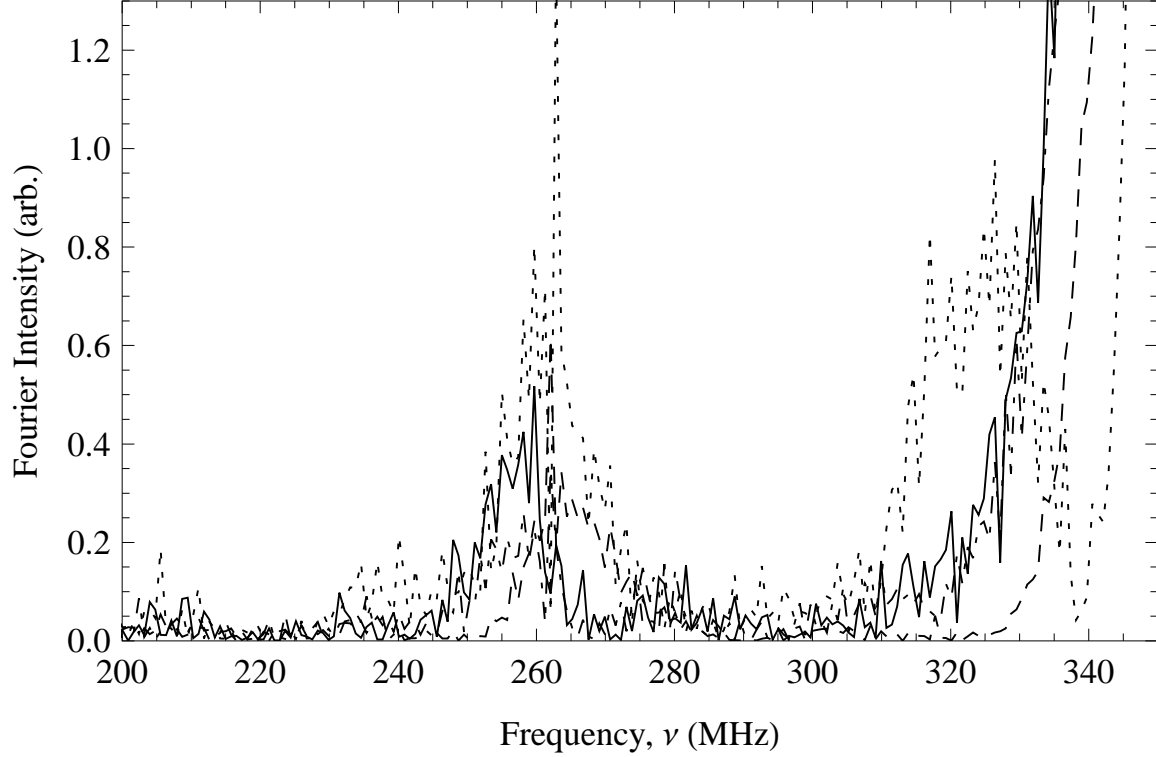


Figure 24. Fourier spectrogram of the output pulse. The oscillations in the tail of the pulse are centered around frequency of about 260 MHz for (---) 85°C, (···) 90°C, (·-·) 100°C and (—) 110°C. The longitudinal mode spacing of the cavity, $\nu = c/2L$ is 321 MHz.

describing population transfer due to intermultiplet quenching and spontaneous emission from nearby energy levels. The levels in the model correspond to the atomic levels of cesium in Fig. 17. We refer to the states $7P_{3/2}$, $7P_{1/2}$, $7S_{1/2}$, $6P_J$, $6S$ as N_2 , N_1 , N_3 , N_4 and N_0 , respectively. The term $\Psi(t)$ represents the longitudinally-averaged intracavity intensity of the laser field. The Einstein A coefficients for the transitions were chosen from the literature and range from $0.107\text{-}32.79 \times 10^6 \text{ s}^{-1}$. [30, 37, 87] The fine structure mixing rate coefficients are defined as:

$$k_{12} = \frac{g_2^2}{g_1} \exp(-\Delta E_{21}/kT) k_{21} = \rho k_{21} \quad (28a)$$

$$k_{21} = \sigma_{21}^{He} \bar{v} [He] + \sigma_{21}^{CH_4} \bar{v} [CH_4] \quad (28b)$$

where the relative speed of the collision partners is defined by the temperature and collision pair reduced mass, μ and $\bar{v} = \sqrt{8kT/\pi\mu}$.

The pseudo first-order quenching rates in the model are denoted by Q and assumed to be equal for each fine structure level. ξ is an adjustable parameter that represents the fraction of the population quenched from the pumped or upper laser level, N_1 or N_2 to ground, N_0 . We chose to have the balance $(1-\xi)$ of the quenched population fill the N_3 level, since ethane has many PQR branch rovibrational transitions from 2970-3000 cm^{-1} due to the C-H stretching mode [5]. The energy defect of the $7P_J-7S_{1/2}$ transition is 3230 cm^{-1} ($J=1/2$) and 3411 cm^{-1} ($J=3/2$), respectively, making a resonant E-V transfer process a strong candidate.

The set of rate equations below are described in terms of the longitudinally averaged intensities for the pump, $\Omega(t)$ and the laser, $\Psi(t)$:

$$\dot{N}_0 = \frac{-\eta\Omega}{l_g h\nu_P} + A_{20}N_2 + A_{10}N_1 + A_{34}N_3 + A_{40}N_4 \quad (29)$$

$$+ \xi Q (N_1 + N_2) + \sigma_{10} (N_1 - N_0) \frac{\Psi}{h\nu_L}$$

$$\dot{N}_1 = k_{21}N_2 - \rho k_{21}N_1 - A_{10}N_1 - QN_1 \quad (30)$$

$$- \sigma_{10} (N_1 - N_0) \frac{\Psi(t)}{h\nu_L}$$

$$\dot{N}_2 = \frac{\eta\Omega}{l_g h\nu_P} - A_{20}N_2 - k_{21}N_2 + \rho k_{21}N_1 - QN_2 \quad (31)$$

$$\dot{N}_3 = (1 - \xi) Q (N_1 + N_2) - A_{34}N_3 \quad (32)$$

$$\dot{N}_4 = A_{34}N_3 - A_{40}N_4 \quad (33)$$

$$\dot{\Psi} = (rT^4 \exp[2\sigma_{10}l_g(N_1 - N_0)] - 1) \frac{\Psi(t)}{\tau_{rt}} + \frac{c^2\sigma_{10}h\nu_L}{l_g} N_1 \quad (34)$$

Additional definitions and baseline values for the parameters in these rate equations is provided in Tab. 10. The pump source term, $\Omega(t)$ represents the averaged

pump intensity after two passes through the cavity: [98]

$$\Omega(t) = I_p(t) \left(1 - \text{Exp} \left(2 \sigma_{10} l_g \left(N_2 - \frac{g^2}{g_0} N_0 \right) \right) \right) \quad (35)$$

with $I_p(t)$ the time dependent pump intensity represented by a Gaussian with peak intensity, I_0 :

$$I_p(t) = I_0 \text{Exp} \left(-4 \ln(2) \left(\frac{t - t_0}{\tau_p} \right)^2 \right) \quad (36)$$

Since the pressure of the He buffer gas was several hundred Torr, the laser operated in the homogeneous broadened regime. The stimulated emission cross section at line center may be computed by

$$\sigma(\nu_0, T) = A_{n0} \left(\frac{\lambda_{n0}^2}{8\pi} \right) f(\nu_0, T) \quad (37)$$

where $f(\nu_0, T)$ is the homogeneous line shape evaluated at line center calculated as $2/(\pi \Delta \nu_{hom})$ with $\Delta \nu_{hom}$ the pressure broadening of the 7P state of cesium in the presence of helium. The broadening rate, γ , is $2.85 \times 10^{-20} \text{cm}^{-1}/\text{cm}^{-3}$ [43] with $\Delta \nu_{hom} = \gamma [\text{He}]$.

Figure 25 compares the observed and modeled pulse shapes for four cesium concentrations. The single set of rate parameters in Tab. 10 is adequate to represent all the observations.

Impact of Quenching on Laser Performance.

Unlike infrared alkali lasers that utilize the lowest P states, quenching of the second P states can branch to several product electronic states. Prior studies of the quenching

Table 10. Parameters and values used to model laser performance

Variable	Name	Value	Reference
I_0	Pump Peak Intensity	2.12 MW cm ⁻²	Measured
V_p	Pump Volume	0.08 cm ³	Calculated
τ_p	Pump Pulse Duration	10 ns	Measured
η	Pump overlap factor	0.65 (dim.)	Estimated
V_c	Cavity Mode Volume (TEM00)	0.01 cm ³	Calculated
l_g	Gain Length	2.54 cm	Measured
l_c	Cavity Length	48 cm	Measured
r	Output coupler reflectivity	90%	Measured
T	Cell window transmission	96%	Measured
τ_{RT}	Cavity Round Trip (2 l_c/c)	3.2 ns	Calculated
τ_{10}	Cs 7 ² P _{1/2} lifetime	158 ns	[60]
τ_{20}	Cs 7 ² P _{3/2} lifetime	135 ns	[60]
ρ	Boltzman Factor	0.994 (dimensionless)	Calculated
$\Delta\nu_p$	Pump laser linewidth	2.1 GHz	Measured
$\Delta\nu_D$	Transition linewidth	18.5 GHz	Calculated
$\sigma_{21}^{C_2H_6}$	Ethane spin orbit cross section	110 Å ²	[17]
σ_{21}^{He}	Helium spin orbit cross section	12 Å ²	[17]
$\sigma_q^{C_2H_6}$	Ethane Quenching cross section	20 Å ²	Estimated
σ_q^{He}	Helium Quenching cross section	4 Å ²	Estimated
σ_{20}	Stimulated emission cross section	2.13×10 ⁻¹⁴ cm ²	Calculated
σ_{10}	Stimulated emission cross section	1.82×10 ⁻¹⁴ cm ²	Calculated
σ_{02}	Stimulated absorption cross section	4.26×10 ⁻¹⁴ cm ²	Calculated
σ_{01}	Stimulated absorption cross section	1.82×10 ⁻¹⁴ cm ²	Calculated
ξ	Fraction quenched to N ₀	25%	Estimated

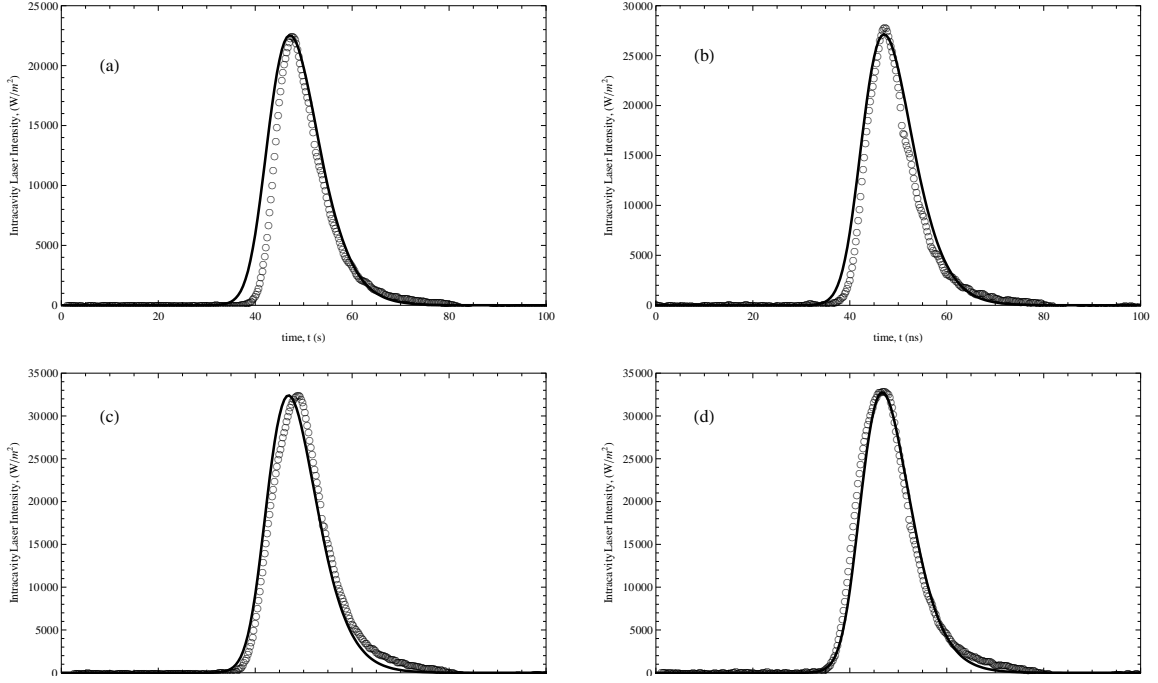


Figure 25. Simulated longitudinally-averaged intracavity laser intensity and experimental laser output pulses for four cell temperatures: (a) 85°C, (b) 90°C, (c) 100°C, (d) 110°C.

rates are limited to total removal rates, regardless of product states. [60, 23, 77]. The reported quenching cross sections were large, typically tens of \AA^2 and had error bounds comparable to the measured value. In contrast, in a recent alkali vapor spin orbit and quenching work, Zameroski [98] suggested the quenching cross sections were up to two orders of magnitude lower than previously thought, mainly due to the effects of radiation trapping not considered in previous experiments. Intermultiplet transfer for alkali–buffer gas collisions has been the focus of several studies. [65, 24, 14, 42, 53]. These studies lend support to the idea that quenching of the pumped state and upper laser level in a blue cesium laser takes place via intermultiplet transfer rather than direct quenching to ground that would require several eV of energy to be transferred to the buffer gas molecule.

To study how the populations in blue and infrared systems differ depending on the size of the quenching cross section, the rate equations, Eqs. 29-34 were solved for

the small signal (no lasing) inversion. The predicted inversion fractions are shown in Fig. 26 and Fig. 27. In both figures, we assumed the pump beam was Gaussian with a peak intensity of 100 kW cm^{-2} and a pulsewidth (fwhm) of 10 ns. We used 100 Torr of ethane buffer gas and a cesium density of $1 \times 10^{14} \text{ atoms cm}^{-3}$. For the sake of comparison we have assumed all quenching goes directly to the ground state, $\xi=1$. Quenching cross sections up to 0.3 \AA^2 have a negligible effect on the magnitude of the inversion. However, for cross sections greater than 3 \AA^2 there is a significant effect on the population inversion. In Fig. 27, the effect on potential inversion for the excited fraction, ξ that is quenched to ground is shown. For ξ less than 50%, the temporal shape and magnitude are significantly affected, especially toward the end of the pulse.

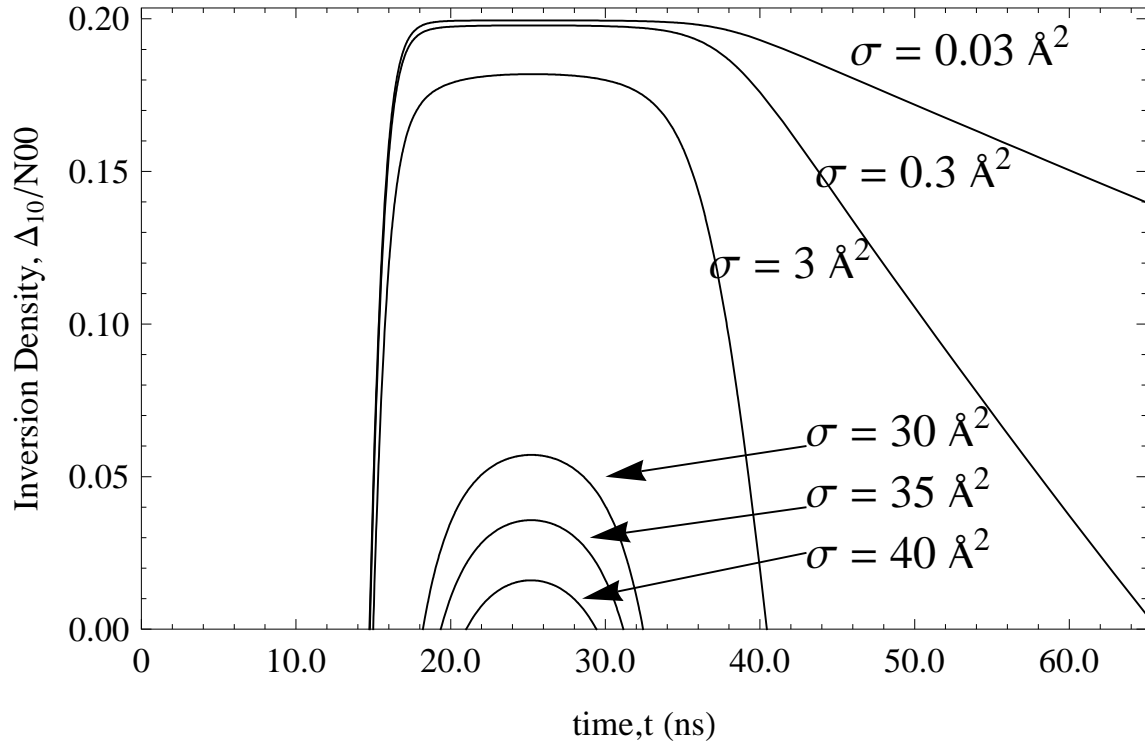


Figure 26. Predicted population inversion, Δ_{10} , as a fraction of the initial ground state concentration for a blue DPAL assuming no stimulated emission. The values of the quenching cross section, σ , represents the range of typical values found in the literature. The fraction quenched to the ground, ξ is assumed to be unity.

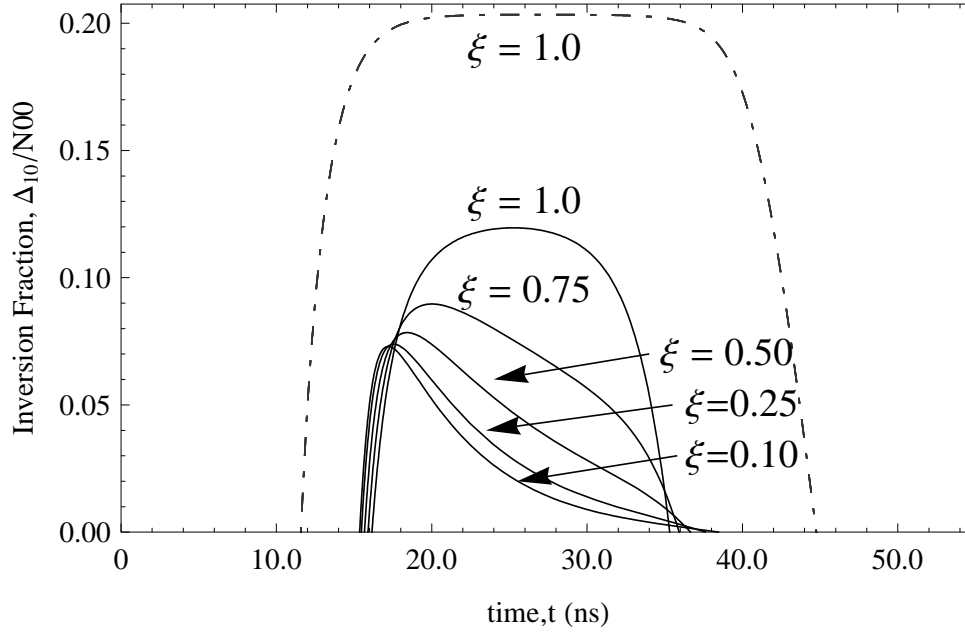


Figure 27. Predicted population inversion for several values of ξ , as a fraction of the initial ground state concentration for an infrared DPAL (- - -) and blue DPAL(—) assuming no stimulated emission. The quenching cross section for the infrared case is 1 \AA^2 and 10 \AA^2 for the blue case

To estimate the modeled output pulses as a function of the branching ratio, ξ are illustrated in Fig. 28. An increase in the fraction of atoms quenched to the ground state decreases the amplitude of the output pulse and increases the width. The precise fraction quenched to ground was not determined in this experiment. However, the pulse shapes in Fig 25 are best represented by $\xi=0.5$.

Conclusion

We have demonstrated a blue analog to the infrared DPAL laser via direct optical excitation of the 7^2P state in cesium. The maximum output energy was 3.3 \mu J with a slope efficiency ranging from 0.26 to 0.45 %. The slope efficiency was seen to rise with an increase in cell temperature, but remains poor due to the low recycling rate. The threshold for lasing was found to decrease with an increase in cell temperature with

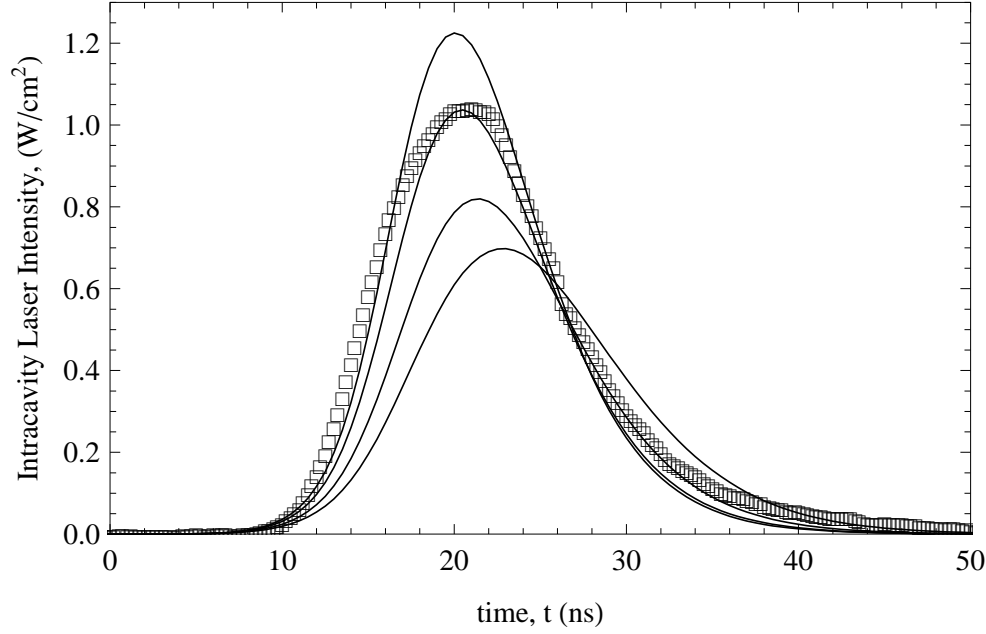


Figure 28. Simulated longitudinally-averaged intracavity laser intensity (solid lines) at $T = 120^\circ\text{C}$ for four values of ξ : 0.75, 0.50, 0.25, 0.10 from top to bottom, respectively. The experimental data at is also shown (empty squares). A decrease in amplitude and increase in pulsewidth is seen with an decrease in ξ .

the lowest threshold at 111°C of $10\ \mu\text{J}$. The branching ratio for quenching product states has a significant effect on the temporal shape of the modeled pulse. Modeling suggests the total removal rate from the $7^2\text{P}_{3/2,1/2}$ states plays a significant role in determining the laser output. If some of these deleterious effects can be overcome by increasing the pump pulsewidth or the gain length, then a blue analog DPAL may ultimately be realized. The development of blue diode pump sources with intensities of $10\ \text{kW}/\text{cm}^2$ will be required.

V. Tuneable Hyper-Raman Laser in Potassium Vapor

Abstract

When a potassium vapor cell surrounded by a stable cavity is pumped with a pulsed dye laser near the 4^2P resonances, Stokes and anti-Stokes lasing due to Stimulated Electronic Raman Scattering (SERS) is generated. When the pump is tuned about halfway between the fine structure levels of the 4^2P state, an efficient hyper-Raman process dominates, resulting in tunable laser radiation near 769 nm with a slope efficiency of about 10.4%. Up to 12 mW of red light is produced at a pump input of 232 mW. The threshold for the hyper-Raman process is about 60 mW. This type of laser may be useful for beam propagation experiments where a tuneable probe beam spectrally close to the main beam is desired.

Introduction

In the last decade, much progress has been made developing diode-pumped alkali lasers (DPAL). The DPAL is a three-level laser system that offers efficient conversion of incoherent diode pump sources into coherent laser light at several near-infrared wavelengths with high quantum efficiency due to fine-structure levels separated by less than 1000 cm^{-1} . The basic scheme relies on alkali metals (Cs, Rb, K) in mixtures with noble gases such as helium and small hydrocarbons such as methane and ethane. The usual function of the noble gas is two-fold: (1) Pressure broaden the atomic transitions to increase their spectral overlap with the pump source, (2) rapidly mix the $P_{3/2}$ state with the lower $P_{1/2}$ state. Molecular buffer gases at low pressure can also provide rapid population transfer from the $P_{3/2}$ to the $P_{1/2}$ state. Population inversion and lasing can occur between the $P_{1/2}$ and ground $S_{1/2}$ state if the quenching rates are small relative to the spin-orbit mixing rates.

Since the DPAL operates as a three level laser, the cell must be bleached. Large pump intensities are required to reach and maintain inversion. Due to these high pump intensities, nonlinear effects such as stimulated Raman scattering have become a concern since they represent a competitive process to normal DPAL operation. The intensity threshold at which these processes appear and become problematic to DPAL scalability has come under scrutiny. To date, no adverse effects have been noted in infrared DPAL systems operating in the lower 2P states. [90]

During recent experiments with a deep red (770 nm) potassium vapor laser operating on the $4^2P_{1/2}-4S_{1/2}$ transition, we noticed the production of several evenly spaced emission lines when the spin-orbit mixing gas (in this case, 1400 Torr of He) was removed. The lines maintained a constant separation of 3.41 nm while the pump was tuned through the D_1 line (770 nm) to the D_2 line (766 nm). The largest amplitudes were seen when the pump frequency corresponded to the core of either the D_1 or D_2 line and also about halfway between the two. These observations are consistent with the nonlinear mechanisms first mentioned by Sorokin [86], Bradley [15] and Anikin [10] who optically pumped potassium in vapor cells at temperatures between 240-300 °C.

In this section, I will describe the theory of the nonlinear mechanisms behind the operation of a potassium hyper Raman laser, compare the device to the traditional three-level potassium DPAL and discuss potential uses of this laser in beam propagation experiments.

Experiment

The experiment layout is shown in Figure 29 with an actual picture of the experiment in Figure 30. A 10 ns pulsed dye laser (Quanta Ray Nd:YAG and Sirah dye box) operating at 10 Hz served as the pump source. Multimode output up to 230 mW was

available with a pulsewidth of 10 ns. A mixture of methanol and LDS-765 (Exciton, Inc.) allowed the dye laser to be tuned over the entire range of the 4S–4P transition (766–770 nm). A stainless steel heat pipe 30 cm long and 2.54 cm in diameter contained about one gram of potassium metal. Sapphire windows coated for 765 nm are mounted at zero degrees. The ends of the heat pipe were cooled using an aluminum water jacket to a constant temperature of 20 °C to prevent condensation of potassium vapor and damage to the windows. The central section of the heat pipe was enclosed in an aluminum heater block controlled by a Watlow single zone heater that provided a maximum temperature of about 325 °C. The cavity was formed by a 50 cm ROC high reflector and a flat output coupler with a reflectivity of 30%. The total length of the cavity was 48 cm and the gain length of the heated zone was about 15 cm. The vertically polarized pump and horizontally polarized laser radiation were separated using a polarization beam splitting cube (PBSC). Coarse cavity alignment was performed using a He-Ne laser and fine adjustments were based on peak power output. The average output power was measured by a Coherent thermopile-type meter and the temporal shape of the output was monitored by a photodiode and oscilloscope. The spectrum of the pump and potassium laser were analyzed by an Ocean Optics spectrometer.

A series of three experiments were performed. The first was to characterize the laser spectrum from the SERS process and measure the output power at the maximum potassium density. To maximize the Raman effect, the pump laser was tuned to either the D₁ or D₂ lines. Before each data collection, the heat pipe was pumped down to mTorr levels at room temperature. After closing the isolation valves between the heat pipe and gas handling lines, we heated the cell for up to two hours to a maximum temperature of 325 °C. Once the temperature stabilized it fluctuated no more than one degree over the course of data collection. The average power of the pump beam

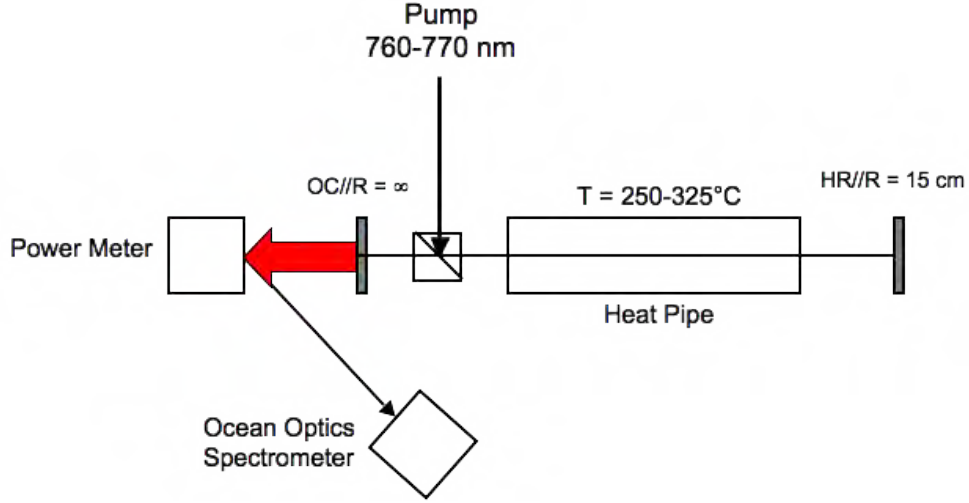


Figure 29. Schematic of experiment layout. (OC) Output coupler and (HR) high-reflector.

was swept from a minimum of 100 mW to a maximum of 230 mW in several steps. For each pump input power the spectrum and average output power were recorded. The spectrometer was calibrated so that the software measured intensity could be converted into an average power for that particular emission line.

The second experiment was performed to determine the effect potassium density had on the average output power of each emission in the Raman process. The pump power in this case was the maximum available, about 232 mW. The pump was tuned to the D_2 line and the output spectrum was recorded. The temperature was then lowered in 10°C steps until the Raman lasing was no longer detected.

The third experiment explored the three-photon hyper-Raman process. The heat pipe was operated at 325°C and the pump laser was tuned between the D_1 and D_2 lines in steps of 0.1 nm. At each step, the output spectrum was recorded. We then found a pump wavelength where the hyper-Raman process dominated the other Raman processes and varied the input pump power to measure the slope efficiency and threshold.

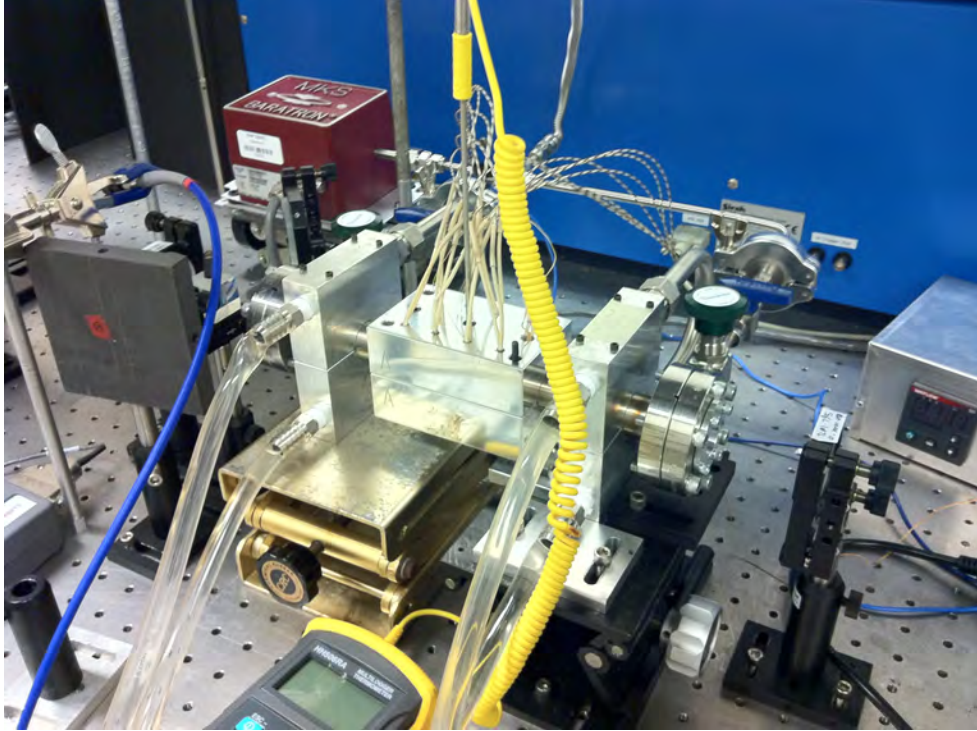


Figure 30. Photograph of potassium hyper Raman laser experiment

Results

Depending on the wavelength of the pump, different Raman processes compete for gain and are present in the output spectrum. In Fig. 31, the top left plot shows the spectral output with the pump centered on the core of the D_2 transition. First and second order Stokes emission are obvious. Further detuning to the red (clockwise in the plot grid), results in the higher orders decaying away and leaving only a strong anti-Stokes emission. When the pump is detuned to a spot near the middle of the fine structure levels, only Rayleigh scattering is seen. Finally, when the pump is tuned to the D_1 line, the higher order Stokes emissions are seen, to at least the second order.

Figure 32 shows the increase in output intensity of all Raman processes with the exception of the hyper-Raman process which is shown in a separate figure. From the plot you can see that the the pump power is only weakly attenuated at all potassium densities despite being tuned to a resonance line. This implies that the transition is

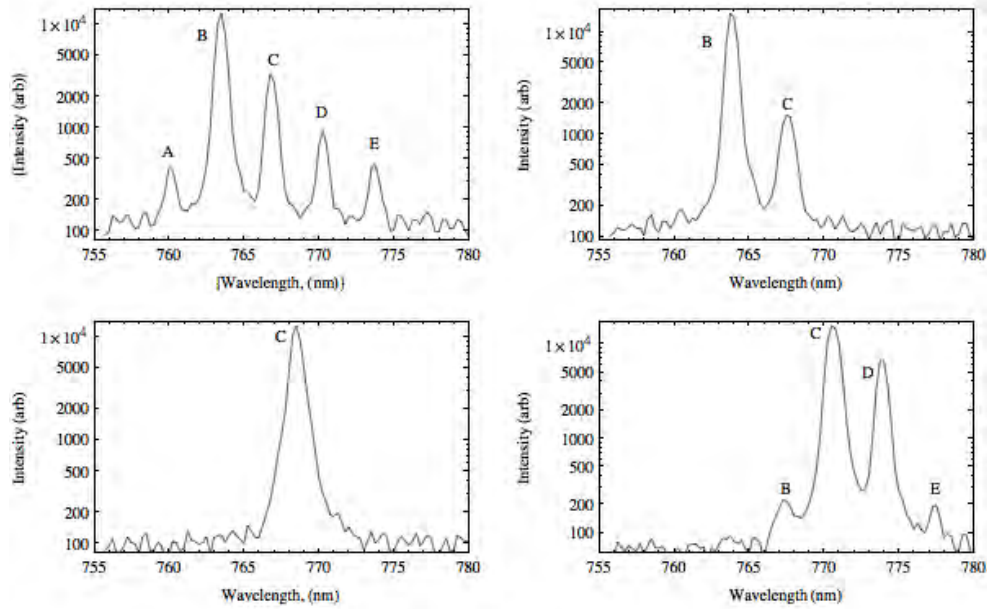


Figure 31. Semilog plot of output intensities for a specific pump wavelength showing the nonlinear features at 325°C. For all plots: (A) 2nd anti-Stokes, (B) 1st anti-Stokes, (C) residual pump, (D) 1st Stokes, (E) 2nd Stokes. Clockwise from top left: D₂ pump with multiple order anti-Stokes scattering, anti-Stokes scattering, Rayleigh scattering, D₁ pump with multiple order Stokes scattering.

fully bleached and that Raman processes are maximized at these temperatures. The 1st order anti-Stokes process is very efficient and rises rapidly with density, rolling off about halfway to the maximum potassium density. The high orders are naturally far less efficient since they use final Raman level as the starting point for a second Raman process. Since the lifetime of the 4P state is short and there is no pumping process filling the states, the population density is much lower and therefore more difficult to create the inversion necessary to begin a higher order Raman process.

In Fig. 33, the entire Raman spectrum is shown for all pump wavelengths. The intensity of each point is scaled from 0–15 mW with the higher intensities being darker. Several features are immediately noticeable. First, the spacing of the SERS processes maintain a constant separation throughout the pump range, as expected. Second, the SERS process is strongest near the resonance lines, and the higher order

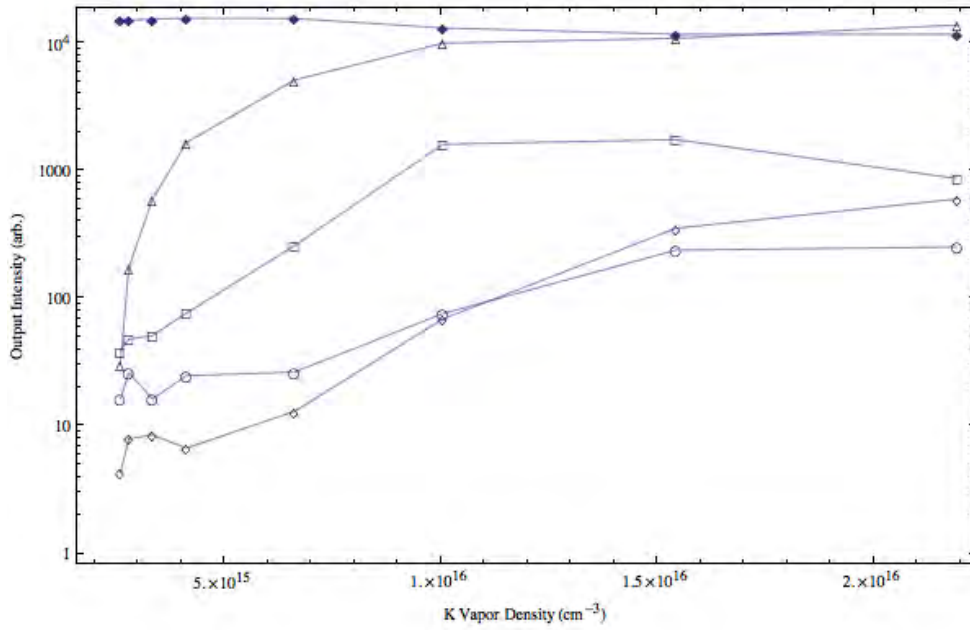


Figure 32. Average output intensity as a function of potassium density for a pump power of 232 mW. Pump (♦), 1st anti-Stokes (△), 1st Stokes (□), 2nd anti-Stokes (○), 2nd Stokes (◇)

Raman processes are only seen near the electronic resonances as mentioned above. The hyper-Raman process begins as a branch from the Rayleigh scattered pump line and increases linearly until it joins the SERS 1st Stokes line. All Raman processes appear to negate each other in a narrow region near the center between the D₁ and D₂ resonances. This is possibly due to an equal absorption of pump photons into the wings of each fine structure level, creating little to no population inversion to achieve Raman gain.

In Fig. 34, the pump wavelength was tuned from a point where the only detectable process was the anti-Stokes beam. When the pump was tuned to the red side of 767.6 nm, a second process (HRS) began to grow out of the residual pump, rapidly growing in magnitude and separation from the pump over a tuning range of 0.5 nm. The separation of the HRS line from the pump was not fixed like the SERS lines. This process has a linear tuning slope of about 2 nm/nm.

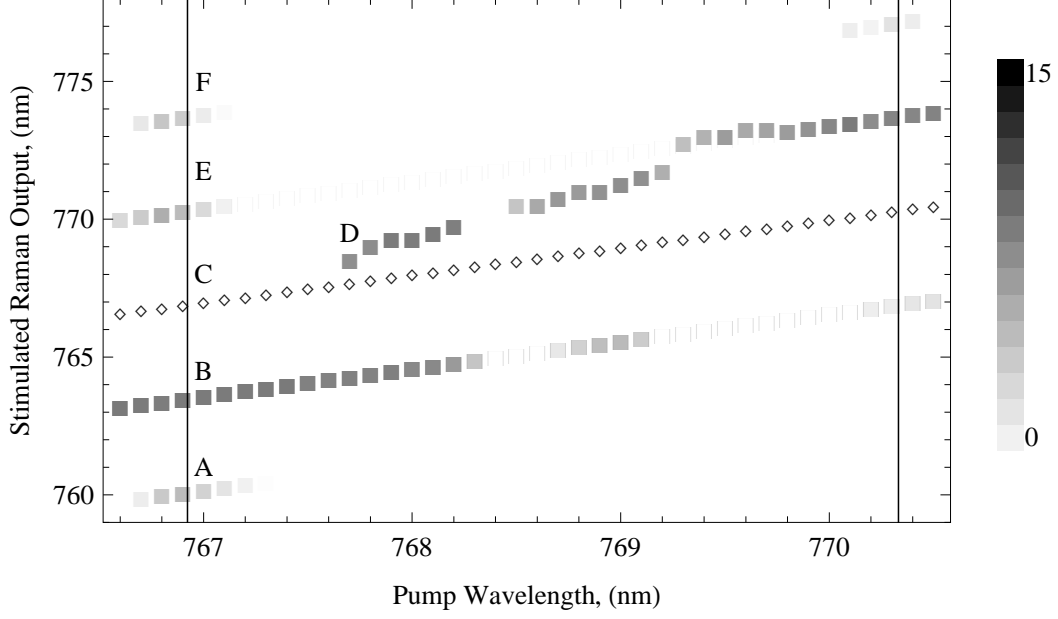


Figure 33. Output wavelength and average power in mW (given by the graylevel) for a specific input wavelength at an input power of 232 mW and temperature of 325° C. Vertical bars indicate position of D₁ and D₂ lines. (A) 2nd Stokes, (B) 1st Stokes, (C) Pump, (D) hyper Raman process, (E) 1st anti-Stokes (F) 2nd anti-Stokes.

In Fig. 35, we demonstrate that a slight tuning of the pump can alter the spectral output significantly by switching processes between SERS and HRS. The pump was first tuned to a wavelength where the only detectable process was HRS. When the pump was detuned by 0.1 nm to the red, the spectral output was observed to “hop” to the SERS process. The process was reversible with minimal hysteresis visible in the output of the spectrometer.

In Fig. 36, we characterize the performance of the hyper Raman process in terms of a laser. The threshold is high, nearly 60 mW which represents an intensity of about 20 kW cm⁻². The slope intensity is over 10.4% which is almost the same as the potassium DPAL laser operating on the same transition. The maximum output power was about 12 mW, again comparable to the pulsed potassium DPAL system using 1400 Torr of helium.

In Fig. 37, we make the comparison between the temporal shapes of a Raman

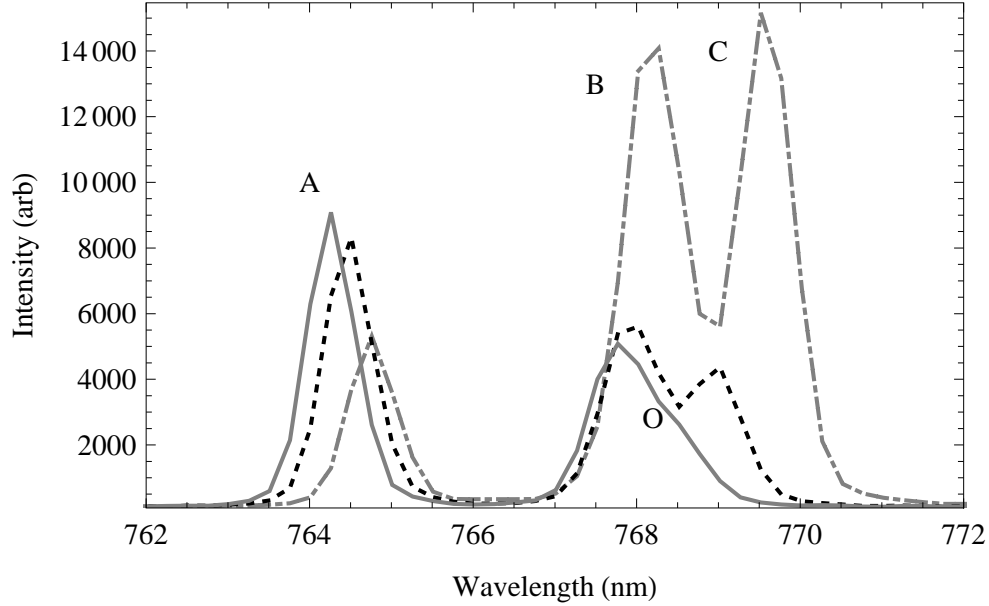


Figure 34. Onset of hyper Raman lasing. Pump wavelength: 767.6 nm (solid), 767.8 nm (dashed), 768.1 nm (dot-dash). The point (A) is the 1st anti-Stokes, (B) is the pump and (C) is the hyper Raman process. The point (O) is the initial point where the process can be seen separated from the pump beam in this spectrometer. The tuning from the pump beam is linear with a slope of 2.01 nm/nm.

output pulse and that produced by the same system with 1400 Torr of helium. With the added helium, the system acts as a DPAL laser exhibiting a pulsewidth similar to that of the pump pulse. The Raman pulse exhibited asymmetry characteristic of the way the pulse is shaped while it copropagates in the potassium vapor with the pump pulse. The front of the pulse sees a constant gain as it passes through the pump wave.

Theory

When a laser beam of sufficient intensity interacts with a two or three level atomic system near a resonance, nonlinear processes can become very efficient, converting pump photons into wavelengths not associated with electronic dipole transitions, but a virtual states. In this experiment, the potassium vapor serves as a nonlinear medium that converts pump radiation into a narrow, collimated beam of stimulated radiation whose wavelength is shifted by a fixed amount, equal to the separation of the fine

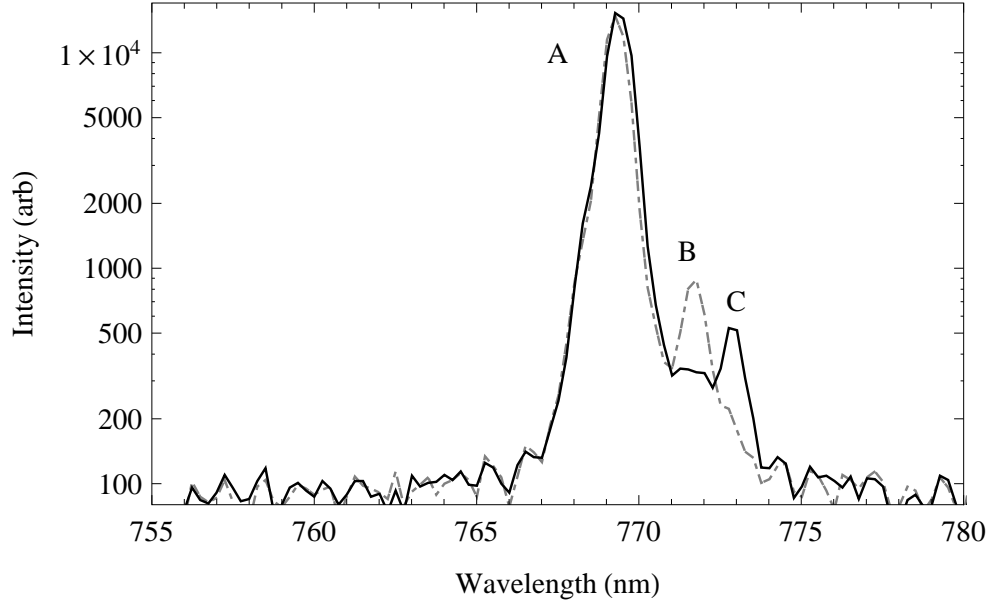


Figure 35. Evidence of process switching. Pump (A) tuning from 769.2 nm (dot-dash) to 769.3 nm (solid), results in selection of either hyper Raman (B) or SERS Stokes scattering (C). The temperature was 325 °C and the input power was 232 mW.

structure levels. One pump photon populates a real electronic state and a second pump photon scatters off of it, emitting a shifted photon and changing the final electronic level. If the final electronic state is lowered an anti-Stokes beam is created; if the final electronic state is raised, then a Stokes photon is created. This process is known as Stimulated Electronic Raman Scattering (SERS) and was first demonstrated in potassium vapor by Sorokin [86] who generated an antiStokes beam shifted by 58 cm^{-1} , the fine structure splitting of the 4^2P state. Because SERS can be very efficient near an electronic resonance, several orders of Raman emission can appear, each moving the atomic population from one real level to another through a virtual state. The SERS process is easy to identify because the orders are spaced in wavelength by the same amount. A second two-photon process, called hyper-Raman scattering, occurs when the pump photon wavelength falls in between the fine structure levels of an electronic transition. This is different from SERS since not one, but two virtual states are involved. The Raman shifted frequency is not fixed but increases linearly

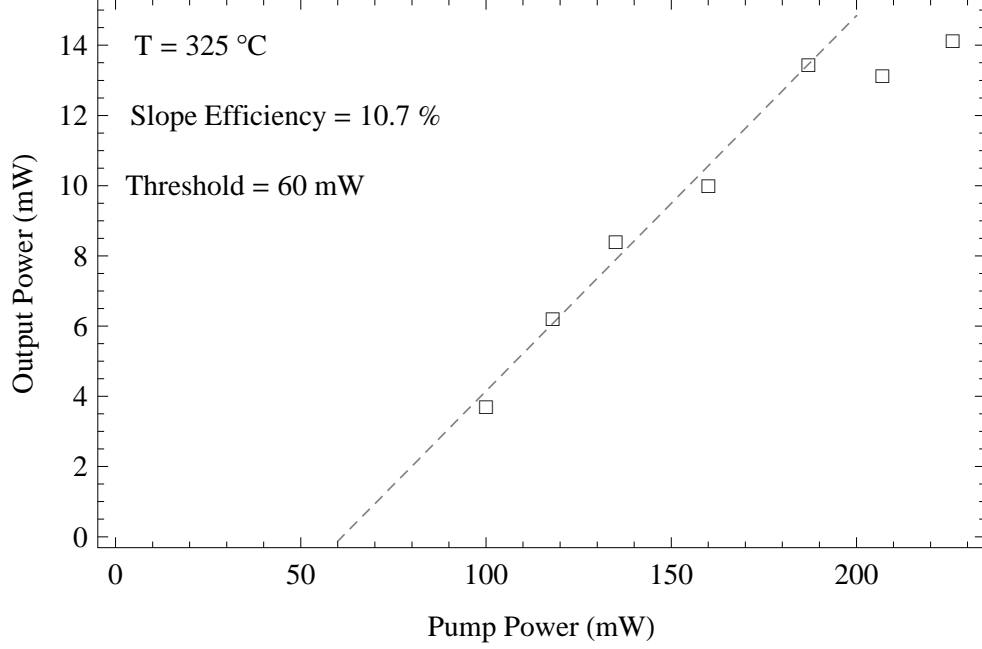


Figure 36. Input vs Output power for hyper Raman laser. Pump tuned to 768.2 nm at 325° C. The dashed line is a least-squares fit to the data. The slope efficiency was 10.4% and the extrapolated threshold is 60 mW. The maximum optical-to-optical conversion is about 7%

with an increase in pump wavelength.

The SERS process can be described using the density operator formalism where the time evolution of each real and coherent state can be written with terms describing the dephasing rate, radiative rate and the interaction Hamiltonian. For each state, the time derivative of the density operator may be written as[95], where the μ_{ij} are the dipole moments, E is the applied field, γ_{ij} are the dephasing rates, and the A_{ij} are the spontaneous decay rates.

$$\dot{\rho}_{ij} = -(\gamma_i + i(\omega_{ij} - \omega_p)) \rho_{ij} - \frac{i}{\hbar} \sum_k (\mu_{ik} E \rho_{kj} - \mu_{kj} E \rho_{ik}) \quad (38)$$

$$\dot{\rho}_{ii} = -A_{ii} \rho_{ii} - \frac{i}{\hbar} \sum_k (\mu_{ik} E \rho_{ki} - \mu_{ki} E \rho_{ik}) \quad (39)$$

For a four level system where we have states, $|1\rangle, |2\rangle, |3\rangle$ and $|4\rangle$ that represent the

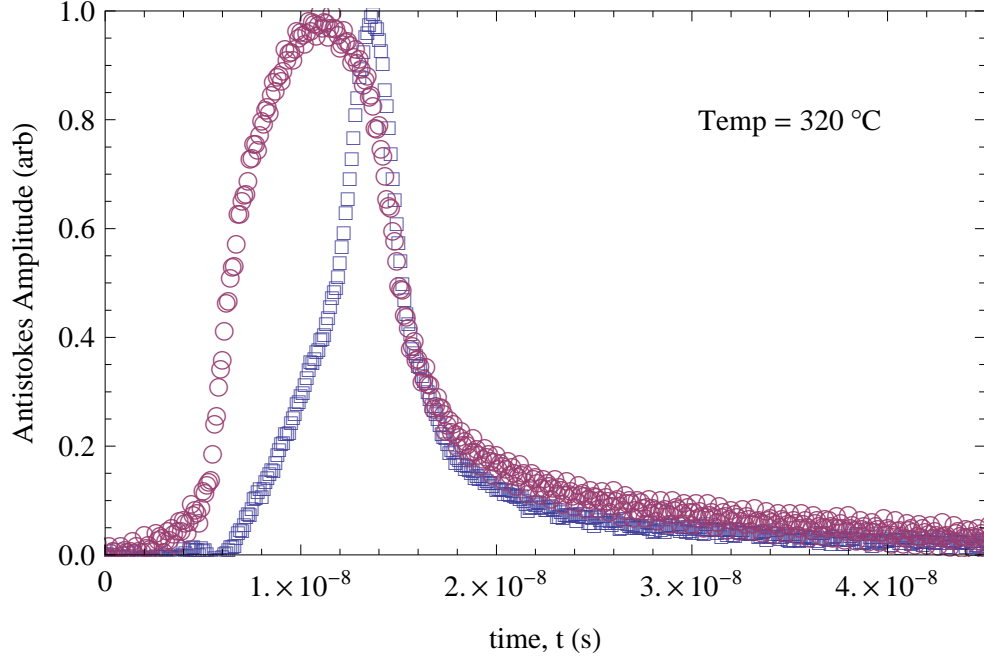


Figure 37. Temporal pulse shapes for: (o) potassium DPAL laser (770.3 nm) using 1400 Torr of He, (□) the anti-Stokes laser (763.5 nm) with no buffer gas. The FWHM of the DPAL is about 9 ns; for the Raman it is about 3 ns. The DPAL is pumped on the D₂ line and lases on the D₁ line. To achieve only anti-Stokes output, the Raman laser was tuned from 767.2 to 767.6 nm with anti-Stokes output blue-shifted by a constant 3.4 nm. The asymmetry and narrowing of the pulse is due to the copropagation with the pump pulse.

potassium $4^2S_{1/2}$, $4^2P_{1/2}$ and $4^2P_{3/2}$ and $4^2D_{3/2}$ states, respectively. Equations 38 and 39 generate a total of nine equation of motion, three for each real level and six for the off-diagonal coherent states. We have neglected terms involving ρ_{44} because the pump beam is detuned far enough such that the population density is very small compared to the other states. We also neglect terms like ω_{mm} and μ_{mm} and other terms where the dipole moment is zero due to selection rules. The potential terms in the Hamiltonian can be written using the Rabi frequency, $\Omega_{ij} = \frac{E_{ij}\mu_{ij}}{h}$, and the frequency terms can be written as $\Delta_{nm} = \omega_{nm} - \omega$ the difference between the transition and the pump or Raman wavelength. By doing so, we are making the rotating wave approximation. We assume a strong pump pulse that results in $\rho_{11}(0) = 0.33 N_0$ and $\rho_{mm}(0) = 0.66 N_0$, where N_0 is the initial ground state density, and $\rho_{mm}(0)$ is the initial value of the

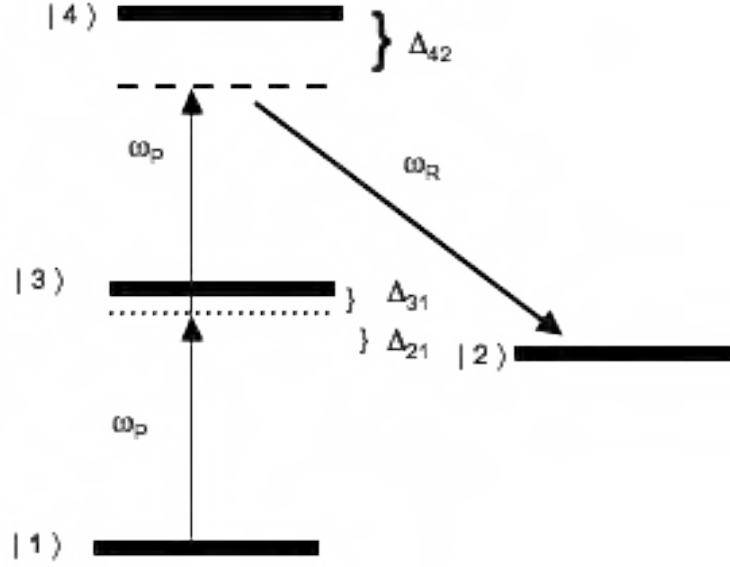


Figure 38. Energy levels involved in a λ -type Raman process. In SERS, the ground state $|1\rangle$ is first populated by a pump photon, ω_p . A second pump photon scatters off a virtual state below $|4\rangle$ generating an antiStokes photon (or Stokes if $E_2 > E_3$) and increasing the population of the final state, $|2\rangle$. The separation between $|4\rangle$ and the virtual level is given by Δ_{42} and the detuning between the pump and $|3\rangle$ and $|2\rangle$ is given by Δ_{31} and Δ_{21} , respectively.

pumped level just after the strong pump pulse. For this simulation we use a total potassium density of 10^{19} m^{-3} . We assume that $\gamma_{mn} = \gamma$ and that the dephasing rate is equal to the Doppler broadening rate. The radiative rates A_{nm} are taken from the literature[76].

$$\dot{\rho}_{12} = -(\gamma + i\Delta_{21})\rho_{21} + i(-\Omega_{12}\rho_{11} + \Omega_{12}\rho_{22} + \Omega_{13}\rho_{32} - \Omega_{24}\rho_{14}) \quad (40)$$

$$\dot{\rho}_{13} = -(\gamma + i\Delta_{31})\rho_{13} + i(-\Omega_{13}\rho_{13} + \Omega_{12}\rho_{23} + \Omega_{13}\rho_{33} - \Omega_{34}\rho_{14}) \quad (41)$$

$$\dot{\rho}_{14} = -\gamma\rho_{14} + i(-\Omega_{12}\rho_{24} + \Omega_{24}\rho_{14} + \Omega_{13}\rho_{34} - \Omega_{34}\rho_{13}) \quad (42)$$

$$\dot{\rho}_{23} = -\gamma\rho_{23} + i(-\Omega_{21}\rho_{13} + \Omega_{13}\rho_{21} + \Omega_{24}\rho_{43} - \Omega_{34}\rho_{24}) \quad (43)$$

$$\dot{\rho}_{24} = -(\gamma + i\Delta_{24})\rho_{24} + i(\Omega_{21}\rho_{14} - \Omega_{24}\rho_{22} - \Omega_{34}\rho_{23}) \quad (44)$$

$$\dot{\rho}_{34} = -(\gamma + i\Delta_{34})\rho_{34} + i(+\Omega_{13}\rho_{14} - \Omega_{24}\rho_{32} - \Omega_{34}\rho_{33}) \quad (45)$$

$$\dot{\rho}_{11} = A_{21}\rho_{22} + A_{31}\rho_{33} + i(\Omega_{12}\rho_{21} - \Omega_{21}\rho_{12} + \Omega_{13}\rho_{31} - \Omega_{13}\rho_{13}) \quad (46)$$

$$\dot{\rho}_{22} = -A_{21}\rho_{22} + i(\Omega_{21}\rho_{12} - \Omega_{12}\rho_{21} + \Omega_{24}\rho_{42} - \Omega_{24}\rho_{24}) \quad (47)$$

$$\dot{\rho}_{33} = -A_{31}\rho_{33} + i(\Omega_{13}\rho_{13} - \Omega_{13}\rho_{31} + \Omega_{34}\rho_{43} - \Omega_{34}\rho_{34}) \quad (48)$$

The system of equations above was solved in *Mathematica* for different values of detuning. The applied field is written as $E(t) = E_p(t) + E_r(t)$. The amount of detuning acts to increase the population transfer in both SERS and HRS. Here, we present one detuning, to demonstrate the population transfer that results from a stimulated Raman process. A full description and model to include the entire tuning range is the subject of another work.

Conclusion

In this paper we have demonstrated lasing near the 4^2P resonance doublet using Raman scattering. Using the density operator formalism, the third-order susceptibility shows how the SERS process achieves gain based on a two photon transition by transferring population from one excited electronic state to another. The SERS process is strongest near the resonances while the hyper-Raman process is most ef-

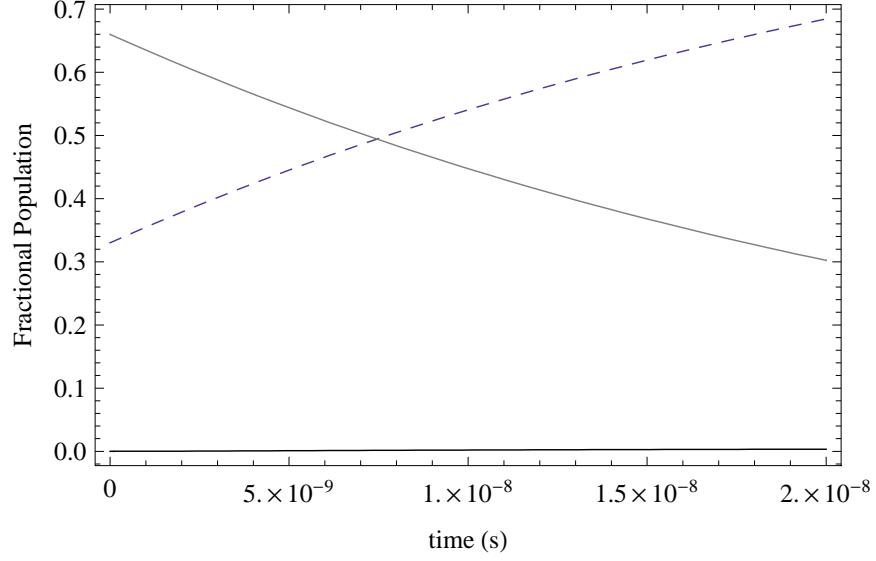


Figure 39. Simulated fractional population densities of the ρ_{11} (---) and ρ_{33} (—) states for a pump detuning of -20 cm^{-1} from the D_2 line (ρ_{33}).

ficient when the pump is tuned between the resonance lines. For each process it is possible to find a region in the pump spectrum where one process clearly dominates and all other processes are minimized. In the case of lasing on the 1st anti-Stokes line, pumping near the D_2 resonance results in strong anti-Stokes signal, converting approximately 7% of the pump light into a collimated beam blue-shifted by 3.4 nm. For the case of the hyper-Raman lasing process, we achieved a slope efficiency of 10.4% with a threshold of 60 mW with little to no competition from other Raman processes. The hyper-Raman process offers linear tunability with good performance even when the pump and hyper Raman beams are spectrally separated by less than 1 nm. This is potentially useful for systems that require adaptive optics to calculate distortion due to atmospheric turbulence. A portion of the main beam of a DPAL system could be used to generate hyper Raman light very close to the frequency of the main beam allowing for the most accurate characterization of the atmosphere while being easily separated using a spectrometer. There is also the possibility of using rapid pump frequency sweeping to induce a large change in laser spectral output due

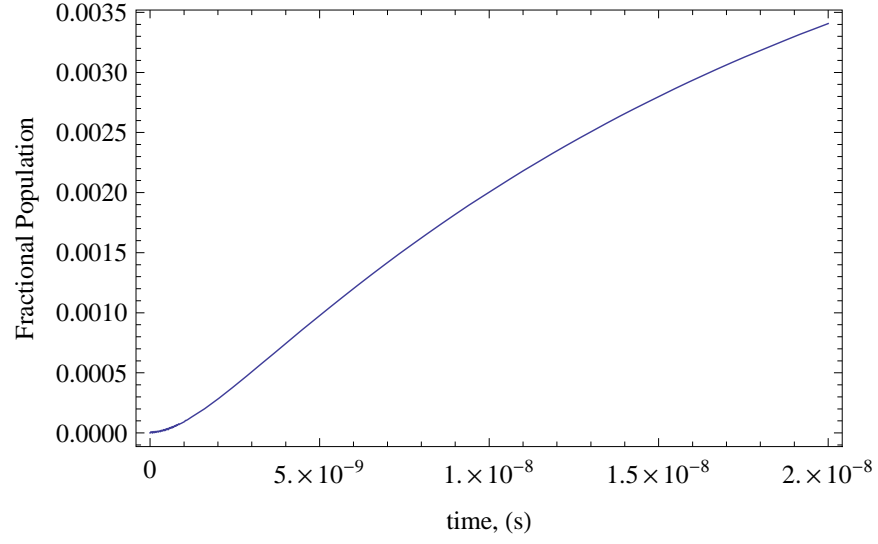


Figure 40. Simulated fractional population densities of the the $4^2\text{P}_{1/2}$ state (ρ_{22}), showing population transfer via a Raman process from $4^2\text{P}_{3/2}$.

to the competitive relationship of the SERS and HRS processes.

VI. Conclusion and Recommendations

The decision to study the higher excited electronic states in cesium was an effort to expand the DPAL concept to shorter wavelengths than had been previously demonstrated. An optically pumped blue rubidium and cesium laser was recently demonstrated by our group at AFIT. [90] This laser was pumped using a two-photon nonlinear process. In contrast, I proposed and demonstrated a blue cesium laser based on direct optical (single photon) pumping. Direct optical excitation leading to a visible wavelength laser is a direct analog to the near-infrared case and offered a chance to compare the kinetics involved in the higher excited states, that ultimately led to improving our knowledge of atomic-molecular collisions.

A search of the literature showed that the majority of spectroscopic studies of excited alkali states were focused on collisions with noble gases, and only a few studies had reported spin orbit or quenching cross sections for the gases most commonly used in DPAL research like methane and ethane. In most cases, the spin orbit and quenching rates were calculated using cw pump sources and intensity ratio spectroscopic methods. The quenching rates between the fine-structure sublevels were not resolved in these works and determining these differences was an important step in validating the potential of a visible wavelength, single-photon pumped, alkali laser. In some atomic species the quenching rates between individual sublevels can be quite large.

The electronic states of the alkali metals consist of a repeating pattern of energy levels. The lowest 2P states have been shown to make excellent near-infrared lasers due to the rapid spin-orbit mixing and low quenching rates in collisions with a wide variety of buffer gases, the most important species being helium, methane and ethane. The second 2P state can be reached via two-photon pumping as previously mentioned, but it is also possible to directly pump these states from the ground using a dye laser

tuned to the optical transition. Like the traditional DPAL laser, buffer gases are used to rapidly mix the pump state and populate the upper laser level.

The use of a pulsed dye laser in this research rather than a cw source allowed the time-resolved fluorescence curves to be compared to a rate equation model. Validating the rate equation model against the time-dependent fluorescence data was an important step in understanding the complex interactions of the excited alkali atoms and the various buffer gases. Unlike the lower 2P states, the higher levels have many different relaxation pathways that can depopulate the pumped and upper laser level resulting in poor performance from bottlenecking.

During an unrelated experiment that utilized a potassium/helium mixture as a DPAL laser system, it was discovered that at low helium pressures and high potassium densities, several other unexpected wavelengths were present in the output that made characterising the lasing mechanism and performance in this regime very difficult. [41] Upon closer inspection, it was revealed that nonlinear two and three photon Raman scattering processes were competing with the spin-orbit relaxed three-level lasing process. These Raman processes had been observed before by several others in potassium vapor cell experiments [10, 15] In our case the mechanism was enhanced by a stable optical cavity and efficient, tunable lasing in the deep red (763-775 nm) was demonstrated and characterized.

Cesium 7^2P Kinetics

The spin orbit mixing and quenching cross sections of Cs 7^2P in mixtures with several important buffer gas species were measured. Collision induced mixing in Cs $7^2P_{3/2,1/2}$ is rapid, due to the small energy splitting. The scaling of helium induced mixing rates among the various excited Cs states is well described by a single parameter, the adiabaticity. The mixing rates by molecular collision partners are somewhat

larger and appear to be enhanced by vibrational energy transfer. In contrast to the lowest, Cs $6^2P_{3/2,1/2}$ levels, the higher excited states are rapidly quenched. Intermultiplet energy transfer likely enhances the quenching rates. Quenching of the blue laser upper level, $7^2P_{1/2}$, by ethane is about 42% of the fine structure mixing rate. While a blue laser with direct optical pumping of $7^2P_{3/2}$ has been demonstrated, the rapid quenching imposes an increased pump rate to reach threshold and a higher heat load.

Pulsed Blue Cesium Laser

A blue laser based on direct optical excitation of the second resonance doublet of cesium was demonstrated. This laser is similar to the original infrared DPAL concept in that only one pump photon is required in contrast to previous two-photon pumping schemes used to generate blue light in cesium. Blue light was generated using only helium as a buffer gas, but the best results were found in a mixture of helium and ethane at pressures of 550 and 100 torr, respectively. A stable cavity was formed using a high reflector and curved output coupler with a radius of curvature of 50 cm and cavity length of 48 cm. The best performance was using a 90% output coupler at a temperature of 110 °C. The role of intermultiplet mixing was also explored. Using simulations from a modified rate equation model, it was determined that while the actual fraction directly quenched to the ground was 50% or less. This can be interpreted in several ways, but the most likely explanation is that the primary quenching channel is from the 7P to 7S by conversion of electronic to vib-rotational and translational energy of the ethane molecule. The output power and slope efficiency while low ($\approx 3.3 \mu\text{J}$ and 0.45%, respectively), are similar to previous efforts to generate blue laser light in cesium. The low performance is most likely explained by poor pump mode overlap and bottlenecking.

Potassium Hyper Raman Laser

A hyper-Raman potassium laser, based on nonlinear optical pumping of the K $4S_{1/2}-4P_{3/2,1/2}$ transition was developed and characterized. The laser gain medium is a 15 cm length of potassium vapor inside a stainless steel heat pipe. A stable cavity was formed using a HR and output coupler ($R = 30\%$) separated by about 25 cm. Two lasing regimes are demonstrated. The first, due to SERS maintains a constant 3.8 nm difference based on the separation of the fine structure energy levels of potassium. A second lasing regime, due to a three photon process, provides efficient output that is linearly dependent on input wavelength. This laser is tunable over about 4 nm, with an output from 766-770 nm, with a slope efficiency of 10.7% and a maximum output power of 12 mW.

Blue Cesium Laser Recommendations

Regardless of the pumping mechanism used, the low optical gain of the blue transitions and larger quenching cross sections for the buffer gases tested in this work will likely not result in efficient laser operation or scalability to high powers. Currently, most experimental DPAL lasers, including this system, use a surrogate pump source such as a dye or Ti:Sapphire laser. The true benefit of the DPAL scheme comes from using an efficient diode pump source. Such pump sources are readily available at the infrared wavelengths, but not in the blue. Current blue diode research is a high-interest area due to the commercialization of laser-based displays and laser microscopy. A blue diode array with sufficient intensity may be commercially available in the near future. Once this technology becomes available, the true benefit of this research may be realized. Conversion of incoherent blue light from a diode array into a high-brightness, compact blue laser source would be an important demonstration, with many relevant military and commercial applications.

In order to improve the blue cesium laser several things can be done immediately. The search for a more efficient spin orbit relaxer gas would be the first priority. Identifying a relaxer gas with a quenching cross section of less than 1 \AA^2 (similar to helium) would result in much higher performance since it would minimize the quenching losses of the pumped and upper laser levels. Other gases that have been used successfully in DPAL research but were not tested in this work, such as CF_4 (Freon-14), Helium-3 and SF_6 should be tried. The blue laser may also be operated using helium only. Using 500 Torr of Helium only, we achieved a feeble blue output which proved difficult to repeat. It was unclear if 500 Torr was a threshold or if increasing the helium pressure to two to three atmospheres would improve performance.

The second priority would be to improve the laser cavity and gain medium. In this work we used a relatively short (2 cm) Pyrex cell and uncoated sapphire windows mounted at normal incidence. This type of cell is far from ideal for extracting maximum laser performance and has much higher optical losses than a cell with low-loss coatings and Brewster windows. It was unclear whether a longer cell (≈ 10 cm) would be beneficial. For the alkali three-level lasers to achieve inversion, the entire length of the gain medium must be bleached by the pump laser. Increasing the gain length may leave portions of the gain length unbleached. Since the optical cross section of the alkalis is relatively large, any spontaneous laser radiation would be absorbed by the unbleached sections and losses would be too large for lasing to initiate.

If the blue laser concept is to be scaled to higher powers, it should be converted to a stainless-steel heat pipe oven (HPO) rather than a glass cell. The HPO configuration will allow for much better control over the uniformity of the cesium density in the cell as well as preventing cesium vapor from condensing on the optical windows due to the active cooling system. The optical losses due to condensation on the cell windows is a major source of frustration and a fair amount of lab time is wasted tending to their

cleanliness. After only a few condensation cycles, the entire cell must be disposed of due to the irreparable damage to the windows, and a new cell needs to be prepared. Since the HPO is largely immune to this phenomena, experimental data collection would be much higher. An unstable cavity may also improve performance as well as improving the pump-laser mode overlap.

The stimulated Raman scattering (SRS) present under high pump intensity and alkali density conditions may be problematic since SRS competes with the three-level lasing process. However, suppression of SRS in alkali vapors is often aided by increasing the buffer gas pressure. Increasing the helium or ethane pressure should minimize its impact since SRS tends to favor low (or zero) buffer gas pressures. If a blue laser is to be realized, a cw version of this laser should be explored. A cw dye laser or solid state laser would be an ideal pump source and a Q-switched cavity could be constructed.

In summary, the slope efficiency and output power of the blue cesium laser could be much better than this initial demonstration suggests if a more efficient spin-orbit relaxer gas can be found. Adding optically coated windows mounted at the Brewster angle would offer immediate improvement by reducing losses.

Potassium Hyper-Raman Laser Recommendations

The main benefit of the potassium hyper-Raman laser is that it does not require a buffer gas and is tuneable over a 4 nm range. The maximum output power was a modest 12 mW with a threshold of 60 mW. The output range of this laser is in the near-infrared with applications in photodynamic surgery, oxygen sensing (763 nm) and optical cooling of potassium atoms (767 and 773 nm). The true benefit of this laser is that it can be pumped with widely available diode laser sources. Using a diode pump and a compact potassium-filled HPO, a rugged, tunable wavelength

source in the deep red can be constructed. Several other pump/lase schemes may also be considered since depending on the pump source frequency, both 4^2P levels may be populated allowing spin orbit relaxation mechanisms to induce lasing. In order to further characterize the performance of this laser, a numerical model using the semi-classical rate equations should be developed. This would allow a full understanding of the population transfer between the electronic states via Raman scattering. Finally, the rapid hopping from two to three-photon scattering should be explored. A rapidly shifted pump source (± 0.1 nm) with a narrow linewidth would allow the output to be rapidly switched over a range of about 2 nm.

Appendix A. Cesium Data

The cesium vapor pressure curve has been calculated by several authors over many years and the three most frequently cited fits are shown below in Fig. 41. Over the temperature range considered in this dissertation, there is only a small amount of difference between the three fits, mainly at the lower temperatures. The Nesmeyanov curve was used for all calculations in this work.

$$\log(p/\text{torr}) = 8.221 - \frac{4006.048}{T} - 0.00060194T - 0.19623\log T \quad \text{Nesmeyanov [61]} \quad (49)$$

$$\ln(p/\text{atm}) = (16493522)(K/T) + (16.021.38) \quad \text{Behrens [13]} \quad (50)$$

$$\log(p/\text{atm}) = 4.165 - \frac{3830}{T} \quad \text{Alcock [8]} \quad (51)$$

A table of Cesium properties is supplied for the convenience of the reader. This table is reproduced from [9]

The following plots contain information about the quality of the double exponential fit to the fluorescence decay data. This data was not included in the published journal articles but would be useful to those who might continue this research. In general, as the temperature increases, the signal-to-noise of the signal increases and the accuracy of the fit improves in the late time of the fluorescence curve. However, the first part of the data is obscured to the scattered pump light and cannot be recorded. At lower pressures, where the fluorescence rate rises more slowly, the majority of the curve can be seen and recorded. At higher pressures, above about 1.0 Torr for most gases tested, the front of the curve becomes completely obscured and must not be

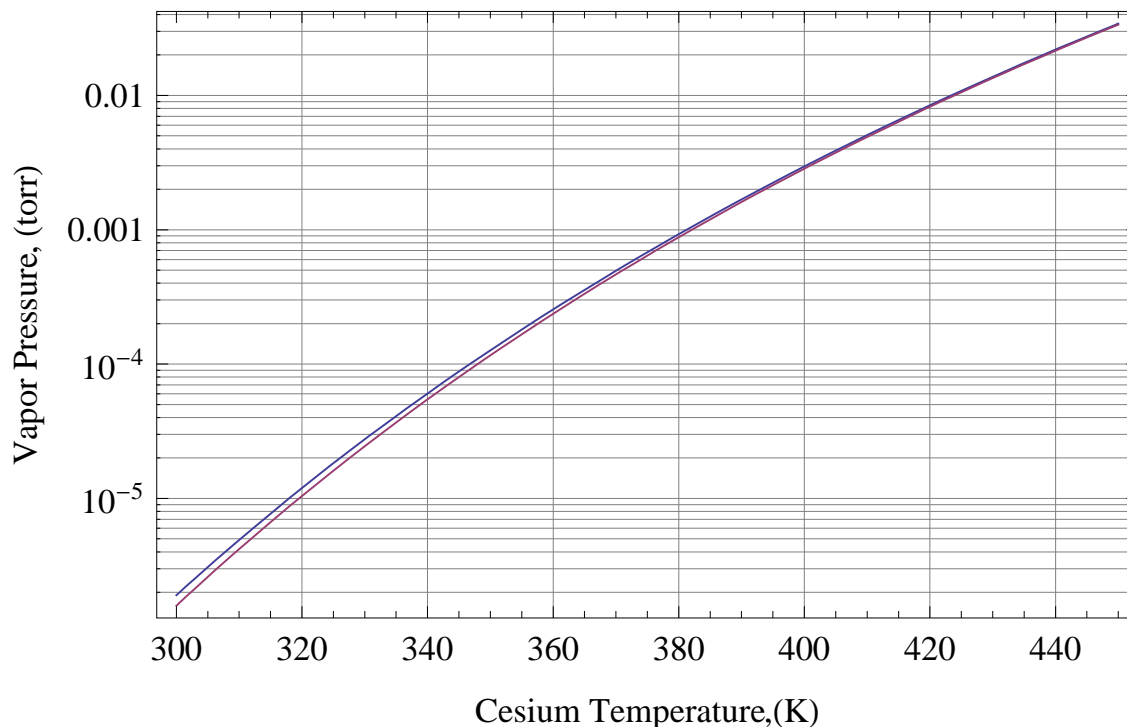


Figure 41. Vapor Pressure of Cesium according to Eqns. 49 and 51

included in the fit.

The simulated data shown below for helium and methane are using the same model for ethane. The portion of the model having the greatest amount of influence over whether the model matched the experimental data over the whole series of buffer gases was the amount of trapping. More specifically, which trapping model was used: Doppler or Pressure broadened trapping. At the the low pressures of the experiment, the Doppler model with a constant, pressure-independent trapping factor allowed the model to describe the data for both helium and methane. However, we found that for Ethane, despite the low pressures that the pressure-broadened trapping model could also provide a good fit to the experimental fluorescence data.

Table 11. Cesium (Cs) physical properties

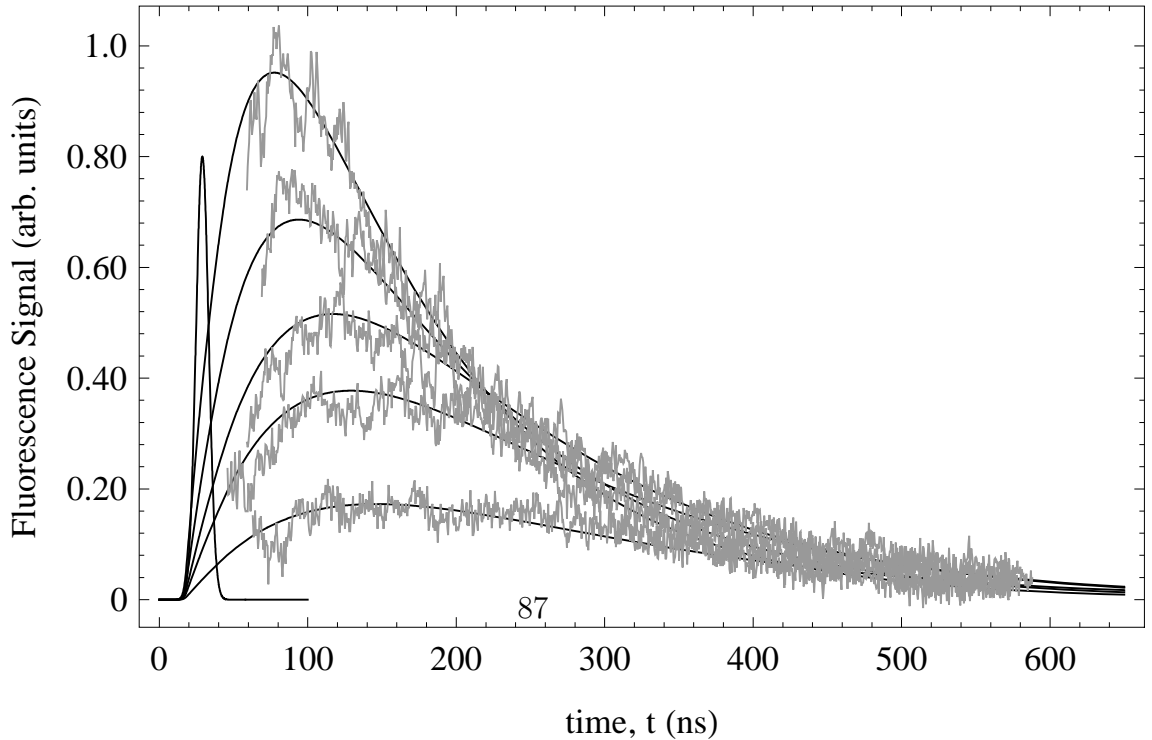
Property	Symbol	Value
Atomic number [†]	Z	55
Total nucleons [†]	$Z + N$	133
Ground state [†]	—	$6s^2S_{1/2}$
Relative natural abundance [†]	$\eta(^{133}\text{Cs})$	100%
Atomic mass [†]	m	132.905 452(1) u
Melting point [‡]	T_m	28.44 °C
Boiling point [‡]	T_b	671.0 °C
Density (solid) [‡]	ρ	1879 kg m ⁻³
Nuclear spin [†]	I	7/2
Magnetic moment	μ	+2.579
Ionization energy [†]	E_I	3.893 90(2) eV

[†] NIST “Chemistry Webbook.” 2005

[‡] Winter, M. “WebElements.” 2008

Table 12. (Cesium $7^2P_{3/2}$) optical properties of allowed dipole transitions

Final State	Oscillator Strength (dim.) [87]	Branching Ratio (%) [37]	Wavelength (nm) [1]
$6S_{1/2}$	0.0174	36	455.528
$7S_{1/2}$	1.115	49	2931.81
$5D_{5/2}$	1.533	13	1360.63
$5D_{3/2}$	0.208	1.6	1439.44



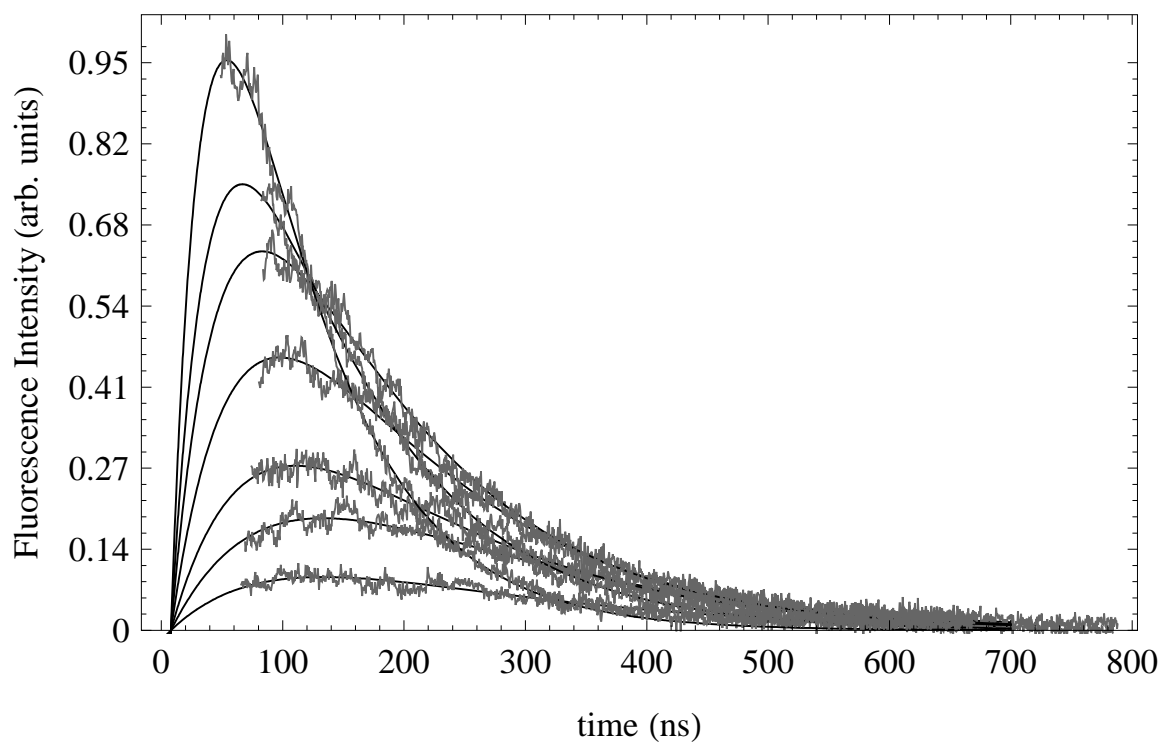


Figure 42. Time dependent fluorescence decay with double-exponential fits (—) for methane. Methane pressures in torr, from top to bottom: 1.0, 0.7, 0.5, 0.4, 0.3, 0.2, 0.1

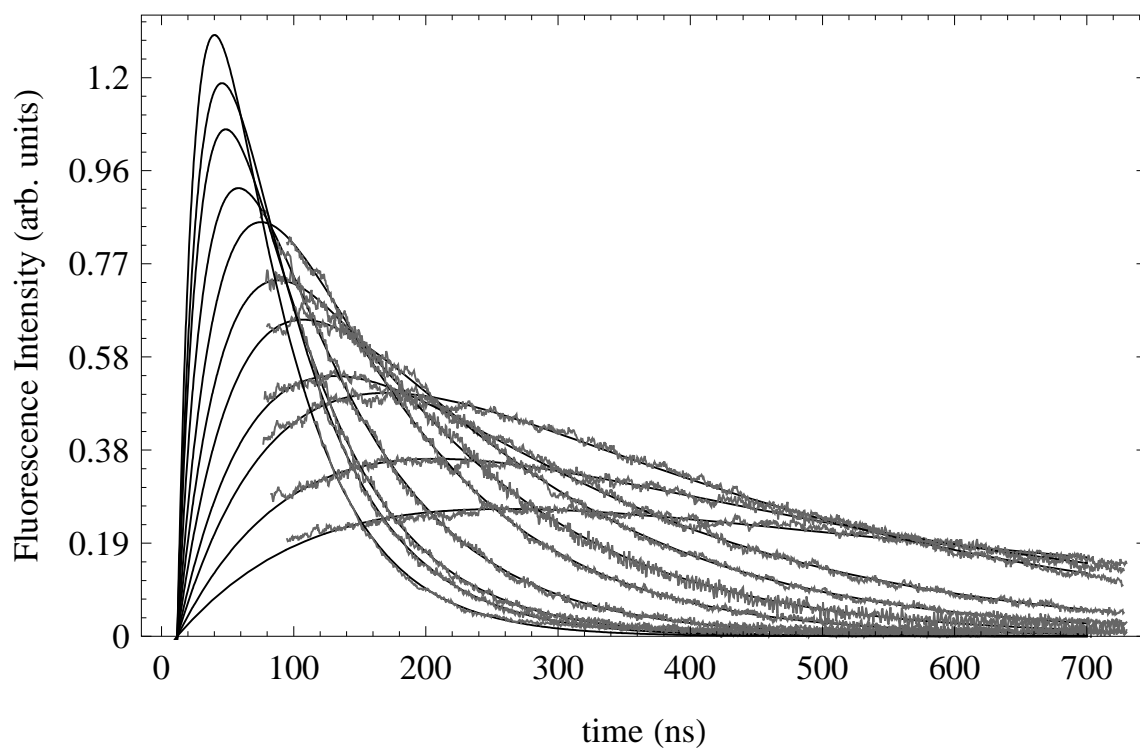


Figure 43. Time dependent fluorescence decay with double-exponential fits (—) for ethane. Ethane pressures in torr, from top to bottom: 1.3, 1.1, 1.0, 0.8, 0.6, 0.5, 0.4, 0.3, 0.2, 0.1

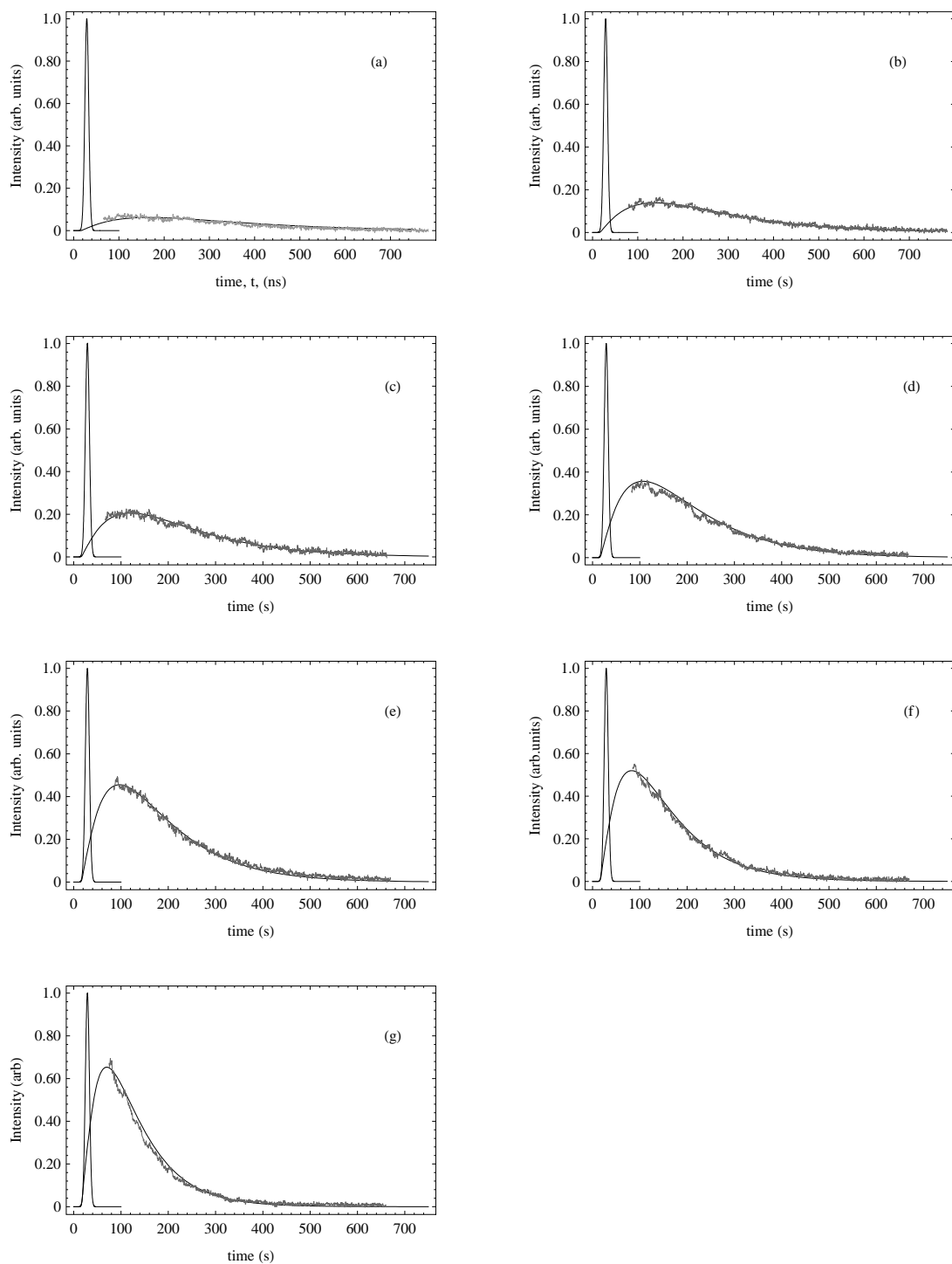


Figure 45. Simulated side fluorescence plots (solid) with experimental data for methane at $T=110^{\circ}\text{C}$. Methane gas pressure in torr: (a) 0.2, (b) 0.4, (c) 0.6, (d) 1.2, (e) 2.0

Appendix B. Potassium Data

The potassium vapor pressure curve calculated by Alcock is presented below. This vapor pressure curve was used in the course of this research.

$$\ln(p/\text{mbar}) = 7.4077 - \frac{4453}{T} \quad \text{Alcock [8]} \quad (52)$$

The physical constants of Potassium are provided for the convenience of the reader. The source of this information can be found in [6]

Table 13. Potassium (K) physical properties

Property	Symbol	Value
Atomic number [†]	Z	19
Total nucleons [†]	$Z + N$	39
Ground state [†]	—	$4s^2S_{1/2}$
Relative natural abundance [†]	$\eta(^{39}\text{K})$	93.25%
Atomic mass [†]	m	39.0983 u
Melting point [‡]	T_m	65.65 °C
Boiling point [‡]	T_b	774.00 °C
Density (solid) [‡]	ρ	862 kg m ⁻³
Nuclear spin [†]	I	3/2
Magnetic moment	μ	+0.391 46
Ionization energy [†]	E_I	4.340 66 eV

[†] NIST “<http://physics.nist.gov/PhysRefData/Handbook/Tables/potassiumtable1.htm>”

[‡] “<http://www.chemicalelements.com/elements/k.html>”

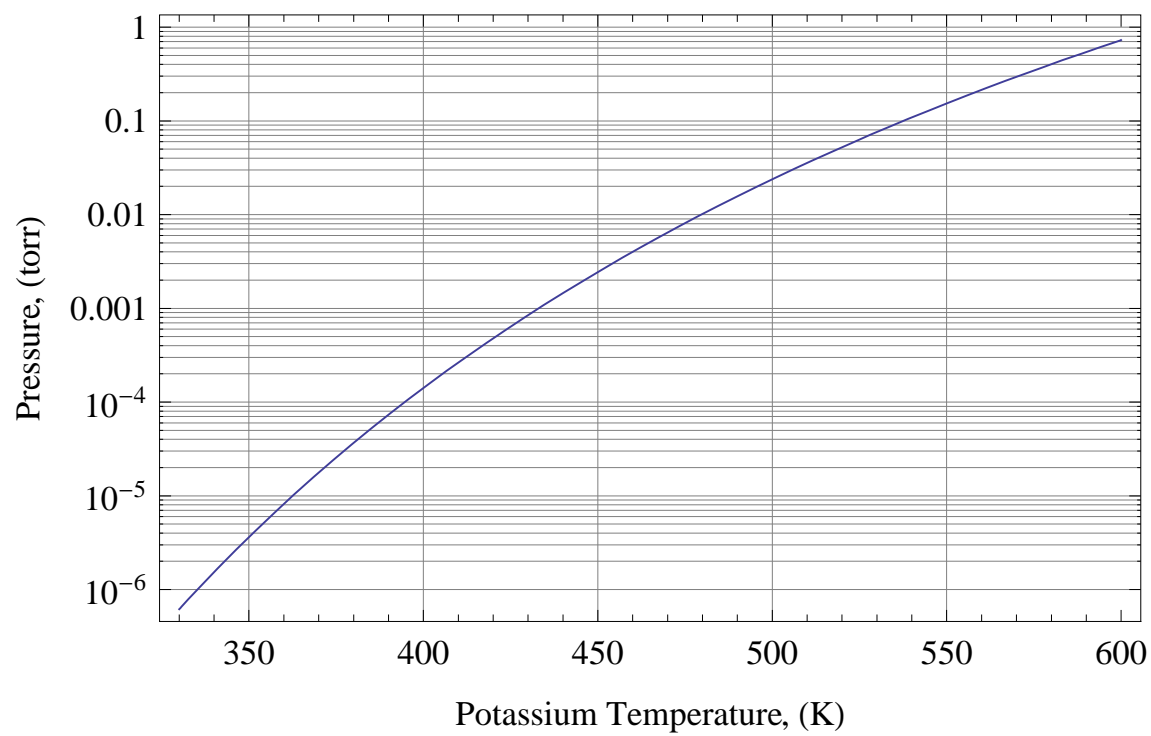


Figure 46. Vapor Pressure of potassium according to Eqn. 52

Bibliography

- [1] URL <http://physics.nist.gov/PhysRefData/Handbook/periodictable.htm>.
- [2] URL http://www.as.northropgrumman.com/products/maritime_laser/index.html.
- [3] URL <http://www.onr.navy.mil/en/Science-Technology/Departments/Code-35/All-Programs/aerospace-research-351/Maritime-Laser-Demonstration.aspx>.
- [4] URL <http://www.boeing.com/defense-space/space/avenger/index.html>.
- [5] URL <http://vpl.astro.washington.edu/spectra>.
- [6] *NIST Handbook of Basic Atomic Spectroscopic Data* <http://physics.nist.gov/asd>. National Institute of Standards and Technology, Gaithersburg MD, 20899, 2011.
- [7] Akulshin, M., R.J. McLean, A.I. Sidorov, and P. Hannaford. “Coherent and collimated blue light generated by four-wave mixing in Rb vapour”. *Opt. Express*, 17(25):22861–22870, 2009.
- [8] Alcock, C.B., V.P. Itkin, and M.K. Horrigan. *Can. Met. Quart.*, 23:309, 1984.
- [9] Anderson, M. *Tunable Optical Delay in Doppler-Broadened Cesium Vapor*. Ph.D. thesis, Air Force Institute of Technology, 2010.
- [10] Anikin, V.I., S.V. Kryuchkov, and V.E. Oguluzdin. “Resonant stimulated electronic Raman scattering in potassium vapor. Dispersion near principle doublet and influence of four-photon process”. *Sov. J. Quant. Elec.*, 4(9), 1975.
- [11] Beach, R. J., W. F. Krupke, V. K. Kanz, and S. A. Payne. “End-pumped continuous-wave alkali vapor lasers: experiment, model, and power scaling”. *J. Opt. Soc. Am. B*, 21(12):2151–2163, 2004.
- [12] Beer, C.W. and R.A. Bernheim. “Hyperfine press shift of ^{133}Cs atoms in noble and molecular buffer gases”. *Phys. Rev. A.*, 13(3):1052–1057, 1976.
- [13] Behrens, R.G., H.O. Woodrow, and S. Aronson. “Vapor pressure of liquid cesium by a Knudsen-effusion radiotracer technique”. *The Journal of Chemical Thermodynamics*, 9:1035–1044, 1977.
- [14] Berends, R. W., W. Kedzierski, A.G. McConkey, J.B. Atkinson, and L. Krause. “Quenching of 5^2P potassium atoms by collisions with H_2 , N_2 and CH_4 ”. *J. Phys. B: At. Mol. Phys.*, 22:L165–L169, 1989.

- [15] Bradley, D.J. “Stimulated Stokes and anti-Stokes electronic Raman scattering by selectively excited potassium and rubidium atoms”. *J. Phys. B: At. Mol. Phys.*, 4, 1971.
- [16] Brown, K. C. and G. P. Perram. “Cesium laser operating in the blue via direct optical excitation of the $7^2P_{3/2}$ state”. *High Energy/Average Power Lasers and Intense Beam Applications V (7915)*. SPIE, 2011.
- [17] Brown, K. C. and G. P. Perram. “Cesium laser operating in the blue via direct optical excitation of the $7^2P_{3/2}$ state”. S. J. Davis (editor), *Proceedings of the SPIE: High Energy/Average Power Lasers and Intense Beam Applications V*, volume 7915. SPIE, 2011.
- [18] Brown, K. C. and G. P. Perram. “Spin-orbit relaxation and quenching of cesium 7^2P in mixtures of helium, methane, and ethane”. *Appl. Phys. B.*, 2012. To be published.
- [19] Brown, K.C. and G. P. Perram. “Tunable Hyper-Raman Potassium Vapor Laser”. *42nd AIAA Plasmadynamics and Lasers Conference (2011)*.
- [20] Butler, Amy. “Lights Out For The Airborne Laser”. URL www.aviationweek.com.
- [21] Chou, C.-S. and Lin K.-C. “Collisional deactivation of K in the high-lying 2S and 2D states by He, Ne, and Ar”. *J. Chem. Phys.*, 105(7):2719–2725, 1996.
- [22] Colbert, T. and J. Heunneken. “Radiation trapping under conditions of low to moderate line-center optical depth”. *Phys. Rev. A.*, 41(11):6145–6154, 1990.
- [23] Cuvellier, J., P. R. Fournier, F. Gounand, J. Pascale, and J. Berlande. “Inelastic collisions involving excited cesium atoms at thermal energies”. *Phys. Rev. A.*, 11(3):846–856, 1975.
- [24] Cuvellier, J., L. Petitjean, J. M. Mestdagh, D. Paillard, P. de Pujo, and J. Berlande. “Near-resonant electronic-to-rotational energy transfer in Rb($7S-5D$)-H₂, D₂ collisions at thermal energy”. *J. Chem. Phys.*, 84(3):1451–1457, 1986.
- [25] Demtröder, W. *Laser Spectroscopy, Vol. 1*. Springer, 4th edition, 2008.
- [26] Derevianko, A., W.R. Johnson, M.S. Safronova, and J.F. Babb. “High-Precision Calculations of Dispersion Coefficients, Static Dipole Polarizabilities, and Atom-Wall Interaction Constants for Alkali-Metal Atoms”. *Phys. Rev. Lett.*, 82(18):3589, 1999.
- [27] Derevianko, A. and S.G. Porsev. “Determination of lifetimes of $6P_J$ levels and ground-state polarizability of Cs from the van der Waals coefficient C_6 ”. *Phys. Rev. A.*, 65(053403-1), 2002.

- [28] DiBerardino, D., C.E. Tanner, and A. Sieradzan. “Lifetime measurements of cesium $5^2D_{5/2,3/2}$ and $11^2S_{1/2}$ ”. *Phys. Rev. A.*, 57:4204, 1998.
- [29] Earl, B.L. and R. R. Herm. “Photodissociation of NaBr, NaI, and KI vapors and collisional quenching of Na^* (3^2P), K^* (4^2P), and K^* (5^2P) by foreign gases”. *J. Chem. Phys.*, 60(11):4568–4578, 1974.
- [30] Fabry, M. “Theoretical and Experimental Determinations of Cesium Oscillator Strengths”. *J. Quant. Spect. Radiat. Trans.*, 16(127-135), 1976.
- [31] Ferray, M., J.P. Visticot, J. Lozingot, and B. Sayer. “Broadening of the caesium second resonance doublet by collisions with hydrogen molecules”. *J. Phys. B: At. Mol. Phys.*, 14:3875–3879, 1981.
- [32] Fisher, E.R. and G.K. Smith. “Vibration-Electronic Coupling in the Quenching of Electronically Excited Alkali Atoms by Diatomics”. *Appl. Opt.*, 10(8), 1971.
- [33] Gallagher, A. “Rubidium and Cesium Excitation Transfer in Nearly Adiabatic Collisions with Inert Gases”. *Phys. Rev.*, 172:88–96, 1968.
- [34] Gross, M., J. M. Raimond, and S. Haroche. “Doppler Beats in Superradiance”. *Phys. Rev. Lett.*, 40(26):1711–1718, 1978.
- [35] Guzman, A.M. and C. Ramirez. “Hyper-raman scattering and three-photon resonant ionization: Competitive effects”. *Phys. Rev. A.*, 47(3):4270–4276, 1993.
- [36] Hager, G.D. and G. P. Perram. “A three-level analytic model for alkali metal vapor lasers: part I. Narrowband optical pumping”. *Appl. Phys. B.*, 101:45–56, 2010.
- [37] Heavens, O.S. “Radiative Transition Probabilities of the Lower Excited States of the Alkali Metals”. *J. Opt. Soc. Am.*, 51(10):1058–1061, 1961.
- [38] Holstein, T. “Imprisonment of Resonance Radiation”. *Phys. Rev.*, 72(12):1212–1233, 1947.
- [39] Huennekens, J. and A. Gallagher. “Radiation diffusion and saturation in optically thick Na vapor”. *Phys. Rev. A.*, 28(1):238–247, 1983.
- [40] Huennekens, J., H.J. Park, T. Colbert, and S.C. McClain. “Radiation trapping in sodium–noble gas mixtures”. *Phys. Rev. A.*, 35(7):2892–2901, 1987.
- [41] Hurd, E. J. *Characteristics of a High Intensity, Pulsed Potassium Vapor Laser in a Heat Pipe*. Master’s thesis, Air Force Institute of Technology, 2011.
- [42] II, J. T. Swindell, B. McCarter, V. Komaragiri, and S. Bililign. “Quenching of $Li(3P)$ by CH_4 , C_2H_4 , C_2H_6 , C_3H_6 ,”. *Chem. Phys.*, 305:299–305, 2004.

- [43] Kielkopf, J. F. “Predicted alkali collisional broadening by noble gases based on semiempirical potentials”. *J. Phys. B: At. Mol. Phys.*, 9(17):L547–L550, 1976.
- [44] Konefal, Z. “Observation of collision induced processes in rubidium-ethane vapour”. *Opt. Comm.*, 164:95–105, 1999.
- [45] Konefal, Z. and M. Ignaciuk. “Stimulated Collision Induced Processes in Sodium Vapor in the Presence of Helium”. *Appl. Phys. B.*, 51:285–291, 1990.
- [46] Konefal, Z. and M. Ignaciuk. “Investigation of collisionally induced stimulated scattering in sodium vapor with temporal and spectral resolution”. *Appl. Phys. B.*, 61:101–110, 1995.
- [47] Konefal, Z. and Z. Trumpakaj. “Temporal and spatial evolution of collision-induced stimulated effects in alkali atoms”. *J. Phys. B: At. Mol. Phys.*, 31:3281–3295, 1998.
- [48] Krause, L. “Collisional Excitation Transfer Between the $^2P_{1/2}$ and $^2P_{3/2}$ Levels in Alkali Atoms”. *Appl. Opt.*, 5(9):1375–1382, 1966.
- [49] Krupke, W.F. “Diode pumped alkali lasers (DPALs)-A review”. *Progress in Quantum Optics*, 2011.
- [50] Krupke, W.F., R.J. Beach, V.K. Kanz, and S.A. Payne. “Resonance transition 795-nm rubidium laser”. *Opt. Lett.*, 28(23):2336–2338, 2003.
- [51] Krupke, W.F., R.J. Beach, S.A. Payne, V.K. Kanz, and J.T. Early. “DPAL: A New Class of Lasers for CW Power Beaming at Ideal Photovoltaic Cell Wavelengths”. *2nd International Symposium on Beamed Energy Propulsion, Sendai, Japan, October 20-23, 2003*. 2003.
- [52] Lennard-Jones, J.E. “On the determination of Molecular Fields II.” *Proc. R. Soc. Lond. A*, 106:463–477, 1924.
- [53] Lin, K-C., A.M. Schilowitz, and J.R. Wiesenfeld. “Collisional Deactivation of $K(5^2P_J)$ by H_2 . Identification of the Primary Quenching Channel”. *J. Phys. Chem.*, 88:6670–6675, 1984.
- [54] Liu, Y. and X. Ge. “Underwater Laser Sensor Network: A New Approach”. *5th WSEAS International Conference on Telecommunications and Informatics*, 421. 2006.
- [55] McGillis, D.A. and L. Krause. “Inelastic Collisions Between Excited Alkali Atoms and Molecules. I. Sensitized Fluorescence and Quenching in $Cs-N_2$ and $Cs-H_2$ Systems”. *Phys. Rev.*, 153(1):44–50, 1967.
- [56] Meijer, T., J.D. White, B. Smeets, M. Jeppesen, and R.E. Scholten. “Blue five-level frequency-upconversion system in rubidium”. *Opt. Lett.*, 31:1002, 2006.

- [57] Mestdagh, J. M., D. Paillard, J. Berlande, J. Cuvellier, and P. de Pujo. “Inter-multiplet transfers of excited sodium atoms induced by nitrogen molecules”. *J. Chem. Phys.*, 89(1):251–256, 1988.
- [58] Miller, W.S., C.V. Sulham, J.C. Holtgrave, and G.P. Perram. “Limitations of an optically pumped rubidium laser imposed by atom recycle rate”. *Appl. Phys. B.*, 103:819, 2011.
- [59] Molisch, A.F., B.P. Oehry, W. Schupita, and G. Magerl. “Radiation trapping in cylindrical and spherical geometries”. *J. Quant. Spect. Radiat. Trans.*, 49(4):361–370, 1993.
- [60] Munster, P. and J Marek. “Determination of cross sections of excitation transfer between the fine-structure components of Cs(7^2P), Rb(6^2) and Rb(7^2P) induced by collisions with rare-gas atoms”. *J. Phys. B: At. Mol. Phys.*, 14:1009–1018, 1981.
- [61] Nesmeyanov, A.N. *Vapor Pressure of the Elements*. Academic Press, New York, 1963.
- [62] Page, R. H. and R. J. Beach. *Diode-Pumped Alkali Atom Lasers*. Technical report, Lawrence Livermore National Laboratory, <https://e-reports-ext.llnl.gov/pdf/316721.pdf>, 2004.
- [63] Page, R. H. and R. J. Beach. *Diode-Pumped Alkali Atom Lasers*. Technical Report UCRL-TR-210223, 2005.
- [64] Page, R. H., R. J. Beach, and V. K. Kranz. *Multimode diode-pumped alkali-vapor laser*. Technical Report UCRL-JRNL-214842, 2005.
- [65] Paillard, D., J.M. Mestdagh, J. Cuvellier, P. de Pujo, and J. Berlande. “Collisions of excited alkali atom with O₂. I. Intermultiplet transfer”. *J. Chem. Phys.*, 87(4):2084–2089, 1987.
- [66] Perschbacher, T.A., D. A. Hostutler, and T.M. Shay. “Proceeding of the SPIE 6346”. 63460, 7–11. 2006.
- [67] Petersen, A.B. and R.J. Lane. “A diode pumped Rb laser at 398 nm”. *Proc. SPIE 6871*, 68711Q-1. 2008.
- [68] Pitz, G.A, C. D. Fox, and G.P. Perram. “Transfer between the cesium $6^2P_{1/2}$ and $6^2P_{3/2}$ levels induced by collisions with H₂, HD, D₂, CH₄, C₂H₆, CF₄, and C₂F₆”. *Phys. Rev. A.*, 84:032708, 2011.
- [69] Rafac, R.J., C.E. Tanner, A.E. Livingston, K.W. Kukla, H.G. Berry, and C.A. Kurtz. “Precision lifetime measurements of the $6P^2P_{1/2,3/2}$ states in atomic cesium”. *Phys. Rev. A.*, 50:R1976, 1994.

- [70] Risk, W.P., T.R. Gosnell, and A.V. Nurmikko. *Compact Blue-Green Lasers*. Cambridge University Press, 2003.
- [71] Rosenberry, M.A., J.P. Reyes, D. Tupa, and T.J. Gay. “Radation trapping in rubidium optical pumping at low buffer-gas pressures”. *Phys. Rev. A.*, 75(023401), 2007.
- [72] Rostas, F. and J. L. Lemaire. “Low pressure measurement of the broadening and shift of the caesium 4555 Å and 4593 Å lines by helium and argon”. *J. Phys. B: At. Mol. Phys.*, 4:555–564, 1971.
- [73] Rotandaro, M. D. and G. P. Perram. “Collision-induced transitions between the Zeeman-split (J,m) levels of Rb($5^2P_{1/2}$, $5^2P_{3/2}$)”. *Phys. Rev. A.*, 58:2023, 1998.
- [74] Safronova, M.S. and C.W. Clark. “Inconsistencies between lifetime and polarizability measurements in Cs”. *Phys. Rev. A.*, 69:040501, 2004.
- [75] Sanchez, B.N. and T. Brandes. “Matrix perturbation theory for driven three-level systems with damping”. *Ann. Phys. (Leipzig)*, 1(26):1–26, 2004.
- [76] Sasonetti, J.E. “Wavelengths, Transition Probabilities, and Energy Levels for the Spectra of Potassium (KI through KXIX)”. *J. Phys. Chem. Ref. Data*, 37(7), 2008.
- [77] Sasso, A., W. Demtroder, T. Colbert, C. Wang, E. Erlacher, and J. Huennekens. “Radiative lifetimes, collisional mixing, and quenching of the cesium $5D_J$ levels”. *Phys. Rev. A.*, 45(3):1670–1680, 1992.
- [78] Shevy, Y. and M. Rosenbluh. “Polarization dependence of resonance-enhanced three-photon scattering”. *Opt. Lett.*, 13:1005–1007, 1988.
- [79] Shevy, Y., M. Rosenbluh, and H. Friedman. “Simultaneous observation of excited-state Raman scattering and resonance-enhanced three-photon scattering”. *Phys. Rev. A*, 31:1209–1212, 1985.
- [80] Shevy, Y., M. Rosenbluh, and H. Friedman. “Stimulated excited-state Raman scattering and three-photon scattering in sodium”. *Opt. Lett.*, 11:85–87, 1986.
- [81] Shultz, J.T., S. Abend, D. Doring, J. E. Debs, P. A. Altin, J. D. White, N. P. Robins, and J. D. Close. “Coherent 455nm beam production in a cesium vapor”. *Opt. Lett.*, 34:2321, 2009.
- [82] Siara, I.N., R. U. Dubois, and L. Krause. “Temperature effect of cross sections for $7^2P_{1/2}$ – $7^2P_{3/2}$ excitation transfer and for quenching in cesium, induced in collisions with H_2 , N_2 , CH_4 , and CD_4 ”. *Can. J. Phys.*, 60:239–244, 1982.

- [83] Siara, I.N. and L. Krause. “Inelastic collisions between Excited Alkali Atoms and Molecules. VIII. $6^2P_{1/2}$ – $6^2P_{3/2}$ Mixing and Quenching in Mixtures of Rubidium with H_2 , HD , D_2 , N_2 , CH_4 , and CD_4 ”. *Can. J. Phys.*, 51:257–265, 1973.
- [84] Siara, I.N., H.S. Kwong, and L. Krause. “Sensitized fluorescence in vapors of alkali atoms XIV. Temperature dependence of cross sections for $7^2P_{1/2}$ – $7^2P_{3/2}$ mixing in cesium, induced in collisions with noble gas atoms”. *Can. J. Phys.*, 52:945, 1974.
- [85] Smith, R. C. and K. S. Baker. “Optical properties of the clearest natural waters”. *Appl. Opt.*, 20(2):177–184, 1981.
- [86] Sorokin, P.P., N.S. Shiren, J.R. Lankard, E.C. Hammond, and T.G. Kazyaka. “Stimulated Electronic Raman Scattering”. *Appl Phys. Lett.*, 10(2):44–46, 1967.
- [87] Stone, P. M. “Cesium Oscillator Strengths”. *Phys. Rev.*, 127(4):1151–1156, 1962.
- [88] Sulham, C.V. *LASER DEMONSTRATION AND PERFORMANCE CHARACTERIZATION OF OPTICALLY PUMPED ALKALI LASER SYSTEMS*. Ph.D. thesis, Air Force Institute of Technology, 2010.
- [89] Sulham, C.V., G.P. Perram, M.P. Wilkinson, and D. A. Hostutler. “A pulsed, optically-pumped rubidium laser at high pump intensity”. *Opt. Comm.*, 283(4328), 2010.
- [90] Sulham, C.V., G.A. Pitz, and G.P. Perram. “Blue and infrared stimulated emission from alkali vapors pumped through two-photon absorption”. *Appl. Phys. B.*, 101:57, 2010.
- [91] Vasilyev, A.A., I.M. Savukov, M.S. Safronova, and H.G. Berry. “Measurement of the 6s-7p transition probabilities in atomic cesium and a revised value for the weak charge Q_w ”. *Phys. Rev. A.*, 66:020101, 2002.
- [92] Verdeyen, J. T. *Laser Electronics, 3rd Ed.* Prentice Hall, 1995.
- [93] Vernier, A., S. Franke-Arnold, E. Riis, and A.S. Arnold. “Enhanced frequency up-conversion in Rb vapor”. *Opt. Express*, 18(16):17020–17026, 2010.
- [94] Warwick, Graham. “Lasers 6, UAVs 0”. 2009. URL www.aviationweek.com.
- [95] Willenberg, G-D., J. Heppner, and F.B. Foote. “Interaction of Three Coherent Fields with Doppler Broadened Serial Four-Level Systems: Application to Four-Level FIR Lasers”. *IEEE J. of Quant. Elec.*, QE-18(13), 1982.

- [96] Xu, W-H., J. Wu, J-H. Qian, and J-Y. Gao. “Light amplification in the Frequency Up-Conversion Regime in a Three-Level System”. *Laser Physics*, 14(1):82–90, 2004.
- [97] Yatsiv, S. “Enhanced and Stimulated Multiphoton Processes in Free Atoms”. *IEEE J. of Quant. Elec.*, 4(11):900–904, 1968.
- [98] Zamoski, N. D., W. Rudolph, G. D. Hager, and D. A. Hostutler. “A study of collisional quenching and radiation-trapping kinetics for Rb(5P) in the presence of methane and ethane using time-resolved fluorescence”. *J. Phys. B: At. Mol. Phys.*, 42, 2009.
- [99] Zhdanov, B.V., T. Ehrenreich, and Knize R.J. “Highly efficient optically pumped cesium vapor laser”. *Opt. Comm.*, 260:696, 2006.
- [100] Zhdanov, B.V., B. J. Sell, and Knize R.J. “Multiple laser diode array pumped Cs laser with 48W output power”. *Elec. Lett.*, 44(582), 2008.
- [101] Zhdanov, B.V., M.K. Shaffer, W. Holmes, and Knize R.J. “Blue laser light generation by intracavity frequency doubling of Cesium vapor laser”. *Opt. Comm.*, 282(23):4585–4586, 2009.
- [102] Zibrov, A.S., M.D. Lukin, M. Hollberg, and M.O. Scully. “Efficient frequency up-conversion in resonant coherent media”. *Phys. Rev. A.*, 65:051801, 2002.
- [103] Zibrov, A.S., M.D. Lukin, L. Nikonov, M. Hollberg, O. Scully, V.L. Velichansky, and H.G. Robinson. “Experimental demonstration of laser oscillation without population inversion via quantum interference in Rb”. *Phys. Rev. Lett.*, 75:1499, 1995.
- [104] Zweiback, J., Komashko A., and W.F. Krupke. “Alkali Vapor Lasers”. *SPIE High Energy/Average Power Lasers and Intense Beam Applications Conference 7581*, 75810G–1. 2010.
- [105] Zweiback, J., G. D. Hager, and W. F. Krupke. “High efficiency hydrocarbon-free resonance transition potassium laser”. *Opt. Comm.*, 282:1871–1873, 2009.

REPORT DOCUMENTATION PAGE					Form Approved OMB No. 0704-0188	
<p>The public reporting burden for this collection of information is estimated to average 1 hour per response, including the time for reviewing instructions, searching existing data sources, gathering and maintaining the data needed, and completing and reviewing the collection of information. Send comments regarding this burden estimate or any other aspect of this collection of information, including suggestions for reducing this burden to Department of Defense, Washington Headquarters Services, Directorate for Information Operations and Reports (0704-0188), 1215 Jefferson Davis Highway, Suite 1204, Arlington, VA 22202-4302. Respondents should be aware that notwithstanding any other provision of law, no person shall be subject to any penalty for failing to comply with a collection of information if it does not display a currently valid OMB control number. PLEASE DO NOT RETURN YOUR FORM TO THE ABOVE ADDRESS.</p>						
1. REPORT DATE (DD-MM-YYYY)		2. REPORT TYPE		3. DATES COVERED (From — To)		
22-03-2012		Doctoral Dissertation		Sep 2008 — Mar 2012		
4. TITLE AND SUBTITLE Collisional Dynamics, Lasing and Stimulated Raman Scattering in Optically Pumped Cesium and Potassium Vapors				5a. CONTRACT NUMBER		
				5b. GRANT NUMBER		
				5c. PROGRAM ELEMENT NUMBER		
6. AUTHOR(S) Brown, Kirk, C., Maj, USAF				5d. PROJECT NUMBER		
				5e. TASK NUMBER		
				5f. WORK UNIT NUMBER		
7. PERFORMING ORGANIZATION NAME(S) AND ADDRESS(ES) Air Force Institute of Technology Graduate School of Engineering and Management (AFIT/EN) 2950 Hobson Way WPAFB OH 45433-7765				8. PERFORMING ORGANIZATION REPORT NUMBER AFIT/DS/ENP/12-M01		
9. SPONSORING / MONITORING AGENCY NAME(S) AND ADDRESS(ES) Harro Ackerman (505) 248-8208 High Energy Laser-Joint Technology Office 901 University Blvd. S.E. Suite 100 Kirtland AFB, NM 87106				10. SPONSOR/MONITOR'S ACRONYM(S) HEL-JTO		
				11. SPONSOR/MONITOR'S REPORT NUMBER(S)		
12. DISTRIBUTION / AVAILABILITY STATEMENT DISTRIBUTION STATEMENT A. APPROVED FOR PUBLIC RELEASE; DISTRIBUTION UNLIMITED.						
13. SUPPLEMENTARY NOTES						
14. ABSTRACT This dissertation explores collisional dynamics, lasing and stimulated Raman scattering in cesium and potassium vapors. The spin orbit mixing and quenching cross sections of several buffer gas species are measured. The fine-structure mixing cross sections for He, CH ₄ and C ₂ H ₆ are 14±3, 35±6 and 73±10 Å ² , respectively. The ² P _{3/2} state is quenched more rapidly than the ² P _{1/2} state. A pulsed blue laser operating via direct excitation of the cesium 7 ² P _{3/2} state is demonstrated. A theoretical model is extended and compared with experimental results. The maximum output energy was 3.3 μJ with a threshold of 10 μJ/pulse and a slope efficiency of 0.45%. A tuneable hyper Raman potassium vapor laser, tuneable over 4 nm is demonstrated and characterized. The output was tunable from 766–770 nm. The threshold for the hyper-Raman process was 60 mW. The maximum slope efficiency (10.4%) and output power (12 mW) are comparable to previously demonstrated potassium DPAL systems that used several atmospheres of buffer gas.						
15. SUBJECT TERMS Collisions, Kinetics, Quenching, Spin-Orbit, Alkali Vapor, Diode-Pumped Alkali Laser (DPAL), Stimulated Raman Scattering						
16. SECURITY CLASSIFICATION OF:			17. LIMITATION OF ABSTRACT	18. NUMBER OF PAGES	19a. NAME OF RESPONSIBLE PERSON	
a. REPORT	b. ABSTRACT	c. THIS PAGE			Dr. Glen P. Perram	
U	U	U	U	119	19b. TELEPHONE NUMBER (include area code) (937) 255-3636, x4504; glen.perram@afit.edu	